Cassini Plasma Spectrometer observations of Titan's ionospheric electrons and negative ions

Anne Wellbrock

Mullard Space Science Laboratory

Department of Space and Climate Physics

University College London

A thesis submitted to University College London for the degree of Doctor of Philosophy

September 2012

I, Anne Wellbrock, confirm that the work presented in this thesis is my own. Where information has been derived from other sources, I confirm that this has been indicated in the thesis.

…….

Signed

Abstract

The work in this thesis uses data from the Cassini spacecraft in the Saturnian system to study the ionosphere and magnetic environment of Saturn's largest moon Titan. The main instrument utilised is the Cassini Plasma Spectrometer – Electron Spectrometer (CAPS-ELS). Following the presentation of relevant background information, the first part of the thesis is concerned with the analysis of electrons in Titan's ionosphere and exosphere, whereas in the second part we investigate observations of organic negative ions that can reach masses as high as 13,800 amu/q.

The first of two electron topics is the study of photoelectrons in Titan's ionosphere. We report on observations of photoelectrons (Coates et al., 2007a) in Titan's exosphere and ionospheric tail that were created in Titan's lower sunlit ionosphere. We compare observations to hybrid model results (Sillanpää et al., 2011) to confirm that photoelectrons can travel to these locations via magnetic field lines and discuss the implications for Titan's ionospheric environment and magnetic tail.

In the second electron topic we explore regions in Titan's topside ionosphere where electrons undergo a change in energy of up to 100 eV. These events are observed predominantly on the hemisphere of Titan where the electric field of Saturn's corotating magnetospheric plasma points away from the moon. A number of events also appear to be associated with pick up ions.

The negative ion part of this thesis describes the investigation of factors that control the masses and number densities of negative ions (Coates et al., 2007b, 2009). These have been observed in the altitude range 950 – 1400 km which makes up the main part of Titan's ionosphere. We find that the highest masses and densities are observed at the lower altitudes within this range. In addition, we reveal solar zenith angle trends for different mass groups, including a region of predominantly low densities near the day-night terminator.

Table of Contents

List of Figures

List of Tables

List of Papers

1. Coates, A.J., **A. Wellbrock**, G.R. Lewis, C.S. Arridge, F.J. Crary, D.T. Young, M.F. Thomsen, D.B. Reisenfeld, E.C. Sittler Jr, R.E. Johnson, K. Szego, Z. Bebesi, G.H. Jones, Cassini in Titan's tail: CAPS observations of plasma escape, J. Geophys. Res., 117, A05324, doi:10.1029/2012JA017595, May 2012.
2. **Wellbrock, A.**, A. J. Coates, I. Sillanpää, G. H. Jones, C. S. Arridge, G. R. Lewis, D. T. Young, F. J. Crary, and A. D. Aylward (2012), Cassini observations of ionospheric photoelectrons at large distances from Titan: Implications for Titan's exospheric environment and magnetic tail, J. Geophys. Res., 117, doi:10.1029/2011JA017113, Mar 2012.
3. Coates, A.J., J.-E. Wahlund, K. Ågren, N. Edberg, J. Cui, **A. Wellbrock** and K. Szego, Recent results from Titan's ionosphere, Space Science Reviews, Volume 162, Issue 1-4, pp. 85-111, DOI 10.1007/s11214-011-9826-4.
4. Ma, Y.J., C.T. Russell, A. F. Nagy, G. Toth, M. K. Dougherty, **A. Wellbrock**, A. J. Coates, P. Garnier, J-E. Wahlund, T. E. Cravens, M. S. Richard, F. J. Crary, The importance of thermal electron heating in Titan's ionosphere: Comparison with Cassini T34 flyby, J. Geophys. Res., 116, A10213, doi:10.1029/2011JA016657.
5. Németh, Z., K. Szego, Z. Bebesi, G. Erdos, L. Foldy, A. Rymer, E. C. Sittler, A. J. Coates, and **A. Wellbrock** (2011), Ion distributions of different Kronian plasma regions, J. Geophys. Res., 116, A09212, doi:10.1029/2011JA016585.
6. Coates, A.J., S.M.E. Tsang, **A. Wellbrock**, R.A. Frahm, J.D. Winningham, S. Barabash, R. Lundin, D.T. Young and F.J. Crary, Ionospheric photoelectrons: comparing Venus, Earth, Mars and Titan, Planet. Space Sci. 59 (2011), 1019-1027, doi:10.1016/j.pss.2010.07.016, Aug 2011.
7. Wei, H.Y., C. T. Russell, M. K. Dougherty, Y. J. Ma, K. C. Hansen, H. J. McAndrews, **A. Wellbrock**, A. J. Coates, M. F. Thomsen, D. T. Young, Unusually strong magnetic fields in Titan's ionosphere: T42 case study, Advances in Space Research, 48, 314-322, Jul 2011.
8. Michael, M., S.N. Tripathi, P. Arya, A. Coates, **A. Wellbrock**, and D.T. Young, High-Altitude Charged Particles in the atmosphere of Titan, Planet Space Sci., 59, 880-885, Jul 2011.
9. Ågren, K., D. J. Andrews, S. C. Buchert, A. J. Coates, S. W. H. Cowley, M. K. Dougherty, N. J. T. Edberg, P. Garnier, G. R. Lewis, R. Modolo, H. Opgenoorth, G. Provan, L. Rosenqvist, D. L. Talboys, J.-E. Wahlund, and **A. Wellbrock**, Detection of currents and associated electric fields in Titan's ionosphere from Cassini data, J.Geophys.Res., 116, CiteID A04313, April 2011
10. Edberg, N.J.T., K. Ågren, J.-E. Wahlund, M.W. Morooka, D.J. Andrews, S.W.H. Cowley, **A. Wellbrock**, A.J. Coates, C. Bertucci and M.K. Dougherty, Structured ionospheric outflow during the Cassini Titan Flybys T55-T59, Planet. Space Sci., 59, 788-797, Jun 2011.
11. Coates, A.J., **A. Wellbrock**, G.R. Lewis, G.H.Jones, D.T. Young, F.J. Crary, J.H. Waite, R.E. Johnson, T.W. Hill, E.C. Sittler Jr., Negative ions at Titan and Enceladus: recent results, Faraday Disc., 147(1), 293-305, DOI: 10.1039/C004700G2010, Nov 2010.

12. Galand, M., R. Yelle, J. Cui, J. Wahlund, V. Vuitton, **A. Wellbrock**, and A. Coates (2010), Ionization sources in Titan's deep ionosphere, J. Geophys. Res., 115, A07312, doi:10.1029/2009JA015100, Jul 2010.
13. Coates, A.J., G.H. Jones, G.R. Lewis, **A. Wellbrock**, D.T.Young, F.J. Crary, R.E. Johnson, T.A. Cassidy, T.W. Hill, Negative Ions in the Enceladus Plume, Icarus, 206, 618-622, doi:10.1016/j.icarus.2009.07.013, Apr 2010.
14. Wei, H.Y., C.T. Russell, **A. Wellbrock**, M.K. Dougherty and A.J. Coates, The plasma environment at Titan's orbit with Titan present and absent, Geophys. Res. Lett., 36, L23202, doi:10.1029/2009GL041048, Dec 2009.
15. Arridge, C.S., H.J. McAndrews, C.M. Jackman, C. Forsyth, A.P. Walsh, E.C. Sittler, L.K. Gilbert, G.R. Lewis, C.T. Russell, A.J. Coates, M.K. Dougherty, G.A. Collinson, **A. Wellbrock**, D.T. Young, Plasma electrons in Saturn's magnetotail: structure, distribution and energisation, Planetary and Space Science, Volume 57, Issues 14-15, December 2009, Pages 2032-2047, doi:10.1016/j.pss.2009.09.007, online Sep print Dec 2009.
16. Coates, A.J., **A. Wellbrock**, G.R. Lewis, G.H. Jones, D.T. Young, F.J. Crary, J.H. Waite Jr., Heavy negative ions in Titan's ionosphere: altitude and latitude dependence, Planet. Space Sci., 57, Issues 14-15, 1866-1871, doi:10.1016/j.pss.2009.05.009, (online May, print Dec) 2009.
17. Vuitton, V., P. Lavvas, R.V. Yelle, M. Galand, **A. Wellbrock**, G.R. Lewis, A.J. Coates and J.-E. Wahlund, Negative ion chemistry in Titan's upper atmosphere, Planetary and Space Science, Volume 57, Issue 13, 1558-1572, doi:10.1016/j.pss.2009.04.004, online Apr published Nov 2009.
18. Jones, G.H., C. S. Arridge, A. J. Coates, G. R. Lewis, S. Kanani, **A. Wellbrock**, D. T. Young, F. J. Crary, R. L. Tokar, R. J. Wilson, T. W. Hill, R. E. Johnson, D. G. Mitchell, J. Schmidt, S. Kempf, U. Beckmann, C. T. Russell, Y. D. Jia, M. K. Dougherty, J. H. Waite Jr., B. Magee, Fine jet structure of electrically-charged grains in Enceladus' plume, Geophys Res Letters, vol 36, L16204, doi:10.1029/2009GL038284, Sep 2009
19. Rymer, A. M., H. T. Smith, **A. Wellbrock**, A. J. Coates, and D. T. Young (2009), Discrete classification and electron energy spectra of Titan's varied magnetospheric environment, Geophys. Res. Lett., Volume 36, Issue 15, CiteID L15109, doi:10.1029/2009GL039427, Aug 09
20. Ma, Y.J., C. T. Russell, A. F. Nagy, G. Toth, C. Bertucci, M. K. Dougherty, F. M. Neubauer, **A. Wellbrock**, A. J. Coates, P. Garnier, J-E. Wahlund, T. E. Cravens, F. J. Crary, Real-time Global MHD Simulations of Cassini T32 Flyby: from Magnetosphere to Magnetosheath, J. Geophys. Res., 114, A03204, doi:10.1029/2008JA013676, Mar 2009.
21. Cravens, T.E., I. P. Robertson, J. H. Waite Jr., R. V. Yelle, V. Vuitton, A. J. Coates, J.-E. Wahlund, K.Ågren, M. S. Richard , V. De La Haye, **A. Wellbrock**, F. M. Neubauer, Model-Data Comparisons for Titan's Nightside Ionosphere, Icarus, Volume 199, Issue 1, p. 174-188, doi: 10.1016/j.icarus.2008.09.005, 2009.

1. Introduction

1.1. Introducing concepts in space plasma physics

In this first introductory chapter we discuss the basics of space plasma physics. A large amount of this introductory material is based on material from Baumjohann and Treumann (1997), Cravens (2004) and Kivelson and Russel (1995).

1.1.1. What is a plasma?

A plasma is a collection of 'free' positive and negative charges that is quasi-neutral on a macroscopic scale. Any external influences are acted on collectively to maintain this neutrality. However, on a microscopic scale, defined by the Debye length which we discuss shortly, charges act as individual particles.

Plasma makes up almost all visible matter in the universe, from fluorescent light tubes and lightning on Earth, planetary ionospheres, the sun and its solar wind to accretion disks around binary stars and black holes.

A charged particle is influenced by surrounding electric fields, and exerts its own electric field on other particles. The potential is given by the Coulomb potential, Φ_C:

$$\Phi_C = \frac{q}{4\pi\varepsilon_0 r}$$

Equation 1

where q is the charge of the particle, ε_0 is the permittivity of free space and r is the distance from the charge. If a charged particle enters a plasma, the neutrality of the plasma is offset and hence the charges in the plasma react and move to 'shield' the

new particle such that the plasma can be in a state of neutrality again. As a result, the potential in a plasma is the Debye potential, Φ_D:

$$\Phi_D = \frac{q}{4\pi\varepsilon_0 r}\exp\left(-\frac{r}{\lambda_D}\right)$$

Equation 2

where λ_D is the above mentioned Debye length. It is the distance over which charges can suppress the Coulomb potential by a factor of e and is given by

$$\lambda_D = \sqrt{\left(\frac{\varepsilon_0 k_B T_e}{n_e e^2}\right)}$$

Equation 3

where k_B is the Boltzmann constant, T_e is the electron temperature, n_e is the electron density, and e is the electron charge. One condition for an ionised medium to be considered a plasma is the *quasineutrality condition*. It states that

$$L >> \lambda_D$$

Equation 4

where *L* represents typical length scales of the macroscopic plasma properties. The sphere with the Debye length as the radius is called the Debye sphere. Another plasma condition is the *collective behaviour condition*:

$$N_D = \frac{4}{3}\pi\lambda_D{}^3 n >> 1$$

Equation 5

where N_D is the number of charged particles within the Debye sphere, such that enough particles are present around a specific charge concentration to shield it.

When the particles in a plasma react to an external force that is causing a perturbation, electrons respond most quickly because they are smaller and hence more mobile than ions. This results in a natural oscillation of the electrons about the ions at the *plasma frequency* ω_{pe}:

$$\omega_{pe} = \sqrt{\frac{n_e e^2}{m_e \varepsilon_0}}$$

Equation 6

where m_e is the electron mass. The plasma frequency is an important characteristic timescale and can be used to describe the third plasma condition, the *collision condition*:

$$\omega_{pe}\tau_n >> 1$$

Equation 7

where τ_n is the time period between collisions with neutrals.

1.1.2. Theoretical approaches to describing plasma

The dynamics of a plasma are complex because the charged particles interact with electric and magnetic fields due to external forces in addition to the fields generated by the particles themselves as they are in motion. In this subsection we describe some of approaches that can be used to describe the dynamics of a plasma.

1.1.2.1. Single particle motion

In single particle motion, electrons and ions are treated independently and the laws of mechanics and electromagnetism are applied to each particle. The main

assumption in this approach is that particles do not interact directly; electromagnetic fields produced within the plasma are not considered and hence collective efforts are not taken into account. Single particle motion can be applied to tenuous plasmas or for example the energetic particles in the radiation belts.

The force acting on a moving particle subjected to electric and magnetic fields is given by the Lorentz force:

$$\mathbf{F}_{\mathrm{L}} = q(\mathbf{E} + \mathbf{v} \times \mathbf{B})$$

Equation 8

Uniform magnetic field

In the presence a uniform magnetic field with **E** = 0, Equation 8 can be written as

$$m\frac{d\mathbf{v}}{dt} = q\mathbf{v} \times \mathbf{B}$$

Equation 9

Differentiation over time gives

$$\frac{d^2\mathbf{v}}{dt^2} = -\left(\frac{qB}{m}\right)^2 \mathbf{v}$$

Equation 10

The force acting on the particle is perpendicular to both **v** and **B**, hence no work is done because there is no motion in the direction of the force.

If the velocity component that is parallel to the magnetic field is zero, the resulting motion is a cyclical path perpendicular to **B**. If there is a nonzero parallel component then the motion follows a helicoidal path. From Equation 10, the

angular frequency of this simple harmonic motion is referred to as the *gyrofrequency* ω_g, the *Larmor frequency* or *cyclotron frequency*:

$$\omega_g = \frac{qB}{m}$$

Equation 11

The motion occurs about a central point called the *guiding centre* which follows a path parallel to the magnetic field and travels at a speed of the parallel velocity component. The cyclical motion about the guiding centre has a radius called the *gyroradius* r_g which is also known as the *Larmor radius* or *cycloton radius*:

$$r_g = \frac{mv_\perp}{qB}$$

Equation 12

where $v_\perp$ is the perpendicular velocity component and the time for one revolution is called the *gyroperiod*.

Figure 1: Gyromotion of charged particles in a plasma due to a uniform magnetic field only (from Baumjohann & Treumann, 1997).

This motion is described as *gyrotropic motion* and is demonstrated in Figure 1. As a result of the mass and charge dependence in Equation 12, the electrons and ions will gyrate about the gyrocentre in opposite senses with different gyroradii.

The *pitch angle* α is defined as

$$\alpha = \tan^{-1}\left(\frac{v_\perp}{v_{||}}\right)$$

Equation 13

and depends on the ratio of the perpendicular and parallel velocity ($v_{//}$) components.

Near planetary surfaces and locations where fields converge, the Lorentz force (q**v** x **B**) can have a component which is negative in the direction of the increasing field strength. This tends to reduce the parallel component of a particle's velocity to an extent that the motion along the field line ceases (Figure 2). This is described as a *mirror point*, from which the particle returns along the field line until another mirror point is reached for example at the other end of the planetary dipole field line. The process is known as *magnetic mirroring*.

Figure 2: Magnetic mirroring. A particle's parallel velocity can reach zero and return along the magnetic field line when magnetic field lines are converging as shown in this example (from Baumjohann & Treumann, 1997).

Due to the total speed staying constant, the perpendicular component increases as the parallel component decreases. The first adiabatic variant states that

$$\frac{v_{\|}^{\,2}}{R} = const$$

Equation 14

which can be used to find an expression relating the mirror point as a function of pitch angle:

$$B_m = \frac{B}{\sin^2 \alpha}$$

Equation 15

Where B_m is the magnetic field at the mirror point and B is the magnetic field at a given point, for example at the equator. The mirror point therefore only depends on the pitch angle and magnetic field at a specific point and is independent of the type of particle or its kinetic energy.

Uniform magnetic and electric field

If we now add a non-zero uniform electric field as in Equation 8, an extra motion is introduced. Electrons are very mobile along magnetic field lines, hence they can react almost instantly to cancel out any electric field components parallel to the magnetic field. However, the perpendicular component of the electric field will cause the guiding centres of charged particles to drift in a direction perpendicular to both the electric and magnetic fields according to the ***E*** $\times$ ***B*** *drift:*

$$\mathbf{v}_{\mathbf{E}\times\mathbf{B}} = \frac{\mathbf{E}\times\mathbf{B}}{B^2}$$

Equation 16

This velocity is now independent of mass and charge, therefore the drift direction is the same for both ions and electrons and is superimposed on the gyromotion due to the magnetic field, as demonstrated in Figure 3.

Figure 3: Trajectories of an ion and an electron as a result of **ExB** drift (from Baumjohann & Treumann, 1997).

Non-uniform magnetic field

An inhomogeneous magnetic field means that the field has gradients and the field lines can be curved, which is typical in planetary magnetospheres. This introduces additional drift motions such as *gradient drift* and *curvature drift*.

Gradient drift is the result of a weakly inhomogeneous magnetic field. It is perpendicular to both the magnetic field and its gradient:

$$\mathbf{v}_{\nabla} = \frac{m v_{\perp}^{2}}{2qB^{3}}(\mathbf{B} \times \nabla \mathbf{B})$$

Equation 17

A current is generated as a result of electrons and ions drifting in opposite directions, called *gradient drift current* and is shown in Figure 4.

Figure 4: Gradient drift (from Baumjohann & Treumann, 1997).

When curved magnetic field lines are present, a centripetal force acts on the particles that depends on the radius $\mathbf{R}_C$ of the curvature which points away from the centre of curvature, causing *curvature drift* (Figure 5):

$$\mathbf{v}_{R} = \frac{m v_{\parallel}^{2}}{q} \frac{\mathbf{R}_{\mathrm{C}} \times \mathbf{B}}{R_{C}^{2} B^{2}}$$

Equation 18

Again, electrons and ions drift in opposite directions and hence a *curvature drift* current is created.

Figure 5: Curvature drift (from Baumjohann & Treumann, 1997).

Gradient and curvature drifts strongly depend on the parallel and perpendicular velocity components, respectively. These drifts are therefore particularly important in regions where very energetic particles are found, such as the radiation belts.

1.1.2.2. Many particle motion

Kinetic theory

Collective behaviour is important in many plasmas. Magnetic fields are generated by moving charges, which influence all other particles in the structure. Some particles may in turn create or change their electric and magnetic fields, resulting in complex reactions and feedback chains that cannot be simulated even by powerful computers. One approach to solve this problem is *kinetic theory* which uses a statistical approach to treat the particles as a group. Kinetic theory can be used for non-isotropic distributions which deviate from Maxwellians such as loss cone distributions, trapped particle distributions (which peak at 90°), and ring and shell distributions (relevant during ion pick-up).

Kinetic theory is based on describing the distribution of particles among velocities throughout space. This is done by assigning the position and velocity to each particle at each point in time, in order to describe the state of the plasma. These are taken as independent coordinates in a hypothetical six-dimensional (3 space and 3 velocity) space called *phase space* and their distribution is given by f = f(r, v, t) at a given position r and time t where f is called the particle distribution function (PDF). The phase space density (PSD) is the number of particles in a volume element of phase space:

$$dn = f(\mathbf{r},\mathbf{v},t)d\mathbf{v}_x d\mathbf{v}_y d\mathbf{v}_z$$

Equation 19

Integrating over three-dimensional velocity space gives the moments of the particle distribution:

$$\mathbf{M}(\mathbf{r},t) = \int \mathbf{v}^n f(\mathbf{r},\mathbf{v},t)d\mathbf{v}_x d\mathbf{v}_y d\mathbf{v}_z$$

Equation 20

Where *n* represents the order of the moment. *n* = 0 gives the 0^{th} order moment: density. The first and second order moments are temperature and velocity, respectively.

Fluid theories

Instead of following the detailed changes of distribution functions, another approach to treating particles as a group in a plasma is using a fluid description. In *magnetohydrodynamics (MHD)*, the plasma is treated as a single conducting fluid over a macroscopic scale only. MHD applies both Maxwell's equations and the Navier-Stokes equations of fluid dynamics to a plasma but is only accurate when time scales are slow compared with characteristic plasma time scales like particle gyration and oscillation periods. Length scales also need to be long compared to particle gyroradii and Debye lengths. Ideal MHD is applicable when we can assume that the fluid is a perfect electrical conductor and when the effects of magnetic advection are much greater than magnetic diffusion. It is appropriate to use MHD in space plasma environments with large physical scales and long timescales when the individual particle motion is not important and when the ion mass is well represented by an average mass across the simulated volume such as large scale aspects of the solar wind and planetary magnetospheres. MHD can generally be used reasonably well to simulate induced magnetospheres of unmagnetised objects such as Mars, Venus and Titan, however a limiting factor can be the size of the ion gyroradii. These can sometimes be of similar size to typical length scales of the system, namely the radius of the planet or moon.

In addition, there are some other fluid ways of describing plasmas, such as *multi-fluid theory* which uses different types of particles such as electrons and major ions, as separate species. This is effective when species react differently to disturbances in the plasma.

Frozen-in theorem

The current, **J**, in a conductive medium is given by Ohm's law:

$$\mathbf{J} = \sigma_O(\mathbf{E} + \frac{\mathbf{v} \times \mathbf{B}}{c})$$

Equation 21

where σ_O is the conductivity of the plasma, **v** is the plasma velocity, and *c* is the speed of light. In a highly conducting plasma, such as the solar wind or magnetospheric plasmas,

$$\frac{\mathbf{J}}{\sigma_O} \approx 0$$

therefore

$$\mathbf{E} - \frac{\mathbf{v} \times \mathbf{B}}{c} = 0$$

Equation 22

This means that the magnetic fields are carried with the plasma and the magnetic field lines are 'frozen into' the fluid. Hence a particular parcel of plasma stays attached to the field lines of the plasma (Cravens, 2001, De Pater and Lissauer, 2001).

1.2. Introducing Titan

Saturn's largest moon Titan is a unique object in the solar system. It has a nitrogen based atmosphere and is in many ways the most Earth-like body known. It was discovered in 1655 by Dutch astronomer Christiaan Huygens and was named *Titan* by John Herschel in 1847 after the immortal giants in Greek mythology because it was believed to be the largest moon in the solar system.

Voyager 1 and 2 made one Titan pass each on 12 November 1980 and 26 August 1981 at a distance of 3,915 km and 666,190 km, respectively. They found a cold world with an estimated surface temperature of 94 K and a plethora of organic molecules based on the two main atmospheric volatiles nitrogen (97%) and methane (1.5 – 3 %) (Broadfoot et al., 1981, Hanel et al., 1981, Strobel et al., 2009). Voyager 1 results also demonstrated that Titan's solid body is actually slightly smaller than Jupiter's giant moon Ganymede; Titan's massive extended atmosphere and orange haze layers impenetrable by almost all visible light were revealed and had made the moon appear larger. Nevertheless, with a radius of 2575 km it is not only the second largest moon in the solar system but it is also larger than the planet Mercury. In addition, Titan is the only moon in the solar system with a substantial atmosphere, which exceeds the surface pressure on Earth by 50%.

With the arrival of Cassini-Huygens in the Saturn system in 2004, Titan has been studied extensively (Brown et al., 2009). Huygens landed on Titan successfully on 14 January 2005, revealing for the first time the geologically active surface of the enigmatic moon. Many Earth-like features were soon confirmed: Titan is the only body in the solar system other than Earth with surface lakes and has a methane cycle similar to the hydrological cycle on Earth with evaporation, clouds and rain (Atreya et al., 2009). Cryovolcanism, dendritic erosion patterns, dune fields, small scale gullies, rounded cobbles and mountain ranges indicate dynamic surface processes (Jauman et al., 2009).

Figure 6: Top panel: Haze-enshrouded Titan behind smaller moon Epimetheus and Saturn's A and F rings. The colour information is artificial (NASA/JPL/University of Arizona image PIA07786). Bottom-left: False colour composite of several images during separate Titan flybys T19 and T20. The image was taken using the VIMS spectrometer aboard Cassini and constructed from three wavelengths in the infrared which can penetrate Titan's haze layers (NASA/JPL/University of Arizona image PIA09034). Bottom-middle: Natural colour image view of Titan (NASA/JPL/University of Arizona image PIA07729). Bottom right: Natural colour image of Titan's upper atmosphere. The haze layers in the upper part scatters blue and UV wavelengths, whereas the orange haze layers absorb 90% of all visible light (NASA/JPL/University of Arizona image PIA09034).

Titan orbits Saturn at a distance of approximately 20 R_S ($R_S \approx 60268$ km = Saturn's radius) and is tidally locked in synchronous rotation with Saturn. Hence Titan's orbital period is identical to its rotation period which is approximately 16 days, and the same hemisphere of Titan always faces Saturn. This also means that Titan experiences the same seasons as Saturn, which are long compared to Earth's seasons: One Saturn year is approximately 29.5 Earth years. Titan's seasons are shown in Figure 7.

Figure 7: Orbital motion of Saturn and Titan around the Sun showing their seasons in the Northern hemispheres and some spacecraft mission information of Voyager 1, Cassini and Huygens. (Adapted from Tokano et al., 1999)

Titan's atmospheric structure is shown in Figure 8. Most terrestrial planets in the solar system do not have a stratosphere because there is no temperature inversion just above the troposphere. At Earth, this increase in temperature with height in the stratosphere is caused by ozone heating, whereas there is no such 'ozone equivalent' that heats the atmosphere at planetary bodies such as Venus, Mars, Triton and Pluto. However, on Titan the ozone equivalent particles are made up of a number of different gases and aerosols (Muller-Wodarg et al., 2000, Coustenis and Taylor, 2008). Therefore the thermal structure of Titan's atmosphere can be subdivided into the same regions as those of the Earth's atmosphere. The first temperature minimum of around 70 K occurs at an altitude of around 40 km (the *tropopause*) (Fulchignoni et al., 2005). The temperature then rises to 180 K at

around 300 km at the *stratopause* and decreases again in the *mesosphere* until the *mesopause* at around 500 km. Titan's thermosphere reaches altitudes of approximately 1400 km at the *exobase*. The exobase marks the upper boundary of the atmosphere; above it particles become dominantly collisionless in a region called the *exosphere*. The atmosphere also contains several haze layers which can be found at approximately 200, 375 and 500 km altitudes. Titan's atmospheric structure and composition is reviewed in more detail by Strobel et al. (2009).

Figure 8: Titan's different atmospheric regions as recorded by HASI (Huygens atmospheric structure instrument) onboard the Cassini-Huygens lander (Observatoire de Paris).

1.3. Plasma interactions in the solar system

In this section we first review interactions of plasmas with planetary bodies in the solar system and then discuss Titan's unique interaction including its plasma environment.

1.3.1. Solar wind interaction with magnetised planets

Planets which generate their own significant magnetic field are surrounded by a region called the *magnetosphere* (Bagenal, 2000). In this region the behaviour of charged particles are dominated by the magnetic field of the planet. Planetary magnetospheres in the solar system interact with a plasma originating from the Sun called the solar wind. It consists of electrons and ions of which on average 95% are protons (H^+), 4% alpha particles (He^{++}) and other ions such as carbon, nitrogen and oxygen.

The solar wind is deflected around planetary magnetospheres which can be thought of as magnetic cavities. We use Saturn as an example of a magnetised planet because Titan spends most of its time within Saturn's outer magnetosphere. Figure 9 shows a three dimensional schematic of Saturn's magnetosphere. The solar wind is slowed down at a bow shock from supersonic to subsonic speeds upstream of the planet, and is compressed and heated. A bow shock only forms when the external plasma travels at supersonic speeds, which is virtually always the case with the solar wind at Saturn. The region between the bow shock and the planet's magnetosphere is called the *magnetosheath*. The boundary between this shocked solar wind and the magnetosphere is referred to as the *magnetopause* (marked in Figure 9). A simple estimate of the magnetopause (MP) distance from the planet at the subsolar point can be calculated using pressure balance (Kanani et al., 2010). The dominant pressure exerted on Saturn's magnetosphere is the solar wind dynamic pressure (ρu^2, where ρ is the solar wind mass density and u the solar wind velocity) and is assumed to be in equilibrium with the magnetosphere's magnetic pressure ($B^2/2\mu_0$ where μ_0 is the permeability of free space).

In reality, frequently changing conditions keep the magnetopause in constant motion. The solar wind dynamic pressure changes over time due to e.g. coronal mass ejections (CMEs) and corotating interaction regions (CIRs) (e.g. Jackman et al., 2005). Magnetic reconnection (McAndrews et al., 2008) may also affect the MP location. Saturn has many sources of plasma such as its rings and moons (especially Enceladus) (e.g. Kivelson, 2006) which contribute considerably to the magnetospheric configuration and result in a changing hot plasma pressure component. A typical subsolar magnetopause distance is $22R_S$; c.f. Titan's orbit is at 20 R_S. The location of Saturn's magnetopause can determine what environment Titan is exposed to: the supersonic solar wind upstream of the bow shock, the shocked solar wind in the magnetosheath, or the magnetospheric plasma inside the magnetosphere. This is discussed further in section 1.3.3.

Figure 9: Schematic 3D illustration of Saturn's magnetosphere (courtesy Bagenal/University of Colorado).

The magnetic field carried by the solar wind couples with that of the magnetosphere and stretches out into a long *magnetotail*. This region contains tail *lobes* which are separated by a *plasma* (or *current*) *sheet*. The lobes are a region of low density plasma and a strong magnetic field, whereas the plasma sheet contains hot, high density plasma and the magnetic field is low.

The gas giants and Earth are other examples of magnetised planets in the solar system which have a substantial magnetosphere. There are two general types of magnetospheric configurations. In the case of Earth, it is the called the *Dungey cycle* (Dungey, 1961). The Earth is a slow rotator and only has a small internal mass source (the high latitude ionosphere, 1kg/s), therefore the Dungey cycle is controlled by the solar wind and enabled by reconnection which occurs on the dayside and also in the tail. The Earth's corotation electric field is only dominant over the solar wind electric field close to the planet. The other magnetospheric interaction mechanism is called the Vasyliunas cycle (Vasyliunas, 1983) and the prime example is the Jupiter magnetosphere. Jupiter is a fast rotator with a very strong magnetic field and there are considerable plasma sources inside the magnetosphere (1000kg/s, the most important source being Jupiter's volcanic moon Io). This interaction is therefore driven internally; plasma mass loading is important and combined with strong centrifugal forces due to the rapid rotation, the field lines stretch to the tail where magnetic reconnection occurs (Gombosi et al., 2009). Jupiter's corotation electric field is much stronger than that of the solar wind.

The case of Saturn is somewhere between Earth and Jupiter. While Saturn is a fast rotator and has reasonable internal plasma sources (300kg/s, with the moon Enceladus being a dominant source), its magnetic field is not by far as strong as

Jupiter's. Saturn therefore exhibits both Dungey and Vasyliunas cycle characteristics (Cowley et al., 2004).

1.3.2. Plasma interactions with unmagnetised objects

When a planet or moon does not generate its own global magnetic field, the solar wind or external plasma will interact directly with the body's atmosphere or surface. The type of interaction depends on the electrical conductivity of the body and the type of atmosphere or exosphere present.

Bodies without an atmosphere

The interaction of an external plasma with objects that do not posses an atmosphere or only a very tenuous exosphere and a surface of low conductivity, such as the Earth's moon, rocky asteroids and some other satellites in the solar system, do not carry sufficient current to deflect the external plasma. Hence there is a direct interaction and the plasma is absorbed by the surface. The region immediately downstream of the object, called the wake, forms a plasma cavity, which is filled further downstream.

Figure 10: Schematic illustration of the solar wind interaction with an unmagnetised satellite that has no atmosphere such as the Earth's moon (adapted from Bagenal, 2001).

Bodies with an atmosphere

In the case of unmagnetised objects such as Venus and Mars with a significant atmosphere, the obstacle to the plasma flow is a highly conductive ionosphere

through which electrical currents can flow. An ionosphere is a partially ionised layer of a planetary object's atmosphere which is discussed in more detail in section 1.4. When the magnetic field lines carried by the external plasma try to penetrate the ionosphere, currents in the ionosphere are set up which flow out to the magnetospheric plasma. As a result, forces are created which slow and divert the incident flow. The result of these ionospheric pressure forces is the formation of an *induced* magnetosphere similar to the intrinsic magnetospheres described in the previous section. The magnetic field lines of the solar wind drape around the planet and stretch out downstream to form a magnetotail. The pressure boundary that separates the ionospheric plasma from the solar wind is called the *ionopause*, which is where, similar to the magnetopause at magnetised planets, the pressure of the upstream flow balances the pressure in the ionosphere (Arridge et al., 2011). A bow shock forms upstream of the planet, provided the external plasma travels at supersonic velocities.

Figure 11: Schematic illustration of the solar wind interaction with an unmagnetised planet which has an atmosphere, such as Venus and Mars (adapted from Bagenal, 2001).

Comets

The solar wind interaction with comets (Coates and Jones, 2009) is similar to the interaction with unmagnetised planets such as Venus and Mars, however there are some differences. The nuclei of comets are much smaller than planets. Gravity is therefore not important and the region occupied by the cometary gas depends on the speed of expansion and the ionisation time (Russell, 1991). As a result the actual interaction region is larger than that of Venus or Mars, and the interaction itself is more gradual. A weaker bow shock is usually observed. The boundary between the shocked solar wind and the induced magnetosphere is called *cometopause*.

The main reason this induced magnetosphere forms is due to a process called *mass loading*. As the solar wind approaches, it ionises neutral particles from the comet's exosphere on the ram side. These particles were initially unaffected by the electric and magnetic fields of the impinging plasma. However, now carrying a charge, they are *picked up* by the plasma and their movement is controlled by the fields due to the magnetospheric plasma. This process is known as *ion pick up*. As a result, the mass of the plasma on the ram side increases. In order to conserve angular momentum, the plasma slows down at these *mass loading* sites. However, the plasma flow continues unhindered further from the comet. Due to the frozen-in theorem (see section 1.1.2.2), the magnetic field lines are forced to drape around the obstacle. A magnetic barrier forms upstream due to the pile up of magnetic flux. As the field lines enter the downstream side, the draping increases until the tension pulls them away from the ionosphere. The loaded plasma then leaves the comet along the tail. Mass loading is a common feature in the interactions of plasmas with unmagnetised bodies that have atmospheres and/or exospheres and is also present in the Mars and Venus interactions. However, in the latter cases the ionospheric pressure forces are more important than at comets in forming the induced magnetosphere and the magnetic field line draping.

Satellites inside planetary magnetospheres

Plasma interactions with unmagnetised objects also occur inside the magnetospheres of the gas giants. The magnetospheric plasmas interact with the planet's satellites that are located within the magnetospheres. These interactions range from plasma surface interactions similar to the solar wind interaction with the Earth's moon, to cometary type mass loading based interactions and can even include some features of the Venus type interactions. Ganymede, the largest moon in the solar system, even produces its own magnetic field, therefore it possesses a magnetosphere within Jupiter's magnetosphere (Kivelson et al., 1996).

1.3.3. Titan's plasma interaction and environment

Titan orbits Saturn at approximately 20 R_S which is located in the outer part of Saturn's magnetosphere under typical solar wind dynamic pressure. There are some important features as a result of this location that we will now explore. Close to Saturn, the planet's magnetospheric plasma almost co-rotates with Saturn's rotation which is approximately 10.6 hours. At a distance of 20 R_S from Saturn, the plasma tends to subcorotate - it lags behind the near-corotation of the inner magnetospheric plasma and travels at velocities around 120 km s^{-1} which is just below the magnetosonic velocity (Schunk and Nagy, 2009) but 170 km s^{-1} velocities can be reached (Thompson et al., 2010, Arridge et al., 2012).

Titan's orbit around Saturn is shown in Figure 12. Saturn is in the centre of the figure, and shown are the magnetopause and bow shock locations of its interaction with the solar wind arriving from the left at 12:00 Saturn Local Time (SLT). Titan's orbit is marked by the dashed circle with a few orbital example locations. Titan's orbital motion is anticlockwise in this figure, as indicated by the arrows. Saturn's rotation period (10.6 hours) is much shorter than Titan's orbital period (≈ 16 days). Even though the magnetospheric plasma subcorotates with the planet it is still much faster than Titan and therefore continuously impinges on Titan's trailing edge, which is referred to as the *ram side* or *upstream side*. In Figure 12 we can also see the solar wake (marked in orange) which is Titan's nightside, and the magnetospheric corotation wake (marked in green). The direction of the corotation wake in this figure is the nominal direction which would be expected from Titan's orbit around Saturn. We therefore call this the *nominal* corotation wake. As we shall see later (e.g. chapter 3, case T17), the corotation wake is sometimes observed at an angle to the expected nominal wake direction.

Figure 12: Titan's orbit around Saturn, showing the nominal magnetospheric corotation wake in green and the solar wake (night side) in orange (adapted from Coates (2009)). The angle α indicates the *solar incidence-ram-angle (SRA)* which is the angle between the solar wake and the nominal corotation wake.

Titan lacks a significant intrinsic magnetic field (Neubauer et al., 1984). Recent Cassini observations have revealed a dipole moment of 0.78 ± 2.2 nT R_T^3 (Wei et al., 2010) which is consistent with the earlier Voyager based reports of Titan being unmagnetised.

Titan is the only moon in the solar system that has a substantial atmosphere, which includes a highly conductive ionosphere. Its plasma interaction therefore falls in the Venus type interaction category. However, mass loading is also an important process due to Titan's extended exosphere, contributing to the deceleration and deflection of the flow before (several R_T upstream) ionospheric pressure forces become stronger closer to the moon's ionosphere. Therefore Titan's interaction also resembles the cometary type in some ways. The impinging magnetospheric plasma travels at mostly subsonic speeds, therefore a bow shock has not been observed to date, however it may be possible for a weak bow shock to form when the magnetospheric plasma flow reaches velocities higher than the magnetosonic flow which is near 120 $km.s^{-1}$ (Schunk & Nagy, 2009). The lack of a bow shock is the main difference to the Venus and cometary type interactions. Key features of the Titan interaction are shown in Figure 13. A size comparison of the different intrinsic and induced magnetospheres is shown in Figure 14.

Figure 13: Titan's interaction with Saturn's magnetospheric plasma ('corotation flow'). The convection electric field **E** of the magnetospheric corotation flow depends on the magnetospheric corotation velocity **v** and magnetic field **B** as shown (adapeted from Blanc et al., 2002).

Figure 14: Size comparison of different intrinsic and induced magnetospheres in the solar system. The four panels on the left show the magnetised bodies and magnetopause and bow shock positions. The panels on the right show the unmagnetised interactions with bow shock positions only. The comets shown are Halley (H), Giacobini-Zinner (GZ), Borrelly (B) and Grigg-Skjellerup (GS). In the case of Pluto, Charon's orbit is indicated by a

circle and bow shock positions **a** and **b** refer to aphelion and perihelion (from Coates et al., 2001 with Titan added by Coates in 2008).

The two main ionisation sources of Titan's ionosphere are solar radiation and Saturn's magnetospheric plasma. In most planetary interactions, the two ionisation sources are solar radiation and the solar wind plasma, which both originate at the Sun and therefore arrive at the planet from approximately the same direction. At Titan, however, the two ionisation sources have different origins. While the direction of the solar radiation source remains constant, the location of the upstream side in Titan's ionosphere constantly changes and is a function of orbital position. This is also demonstrated in Figure 12 which shows the solar radiation wake (Titan's night side) in orange, and the magnetospheric wake, or magnetotail, in green. We can see that the angle between these two wakes is constantly changing with Titan's orbital motion. This angle is called *solar incidence-ram-angle* (SRA) and is zero at 18:00 hours SLT (Sittler et al., 2009).

When the solar wind pressure is high, Saturn's magnetopause can get pushed closer to the planet, sometimes past Titan's orbit. In this case Titan can be found in the magnetosheath where it is exposed to the shocked solar wind if it is in or near the noon sector of its orbit around Saturn. This was observed during the Cassini T32 Titan flyby (Bertucci et al., 2008 and Ma et al., 2009) and a *magnetic memory* was revealed; Titan's induced magnetosphere can be populated by magnetic *fossil fields*. These fields show the properties of a magnetic environment that Titan was embedded in up to three hours earlier.

Figure 15: Conditions under (A) nominal solar wind dynamic pressure such that Titan's orbit is located inside the magnetosphere and (B) at high solar wind dynamic pressure such that Titan is found in Saturn's magnetosheath near noon Saturn local time (SLT), exposed to the shocked solar wind (not to scale) (Bertucci et al., 2008).

When the solar wind dynamic pressure is very high, Saturn's magnetosphere could even get pushed so close to the planet that part of Titan's orbit would end up outside of Saturn's magnetosphere. In that case Titan would be exposed directly to the supersonic solar wind. This has not yet been observed, however a bow shock would likely form on the solar wind upstream side of Titan. The probability of finding Titan in the supersonic solar wind is low because the solar wind dynamic pressure is rarely high enough to push the bow shock inwards past Titan's orbit. In addition, Titan would have to be located in the noon sector when this happens. However, Wei et al. (2009) also found some evidence that the presence of Titan affects the location of Saturn's magnetopause. In the noon sector, the magnetopause is more frequently observed at or closer to the planet than Titan's orbit when the moon is absent. Titan's presence may therefore reduce the magnetosphere's compressibility.

As described in section 1.3.2, when an unmagnetised body with an atmosphere is exposed to an external plasma, an important feature of this interaction is the ionopause. Pressure balance can be used to calculate a simple estimate of the ionopause distance from Titan (c.f. section 1.3.1 for Saturn's magnetopause location). We consider the scenario of Titan being exposed to Saturn's magnetospheric plasma. The dominant pressures on Titan's ionosphere due to Saturn's magnetosphere are particle and magnetic pressure, while Titan's ionospheric pressure is dominantly particle pressure. Particle pressure consists of dynamic and thermal pressure:

$$p_p = p_{dy} + p_{th} = \rho u^2 + n k_B T$$

Equation 23

where p_p is the particle pressure, p_{dy} is the dynamic pressure, p_{th} is the thermal pressure, ρ is the mass density, u is the velocity, n is the number density, k_B is the Boltzmann constant and T is the temperature. Saturn's magnetospheric particle

pressure is dominated by dynamic pressure, whereas Titan's ionospheric particle pressure is mainly thermal. Pressure balance at the ionopause can therefore be estimated by equating Saturn's magnetospheric pressure (magnetic and dynamic particle pressure) and Titan's ionospheric pressure (thermal particle pressure):

$$\rho_{MS} u_{MS}^{\ 2} + \frac{B_{MS}^{\ 2}}{2\mu_0} = n_{IS} k_B T_{IS}$$

Equation 24

where the subscripts 'MS' and 'IS' indicate Saturn's magnetosphere and Titan's ionosphere, respectively.

Sittler et al. (2004) used pressure balance and Voyager 1 data to estimate an ionopause location between 1025km and 2225km altitude. However, the ionopause location and also its thickness can fluctuate widely and there are likely large day/night variations.

Titan's plasma environment has been reviewed by Arridge et al. (2011). Several studies have been carried out to study and classify different environments that Titan is exposed to: Rymer et al. (2009), Simon et al. (2010), Garnier et al. (2010), Nemeth et al. (2011) and Westlake et al. (2011). For example, Rymer et al. (2009) grouped the Cassini targeted Titan flybys into different categories according to electron populations measured by the CAPS-ELS (Cassini Plasma Spectrometer - Electron Spectrometer) and MIMI-LEMMS (Magnetospheric Imaging Instrument – Low Energy Magnetospheric Measurement System). The four main categories are *plasma sheet, lobe-like, magnetosheath* and *bimodal*. The bimodal category contains two distinct electron populations, of which the lower ones may be associated with water group products. Only two encounters so far have been observed partly in the magnetosheath, T32 and T42. 34 out of the 54 encounters analysed were classified as being in one of these four groups, whereas the

remaining flybys were reported as combinations of the regions. Arridge et al. (2011) combined and updated the above mentioned plasma environment studies.

Saturn's inner magnetosphere is dipolar, however, the larger the distance from Saturn, the less dipolar and stretched out and more disk-like the magnetic configuration becomes. Therefore at Titan, the magnetic field can be of the nominal North-South configuration, it can point radially towards or away from Saturn, or somewhere in between (Bertucci et al., 2009). This adds more complexity to the interaction flow (Arridge et al., 2011).

1.4. Titan's ionosphere

The partially ionised layer of a planet's or moon's atmosphere is called the ionosphere. It is created by photon and energetic particle irradiation (Bagenal, 2001). The dominant ionisation sources are photoionisation by extreme ultraviolet (EUV) solar photons and electron-impact ionisation by electrons that have sufficient energy to overcome the neutral atom or molecule's ionisation potential (Blanc et al., 2002). In this section we review some aspects of Titan's chemically rich ionosphere.

1.4.1. Ionisation sources

Titan's ionosphere is produced from Titan's atmosphere and exosphere by photoionisation, charge-exchange and electron impact ionisation from precipitating magnetospheric plasma, energetic particles, and galactic cosmic rays as demonstrated in Figure 16 (Sittler et al., 2009). In the figure, the SRA is zero therefore the solar radiation and magnetospheric plasma flow are both incident on

the left side which implies an orbital position on the dusk side of Saturn's magnetosphere (18:00 SLT).

The upstream magnetospheric plasma consists of H^+, H^{2+} and O^+ ions plus other water group (e.g. OH^+, H_2O^+, H_3O^+) and methane group (CH_n with $2 \leq n \leq 4$) ions. These mostly keV ions are not magnetised and can penetrate into the lower ionosphere (Sittler et al., 2009). Magnetospheric electrons can only move along magnetic field lines and therefore are mostly restricted to higher altitudes. However, it is possible for them to undergo gradient and curvature drifts (see section 1.1.2.1) which may allow entry into the deeper ionosphere (Hartle et al., 1982, Strobel et al., 1992). Magnetospheric electrons and photoelectrons from UV photoionisation in Titan's upper atmosphere create non-thermal electrons. These electrons can in turn contribute to the heating of thermal electrons (Wahlund et al., 2005).

Other ionisation sources include interplanetary dust (IP) particles and Saturn's E ring dust particles which can add metallic ions and water ice, respectively, down to altitudes around 600 km and above (Molina-Cuberos et al., 1999, English et al., 1996). In addition, galactic cosmic rays (GCR) can reach altitudes as low as 100 km (e.g. Borucki and Whitten, 2008, and references therein).

Figure 16: Ionisation sources in Titan's atmosphere (Sittler et al., 2009).

The main pick up ions are created from Titan's neutral exospheric species H, H_2, N, N_2, and CH_4. N atoms are produced from dissociation of N_2 due to magnetospheric keV ions, solar UV radiation and magnetospheric electrons and energetic particles. As discussed in the previous section, the ionised exospheric neutrals are picked up by the magnetospheric plasma. The resulting pick up ions are H^+, H_2^+, N^+, N_2^+ and CH_4^+ and the mass loading process can slow the flow down from around 120 km s^{-1}

several R_T upstream of Titan to approximately 5 km s^{-1} or less at the topside of the ionosphere (Sittler et al., 2009).

1.4.2. Structure

In Figure 17 we can see electron density profiles from Cassini and Voyager occultation data, from Cassini Titan flybys Ta and Tb using RPWS, and from an MHD model (Kliore et al., 2008). The Cassini prime mission provided eight occultation observations at dusk and dawn which are averaged in the figure. The data generally agree that the electron density maximum occurs at an altitude around 1200 km or slightly lower, which is mainly due to solar EUV radiation and resulting secondary ionisation by photoelectrons (Cravens et al., 2009). Chemical equilibrium conditions hold below about 1400 km (Ma et al., 2006, 2007) which is the approximate location of the exobase.

Figure 17: Electron density data from a number of sources: The curves marked as 'Dusk Avg' and 'Dawn Avg' are radio occultation data from the Cassini RSS (Radio Science Subsystem), Cassini flyby Ta and Tb inbound and outbound data from RPWS (Radio and Plasma Wave Science), and MHD model results (Kliore et al., 2008)

Figure 18 shows electron density and temperature profiles from 52 Cassini RPWS/LP Titan flyby data, including median values (Edberg et al., 2010). Again, the ionospheric peak can be observed around 1150 km. On an individual flybys basis, the main electron density peak occurs between 1000 and 1400 km altitude (Ågren et al., 2009). The electron population in Titan's ionosphere is cold compared to magnetospheric populations at above approximately one R_T and higher. These measured ionospheric electron temperatures mostly agree with pre Cassini model predictions (Gan et al., 1992, Roboz and Nagy, 1994). In addition, a more recent thermal model agrees well with Cassini Ta flyby data (Galand et al., 2006). Cravens et al. (2009), Sittler et al. (2009) and Kallio et al. (2011) also discuss a variety of

other pre and post Cassini models covering a range of different types and simulated conditions.

Figure 18: Electron density (a) and temperature (b) profiles from 52 Cassini Titan flybys using RPWS/LP (Langmuir Probe) data. The altitude range is in Titan radii. 1 R_T = 2575 km, hence the altitude range at which data is presented is approximately 950 km – 5150 km. The black lines represent median values (Edberg et al., 2010).

The electron densities at the peak of the respective flybys are shown in Figure 19 as a function of solar zenith angle (SZA). The day/night terminator on the surface is at a SZA of 90°, and solar radiation is highest at 0°. We further discuss SZA with respect to negative ions in chapter 5.5.5 and 5.6.4. The data clearly demonstrate a large difference between dayside and nightside densities; the peak nightside densities are about a factor of 3 or 4 less than the peak dayside densities (Ågren et al, 2009, Cravens et al., 2009). Therefore the dominant ionisation source appears to be solar EUV radiation, whereas magnetospheric electron impact ionisation is the main source left to produce some of the nightside densities.

Figure 19: Electron peak densities as a function of solar zenith angle (SZA) from RPWS/LP data of the Cassini Titan flybys as shown. From Ågren et al. (2009).

In section 3 we study observations of ionospheric photoelectrons found in the exosphere and Titan's tail. We explore why they are found at such large distances to their point of origin and discuss implications on Titan's magnetic environment. This work is published in Wellbrock et al. (2012). In section 4 we investigate the structure of Titan's ionosphere using electron observations in the outer parts of the ionosphere near the exobase where in some regions they seem to experience an increase in energy of up approximately 100 eV.

1.4.3. Composition and chemistry

Due to the presence of organic hydrocarbons, Titan's atmosphere and ionosphere are some of the most complex chemical systems known in terms of composition. The INMS (Ion and Neutral Mass Spectrometer) instrument onboard Cassini can measure ions and neutrals with masses up to 99 amu (Waite et al., 2007). Figure 20 shows composition data from INMS. The composition is clearly organised into groups separated by approximately 12-14 amu which is the mass of carbon and nitrogen. More specifically, most of these groups consist of species corresponding to $C_nH_m^+$ and $C_{n-1}H_mN^+$ where *n* and *m* are integers (Cravens et al., 2009). Low Cassini Titan flybys typically have a closest approach (CA) altitude of around 1000 km. The chemical complexity increases with decreasing altitude and higher mass species are more abundant at the lowest altitudes sampled. Compositions are mainly similar on the day and night sides, however according to a study by Robertson et al. (2009) comparing flyby data from T5 (nightside pass) and T18 (dayside pass), higher mass species are relatively more abundant on the dayside.

Figure 20: Cassini INMS composition data of ions and neutrals with masses <100 amu in Titan's upper atmosphere and ionosphere (from Waite et al., 2007).

A large number of species with masses higher than 99 amu have been observed with other instruments such as the CAPS-IBS (Cassini plasma analyser – ion beam spectrometer) and are yet to be identified due to lower energy resolution (e.g. Wahlund et al. (2009), Crary et al., 2009).

To give an idea of the complexity, we show an ionospheric chemical scheme in Figure 21. It was adapted from the model results of Keller et al. (1998) and includes some post Cassini improvements from models by Vuitton et al. (2006, 2007). The observed composition, dynamics and chemistry of Titan's thermosphere and ionosphere are reviewed in more detail by Cravens et al. (2009). A topic of high

interest is the discovery of heavy (up to 13,800 amu/q) mass negative ions (Coates et al., 2007b) using the CAPS-ELS (Cassini plasma analyser – electron spectrometer), which is the main science topic of the work presented here (chapter 5). Waite et al. (2009) review Titan's complex chemistry with emphasis on heavy ions and processes leading to the formation of aerosols in the part of the ionosphere sampled by Cassini (mainly > 950 km) which may fall to the lower atmosphere and surface forming Titan's famous haze layers.

Figure 21: Ionospheric chemical scheme showing some pathways leading to Titan's lower mass ions (Cravens et al., 2009).

2. Instrumentation

2.1. The Cassini-Huygens Mission

The Cassini-Huygens is an international flagship mission costing over $3 billion in consisting of an orbiter (Cassini) and a Titan lander (Huygens) (Matson et al., 2002, Russell, 2005). NASA's Jet Propulsion Laboratory built the Cassini orbiter, to which the Italian Space Agency (ASI) contributed with radio equipment including a high-gain antenna. Cassini was named after Italian-born French scientist Giovanni Cassini who made several important discoveries when studying the Saturnian system in the second half of the 17th century including the discovery of a number of its moons. The Huygens lander was built by the European Space Agency (ESA) and named after Dutch astronomer Christiaan Huygens who discovered Titan in 1655.

The six tonne spacecraft was launched on 15 October 1997 on a Titan IV rocket. Some gravity assist manoeuvres were required on its seven-year journey to the Saturn system (Figure 22), during which observations of Venus, the magnetospheres of Earth and Jupiter, and some aspects of the solar wind were made. Saturn orbit insertion (SOI) occurred on 1 July 2004 and Huygens landed on Titan on 14 January 2005. Cassini's initial four-year prime mission was completed in June 2008, after which the first extended tour began: The *Cassini Equinox Mission* which lasted two years until 2010 and was then extended again as the *Cassini Solstice Mission* until September 2017. The two extended missions are named so due to the Saturn equinox in August 2009 and the summer solstice in the northern hemisphere in 2017. The total of 13 years in orbit by 2017 is the longest continuous observation of a planetary system other than Earth by a single spacecraft and will allow the investigation of changes due to solar activity and seasonal changes (also see Figure 7). The total number of Titan flybys by 2017 will be 127: 45, 28 and 54 flybys during the prime, Equinox and Solstice missions, respectively.

Figure 22: Cassini-Huygens mission trajectory from Earth to Saturn using several gravity-assist manoeuvres (from NASA).

The primary mission objectives include detailed investigation of Saturn's magnetospheric system, the planet, its atmosphere and weather, the interaction of its numerous moons and rings, and a study of Titan, from its interior, surface properties to the structure, evolution and formation of its atmosphere and ionosphere, and plasma environment interactions.

Cassini-Huygens is one of the largest, heaviest and most complex interplanetary spacecraft ever built. It is 6.7 m high and 4 m wide and comprises 12 instruments onboard Cassini (Figure 23), and six onboard Huygens.

Figure 23: The Cassini-Huygens spacecraft (Burton et al., 2001).

2.2. The Cassini Plasma Spectrometer (CAPS)

The CAPS instrument (Young et al., 2004) consists of three individual sensors: one Electron Spectrometer (ELS) and two ion sensors, the Ion Beam Spectrometer (IBS) and Ion Mass Spectrometer (IMS). The CAPS electron spectrometer is the main sensor used for the studies presented here. The location of the CAPS instrument onboard the Cassini orbiter can be seen in Figure 23. It is placed on a pallet called the *Fields and Particle Pallet* which is shown in Figure 24. In order to increase the field of view, CAPS is placed on a motorised actuator which can move at 1° per second and can sweep through a maximum range of ±104°. The actuation is about

the spacecraft's z-axis (see Figure 23, Figure 24 and Figure 25), which is the longest axis of the spacecraft and is negative towards the high-gain antenna. At a nominal actuator angle of 0° the instruments point towards the negative y-axis. A large part of the sky can be covered using the actuator motion, however, some parts of the instrument FOV (field of view) are obscured by objects of the spacecraft body (e.g. Lewis et al., 2008, Young et al., 2004). The FOV is shown in Figure 26. During most of the Titan flybys analysed here the actuator scan angle was ~85 ° ±12 ° for the region near closest approach, while a few flybys were performed with no actuation and the FOV fixed in the direction of travel.

Figure 24: The Fields and Particle Pallet onboard the Cassini orbiter. The location and orientation of CAPS is indicated. The azimuth is in the spacecraft x-y plane and elevation parallel to the z-axis. The CAPS instruments point towards -y in the configuration shown (Young et al., 2004).

Figure 25: A sketch of the Cassini orbiter showing the location and orientation of the three CAPS instrument fans, which are exaggerated in size for clarity (shaded regions). The actuator is in its nominal position here, hence the instruments fields of view all contain the -y direction (Rymer et al., 2001).

Figure 26: Projection of the CAPS-IMS field of view, which is similar for ELS and IMS. The shaded areas represent obscuring features. These include the High Gain Antenna (HGA), the structure of the fields and particles palette (FPP), part of the MIMI-LEMMS instrument, the Radio Thermo Isotope Generator (RTG), the Huygens probe mount and orbiter thrusters (Young et al., 2004).

2.2.1. Cassini Plasma Spectrometer – Electron Spectrometer (CAPS-ELS)

The CAPS-ELS is a hemispherical top-hat electrostatic analyser (ESA) which measures the flux of electrons as a function of energy per charge and direction of

arrival. This section is based on Young et al. (2004), Linder et al. (1998), Coates et al. (1992) and Johnstone et al. (1997). The design is based on an improved version of the High Energy Electron Analyser (HEEA) of the Cluster PEACE (Plasma Electron and Current Experiment) (Johnstone et al., 1997).

2.2.1.1. Operation principle

Incident particles enter the instrument through a baffled opening and then pass between two concentric hemispherical electrostatic analyser plates. The outer plate is grounded whereas the inner plate is at a positive voltage. The resulting potential difference is used to analyse negatively charged particles: Only particles with specific energies (depending on the potential difference) can pass all the way through the narrow slit between the plates; negatively charged particles with different energies would impact the surfaces. The voltage on the inner plate is variable, therefore the energies of the particles that are allowed to pass through can be changed. A special black coating on most internal instrument surfaces and the baffled opening reduce particle scattering and solar UV radiation.

The path of the selected particles then leads through two microchannel plates (MCPs) which consist of closely packed glass microchannels with a diameter of 12.5 microns. A voltage is applied across the plates and they are arranged on top of each other in a slanted chevron pair stack such that the particles impact on a channel wall of one of the plates rather than simply passing through them. The chevron arrangement also reduces ion feedback. When an electron strikes one of the channel walls made from resistive material, a cascade of secondary electrons is caused as the secondary electron emission coefficient of the wall coating material is >1; each channel is an independent electron multiplier. Depending on the position of the initial electron impact, the cascades of electrons are now detected by one of eight anodes which make up the fan structure of the instrument. Each anode covers an angular acceptance of 20° by 5° resulting in a total instantaneous angular

coverage of 160° by 5°. The direction of the incident particles can be established by which anode registers the count.

Figure 27: Cross-section of the CAPS instrument in the spacecraft x-y plane, demonstrating the relative positions of the three detectors ELS, IMS and IBS. The ELS electrostatic analyser (ESA) plates are at the top of CAPS-ELS.

2.2.1.2. Operation

During operation the voltage is swept through 64 steps covering a logarithmic energy range of 0.58 eV to 26,000 eV. The 64th step is the voltage flyback step to prepare for the next sweep, hence there are 63 energy bins which are shown in Table 1. This energy separation is matched to the analyser pass-band of $\Delta E/E$ = 16.7%. Each voltage is held for 31.25 ms. 25% of this accumulation time is *dead time* which allows the voltage to settle. A complete energy sweep takes two seconds.

Bin	Energy (eV)	Bin	Energy (eV)	Bin	Energy (eV)	Bin	Energy (eV)
1	26,040	17	2112	33	171.7	49	13.98
2	22,227	18	1805	34	146.9	50	11.64
3	18,991	19	1544	35	125.1	51	9.89
4	16,256	20	1319	36	107.4	52	8.72
5	13,876	21	1128	37	91.76	53	7.56
6	11,867	22	964.1	38	78.18	54	6.39
7	10,143	23	824.0	39	67.15	55	5.23
8	8674	24	704.3	40	57.45	56	4.64
9	7415	25	601.8	41	49.00	57	4.06
10	6336	26	514.8	42	41.81	58	3.48
11	5416	27	439.4	43	35.84	59	2.90
12	4630	28	375.9	44	30.49	60	2.32
13	3956	29	321.5	45	26.34	61	1.74
14	3383	30	274.8	46	22.21	62	1.16
15	2890	31	235.0	47	19.26	63	0.58
16	2471	32	200.9	48	16.33		

Table 1: CAPS-ELS energy bins (Lewis et al., 2010).

2.2.1.3. Microchannel plate gain

The number of electrons in a cascade resulting from one electron incident on a microchannel wall is called the *gain*. This number depends on the MCP interior surface coating, the spatial arrangement of the two MCPs with respect to each other, and the applied voltage. The ELS MCP gain is approximately 2×10^6 electrons. The interior coating degrades over time, therefore the instrument gain slowly decreases and has a limited lifetime. The MCP voltage is increased periodically to counteract this gain loss. In addition, a gold-plated copper spacer is present in the gap between the two plates which reduces the voltage necessary for a specific gain, hence extending the lifetime. The spacer also improves gain uniformity over the detector. There is a 500 μm gap between the MCP and the anodes with a differential voltage of 100 V. The anodes register one count for a minimum of every 400,000 electrons. These detected raw electron counts are read out by the instrument electronics and passed to the DPU (Data Processing Unit) for processing and transmission.

2.2.1.4. Geometric factor

The geometric factor of the instrument (e.g. Johnstone et al., 1997, Wurz et al., 2007) is required to transform the detected raw counts into scientifically meaningful, calibrated electron quantities. It depends on the geometry (effective area and solid angle acceptance) of the instrument. Lewis et al. (2010) state that one can think of the geometric factor as "the relationship between the number of electrons entering the instrument, and the number being measured by the instrument". The geometric factor is also a function of the intrinsic efficiencies of the instrument, and energy. The determination of the geometric factor started with simulations and then ground calibration tests and continued en route to Saturn and in the Saturn system, including cross calibration with other instruments (Linder et al., 1998, Lewis et al., 2010).

The count rate *C* of an electrostatic analyser in units of s^{-1} at an energy E is proportional to particle energy flux via a relationship involving the geometric factor. Further parameters may be derived such as differential number flux and phase space density *f* which are proportional to C/E and C/E^2, respectively. In addition, moments of the particle distribution function such as density and temperature can be determined from integrations of *f* (e.g. Lewis et al., 2008).

2.2.1.5. Spacecraft potential

The spacecraft can become positively or negatively charged in a plasma environment depending on the ambient plasma and solar radiation environment. In sunlight, the incident UV photons can strike the spacecraft surface and collide with atoms in the surface, freeing electrons. The energy of these photoelectrons depends on the work function of the surface. Cassini has multi-layered insulation surfaces which can result in photoelectrons with energies of tens of eV. Ambient higher energy electrons can also produce low energy secondary electrons when impacting the spacecraft surface. These processes leave the spacecraft positively charged, while the newly created electrons are attracted to and surround the spacecraft. As a result, a negatively charged cloud forms around the spacecraft within a sheath whose width is of order of the Debye length. This charge separation sets up a potential difference, with the spacecraft having a positive potential.

Photoelectrons that have an energy greater than this potential can escape it and will not be detected by ELS. Photoelectrons with lower energies can enter the instrument and give an important indication of the spacecraft potential value because their energy is equivalent to or less than the spacecraft potential. Electrons from the ambient plasma population which are not a result of the spacecraft charging are referred to as real. When these electrons enter the instrument, they would have been accelerated through the potential difference and the measured energy will be higher than their original value by an amount equal to the energy

equivalent to the potential difference. Therefore no real electrons will be detected at energies below the potential. These facts can be used to determine the spacecraft potential when it is positive; there is usually a small dip in the electron spectra which indicates the spacecraft potential. The population at lower energies of the dip is the spacecraft photoelectrons, and the population at higher energies is real. An example of the different populations is shown in Figure 28. The spacecraft potential is positive until about 11:00 UTC. The black line indicates the spacecraft potential. The electrons below this line are spacecraft photoelectrons.

Figure 28: Electron spectrogram of 24 hours in Saturn's magnetosphere. The horizontal axis indicates the UTC time and the distance from Saturn in R_S. The figure shows an example of regions where the spacecraft is at a positive potential (until approximately 11:00 UTC) and at a negative potential in Saturn's inner magnetosphere. The electron population below the black line is the spacecraft photoelectron population (Lewis et al., 2010).

In some regions, the spacecraft potential can become negatively charged. This is common in very dense plasma regions, such as Saturn's inner magnetosphere and Titan's ionosphere, and when the spacecraft is not exposed to solar radiation. In these high flux cases electrons become attached to the spacecraft at a rate faster than the photoelectron production rate. As a result of this negative potential, ambient real electrons are now being decelerated before being detected, and as a result the detected energy is lower than the original, real value. In addition, low energy electrons that do not have enough energy to overcome the potential are repelled and this real population is hence missing from the data. The value of the negative potential cannot generally be determined from ELS alone and often spacecraft potential data from other instruments such as the RPWS Langmuir Probe (LP) need to be used. However, the spacecraft potential may not always be exactly the same on different parts of the spacecraft, and CAPS-ELS is at some distance from the RPWS LP as can be seen in Figure 23. The spacecraft potential is either zero or negative in Figure 28 after about 11:00 UTC evident in the absence of detected spacecraft photoelectrons, which is due to the dense plasma in Saturn's

inner magnetosphere. The lowest electron population may be missing in the spectrogram if the potential is negative.

In cases where the spacecraft potential is non-zero the flux must be corrected by moving the spectra of *f* by the accelerating or decelerating potential as appropriate. According to Liouville's theorem (e.g. Baumjohann and Treumann, 1997), this correction must be done in phase space density because phase space density is conserved during a shift in particle energy.

2.2.2. CAPS Ion Beam Spectrometer (CAPS-IBS)

The CAPS-IBS is capable of providing high resolution, 3-D measurements of the energy and angular distribution of beamed ion populations. It is based on an earlier design by Bame et al. (1978). The principle of operation is similar to ELS (also see Figure 27) but the IBS electrostatic analyser has a larger radius and narrow plate spacing providing higher energy resolution. Other differences include a cross-fan technique allowing the 3-D measurements over a small angular range (e.g. the solar wind or other narrow ion beams such as ions in Titan's ionosphere). The energy range is 0.95 eV to 49,800 eV with a 255-step voltage scan and energy resolution of $\Delta E/E = 0.015$.

2.2.3. CAPS Ion Mass Spectrometer (CAPS-IMS)

The CAPS-IMS consists of a toroidal ESA which is designed to measure positively charged ions as a function of energy per charge and angle of arrival. In addition, IMS is also equipped with a carbon-foil based time of flight (TOF) mass spectrometer using a linear electric field (LEF) timing region (also see Figure 27), therefore compositional information is also provided.

2.3. Cassini Fluxgate Magnetometer (MAG)

The magnetometer (Dougherty et al., 2004) onboard Cassini measures the ambient magnetic field and consists of a fluxgate magnetometer (FGM) and a scalar/vector helium magnetometer (S/VHM). Both parts are on an 11 m boom such that the measurements are not notably affected by the spacecraft's magnetic field. The FGM and S/VHM are located half way along the boom and at the end, respectively. The S/VHM ceased to function in November 2005 and is therefore not discussed here. FGM provides measurements of three perpendicular magnetic field components. FGM data are used to determine electron pitch angles in this work, and are provided courtesy of Imperial College London.

2.4. Cassini Ion and Neutral Mass Spectrometer (INMS)

The INMS instrument was designed to determine the mass composition and number densities of neutral species and low-energy ions primarily in Titan's upper atmosphere but also in Saturn's ring regions and icy moons (Waite et al., 2004). INMS is also located on the Fields and Particles Pallet shown in Figure 24. It has three different operation modes. The closed-source neutral mode is effective for non-reactive neutrals such as N_2 and CH_4. The open-source neutral mode is for reactive neutrals such as atomic nitrogen. In these neutral modes, ions and electrons are removed by an ion trap. In order for the neutrals to be analysed, hot-filament electron guns are used to ionise them.

The third mode, open-source ion mode, is used for ions with energies less than 100 eV. As ions enter the instrument, they are deflected electrostatically using switching lenses and passed through a radiofrequency quadropole mass analyser. Ions are selected according to specific mass to charge ratios and then counted and multiplied. The accumulation time is 31 seconds and voltages are adjusted to cover a mass range of 1 to 99 amu. The scans are repeated every 10 seconds during Titan encounters (Crary et al, 2009). For ions to enter the instrument, the instrument must be pointed within 2° of the direction in which the spacecraft is travelling.

The work by Crary et al. (2009) is used in this thesis; they compare CAPS-IBS and INMS data to estimate spacecraft potential and other parameters. The results of the work are used in this study to estimate spacecraft potential uncertainties and are provided by the Southwest Research Institute.

2.5. Cassini RPWS Langmuir Probe (LP)

The Langmuir Probe onboard Cassini is part of the RPWS instrument (Gurnett et al., 2004). It consists of a spherical metallic sensor with a diameter of 5 cm mounted on a boom which places it 1.5 m from the spacecraft main body. An applied voltage causes the electrons in the ambient plasma to create a current. Measurement of this current and its relation to the applied voltage can be used with some assumptions to determine plasma characteristics such as density, temperature, ion velocity, mean ions mass, and also spacecraft potential. During Titan flybys with CA (closest approach) lower than 1200 km, the voltage is swept between -4 and +4 V in 512 steps within 24 seconds (Ågren et al., 2009). The location of the LP onboard the Cassini orbiter can be found in Figure 23. LP spacecraft potential data are used in this study and are provided by the Swedish Institute of Space Physics.

3. Cassini observations of ionospheric photoelectrons at large distances from Titan: Implications for Titan's ionospheric environment and magnetic tail

3.1. Introduction

This chapter was published in Wellbrock et al. (2012).

In planetary atmospheres, photoelectrons can be produced by the ionisation of molecules due to solar radiation from either the solar continuum or discrete solar lines (e.g., Frahm et al., 2006). One intense solar line is the He II Lyman α line at 30.4nm. Radiation from this line ionises molecules and as a result liberates photoelectrons in several planetary atmospheres, for instance from the ionisation of N_2 and O_2 at Earth (e.g. Coates et al., 1985), CO_2 at Mars (Frahm et al., 2006; Frahm et al., 2006b; Mantas and Hanson, 1979) and atomic oxygen and CO_2 at Venus (Coates et al., 2008), see also Coates et al. (2011).

At Titan, these solar He II line photons can ionize N_2 to produce N_2^+ in the $A^2\Pi_u$ state, generating photoelectrons with energies of 24.1 eV (Galand et al., 2006; Coates et al., 2007a, 2011). These can be seen in the sunlit ionosphere as a discrete peak in the electron energy spectrum from the CAPS-ELS. The main cold electron population of the ionosphere is a broader, lower energy signature in the spectrum (e.g. Coates et al., 2007a, Gan et al., 1992a, Galand et al., 2006).

Some observations of these photoelectron peaks near 24.1 eV can be found at large distances from Titan. Coates et al. (2007a) investigated CAPS observations during the T9 flyby, a distant tail pass (closest approach (CA) altitude of 10408 km). A split tail signature was observed, consisting of two intervals that included cold electron populations. Photoelectron peaks at 24.1 eV (accounting for spacecraft potential) were clearly visible in some spectra of the first interval and possibly in the second. CAPS ion observations show that the observed ion species in the two intervals differ (Szego et al., 2007). The first interval consisted of dense, slow, cold ions in the 16-19 amu and 28-40 amu mass range whereas the ion population found in interval 2

was less dense, faster and in the 1-2 amu range. Local production of photoelectrons created by He II line photons at large distances from Titan is unlikely because neutral N_2 densities are too low there. Coates et al. (2007a) concluded that the cold electrons and ions were escaping plasma from Titan's ionosphere, and that the two intervals were magnetically connected to different parts of the ionosphere. Wei et al. (2007) also discussed plasma escape during the T9 flyby and concluded that cold ionospheric populations moved along magnetic field lines from the low upstream ionosphere to the distant tail. This type of escape can be caused by a pressure gradient between the high density plasma in the ionosphere and the lower density plasma in the tail. Coates et al. (2007a) suggested that suprathermal electrons including 24.1 eV photoelectrons travelling along magnetic field lines can set up ambipolar electric fields (Keller and Cravens, 1994) because they are more mobile along magnetic field lines than ions, causing charge separation, similar to the polar wind on Earth (Ganguli, 1996). Such fields may enhance pressure-driven plasma escape. This is also discussed in Coates et al. (2011) and compared to Mars and Venus. Similar escape processes occur at Venus such as polarization electric fields, described by Hartle and Grebowsky (1995). We continue the work of Coates et al. (2007a) by investigating three case studies of photoelectron peak observations that may be connected to Titan's lower altitude ionosphere, which are described in section 3.2. In section 3.3 we investigate the idea that the photoelectrons were produced in the deeper ionosphere on the dayside and travelled along magnetic field lines to the large distance observation sites. We find support for this idea with modelling results from a hybrid model (Sillanpää, 2008, Sillanpää et al., 2011). We also discuss how this may relate to atmospheric escape and the tail structure.

3.2. Observations

3.2.1. Case study 1: T40

Cassini's Titan 40 flyby (T40) took place on 5 January 2008 with the CA at an altitude of 1014 km at 21:30 UT. The flyby geometry is shown in Figure 29 in Titan-centred coordinates. Saturn Local Time (SLT) was 11:20 therefore the angle between Titan's nominal corotation wake and the solar wake (i.e. Titan's nightside) is nearly 90°. The magnetospheric corotation wake, which is expected if Saturn's magnetospheric plasma was incident from the nominal direction i.e. from the positive y direction at x=0 in Figure 29 (also see chapter 1.3.3 and Figure 12), is referred to as the *nominal* corotation wake. As we will see shortly, the actual (observed) direction of the corotation wake can vary. The spacecraft entered the southern part of Titan's nominal corotation wake at 21:13 UT and then continued its path through Titan's dayside ionosphere. The spacecraft came in from the south and covered a range of increasing latitudes, as shown in Figure 29, with CA taking place at -12.2°.

Figure 29: T40 flyby geometry in Titan-centred coordinates. Saturn's nominal magnetospheric plasma comes from the positive y-axis and impinges on Titan's (black circle) atmosphere, causing a nominal corotation wake (green) along the negative y-axis. Arrows show directions towards the Sun and Saturn as indicated; the solar wake is Titan's nightside and is in the direction opposite to that indicated by the red arrow ('towards sun'). The black dashed line describes Cassini's flyby trajectory 45 minutes before (black diamond shape) and after closest approach. The 24.1 eV photoelectron peaks were observed at A, B and in the dayside ionosphere between C and F. The points are at A: 20:57:38 UT, B: 21:07:38 UT, C: 21:22:38 UT, D: 21:26:48 UT, E: 21:35:00 UT and F: 21:46:30 UT

Figure 30 shows a CAPS-ELS energy-time spectrogram in DEF (differential energy flux) during T40 from 20:45 UT to 22:00 UT. The times labelled “A” (20:57:38 UT), “B” (21:07:38 UT), “C” (21:22:38 UT), “D” (21:26:48 UT), “E” (21:35:00 UT) and “F” (21:46:30 UT) correspond to the same labels in Figure 29. The region between 21:22 UT (point “C”) and 21:46 UT can be identified as ionospheric plasma because it contains typical cold, dense electrons. Outside this region there is a population of very low energy (<4 eV) electrons which are spacecraft photoelectrons. These disappear when the spacecraft passes through Titan's dense ionosphere, because the ambient flux of negatively charged particles dominates the current balance to the spacecraft (see section 2.2.1.5). This results in a negative spacecraft potential and is also seen intermittently before 21:22 UT around points A and B, and just before C. Outside the ionosphere, Saturn’s magnetospheric population is highly variable but there are “bi-modal” distributions with peaks at 10s and 100s of eV (also see section 1.3.3). This encounter was classified as such by Rymer et al. (2009).

Figure 30: T40 electron spectrogram. Points A, B, C, D, E and F correspond to the same points in Figure 29. Closest approach (CA) was at 21:30 UT. Spacecraft photoelectrons can be seen at low energies before A and after F, and also for short periods between A and B, and between B and C. 24.1 eV photoelectron peaks can be observed at and near A and B, and in the ionosphere (between points C and F).

The spectrogram in Figure 30 also shows that in the ionospheric region a partial *bite out* of hotter (>50 eV) magnetospheric electrons can be observed: There are almost no magnetospheric electrons between the dashed lines at C and E. This bite out is a result of the hot magnetospheric electrons being absorbed and scattered down as they interact and collide with particles of Titan's dense upper atmosphere (Hartle et al., 2006, Hartle et al., 1982, Gan et al., 1992b), leaving behind photoelectrons and secondary electrons at lower energies. Most of the magnetospheric electrons detected between the dashed lines at E and F are relatively hot with energies >600 eV. We refer to such a region as a *partial magnetospheric bite out*. There is one

short period of time in the ionospheric region around 21:37 UT where colder magnetospheric electrons are present in addition to the hotter ones.

The vertical spikes around CA appear when the actuator points in the direction in which the spacecraft travels (the *ram direction*). They have been identified as negative ions (Coates et al., 2007b, Waite et al., 2007, Coates et al., 2009) and are discussed in more detail in chapter 5.

Cold (near 10 eV or below), dense plasma "blobs" are present at A, B and just before C, on Titan's downstream corotation side. Points A and B are at an altitude of 9811 km (3.8 R_T) and 6424 km (2.5 R_T) from Titan's surface, respectively. These distances are too far from Titan to be part of the actual ionosphere. Therefore, these cold, dense blobs are likely to be plasma in or near the tail that travelled downstream from Titan's ionosphere. The blob just before C is closer to Titan and well in the nominal tail, blob B is in the southward and Saturn-ward part of the nominal tail, and blob A is just outside the nominal tail, further southward and closer to Saturn. Hence both the distance and the angle to the nominal tail increased from B to A. However, the actual tail could be at an angle to the nominal tail orientation and therefore the structures observed at points A and B may both be part of the actual tail. The tail structure is further discussed in section 3.3.

Plots of individual electron spectra at A, B, C and D are shown in Figure 31. These are each averaged over three individual two-second raw spectra to improve the signal to noise ratio. The broad peaks on all four plots at the low energy end are the ionospheric electrons as described above (the wake plasma blobs at A and B, and the bulk ionospheric electrons at C and D). The extent of the magnetospheric bite out can be seen in the higher energies. Of particular interest in these spectra is the small peak at a measured energy of 22.2 ± 1.9 eV in all four plots. The uncertainty corresponds to the ELS energy resolution of 16.7%. This energy therefore matches that of the photoelectron peak at 24.1 eV corresponding to the energy of electrons

that are emitted as a result of the solar He II line radiation ionising nitrogen as described in section 1 (e.g. Galand et al., 2006, 2010), within the measured uncertainty. At the times when the peaks are detected, the spacecraft potential is zero or negative. This is evident in the absence of spacecraft photoelectrons in the spectrogram (Figure 30). A negative spacecraft potential means that the measured energy is lower than the actual energy. Wahlund et al. (2009) found that the spacecraft potential during close Titan flybys is relatively constant: -0.7 V to -1.6 V. Crary et al. (2009) state a spacecraft potential range from -0.5 V to -2.0 V for most close Titan flybys. Cassini RPWS measurements indicate that the spacecraft potential at points B, C and D were -0.62 V, -1.7 V and -0.68 V respectively (pers. comm. with RPWS team). The data was not available at A. When the spacecraft potential is negative , an energy of the same amount (in eV) needs to be added to the measured energy as the incoming electrons are retarded in travelling through this potential drop. The corresponding energy in this case would still match the photoelectron peak at 24.1 eV. The region between 20:50 UT and 21:22 UT seems to contain some ionospheric plasma between points A, B and C, with strong enhancements at and around these points. However, photoelectron peaks are only observed at and in close vicinity to A and B, and in the ionosphere (e.g. at points C and D).

Figure 31: Energy spectra at points A, B, C and D in differential energy flux (DEF). Spectra are averaged over 3 energy sweeps (6 seconds). The arrow in each spectrum points at the 24.1eV photoelectron peak. Error bars assume Poissonian statistics on counts/acc data. The dashed line shows level registered by one electron in each energy bin.

Figure 32 shows a pitch angle plot averaged over all anodes and 3 energy sweeps (i.e. 6 seconds) starting at 20:57:38 UT (point A). The plots cover an energy range of 3.75 eV to 45.10 eV. The energy bins increase from the centre radially out. The pitch angle range shown is 0 to 180° however only part of this range is covered in both plots as shown (white indicates directions that CAPS did not cover). The colour scale indicates the intensity in DEF (Differential Energy Flux). We investigated

several pitch angle distributions and find that near points A and B the photoelectron peaks are mainly detected at lower (<55°) pitch angles. Occasionally some peaks can also be seen at higher angles but the intensity of these peaks is generally lower than those at lower angles. Pitch angles greater than ~100° were not covered at these times of the flyby. In the ionosphere proper the photoelectron peak intensity does not seem to depend on the pitch angle distribution. These observations are consistent with ionospheric photoelectrons escaping along magnetic field lines. Some pitch angle observations at and around A, B and C also show a slightly higher DEF (differential energy flux) at low pitch angles in the cold population (10 eV and below). This suggests that some of the cold electrons are lower energy photoelectrons that also escaped from Titan's sunlit ionosphere along magnetic field lines to the observations sites.

Figure 32: Pitch angle distributions. Data is averaged over all anodes and 3 energy sweeps (6 seconds). Panel (a) is at point A (20:57:36 UT) during T40. The photoelectron peak can be observed in the 24 eV bin at lower (<55°) pitch angles. Panel (b) is at the beginning of interval A during T17, at 19:38:57 UT. The photoelectron peak can be observed in the 24 eV bin at pitch angles >105°.

3.2.2. Case study 2: T17

The T17 flyby geometry is shown in Figure 33. Closest approach occurred on 7 September 2006 at 20:17 UT when Cassini was at 02:16 Saturn Local Time, at an altitude of 999 km. Cassini approached Titan from a direction close to the negative x-axis as shown in the diagram. It passed through the nominal wake and then the dayside ionosphere. The solar and nominal corotation wakes were at an angle of approximately 135° to each other. In the Rymer et al. (2009) magnetospheric environment classification, T17 is in the "unclassified" category, with brief occurrences of the bi-modal category.

Figure 33: T17 flyby geometry. Arrows show the directions towards the Sun and Saturn as indicated. The inbound leg (starting from the black diamond shape) is on the negative x-axis. The spacecraft flies through the nominal corotation wake (green) and then the sunlit ionosphere. The inbound leg is above the equatorial plane which is crossed just after CA (triangle). The trajectory is close to the equatorial plane throughout the encounter.

Figure 34 shows an electron spectrogram of T17 from 19:00 UT to 21:00 UT. The cold plasma marked as interval B between ~20:12 UT to 20:30 UT can be identified as Titan's ionospheric region proper. Negative ion spikes are again seen around closest approach as in the T40 case. The average DEF of the cold population during interval A on the spacecraft's inbound leg from 19:33 UT (~45 minutes before CA, at an altitude of ~12 000km (4.7 R_T)) is only slightly lower than that of the ionosphere proper but generally comparable. Hence this population appears to be plasma that moved downstream from the ionosphere and is part of the tail. The spacecraft's trajectory from the beginning of interval A to the point where it intersects the nominal tail is at an angle of approximately 80° to the nominal tail indicating a highly asymmetric tail in this case. The spacecraft potential is zero or negative during intervals A and B. This is evident in the disappearance of spacecraft photoelectrons at these times which can be seen in Figure 34. There is a partial bite out of magnetospheric electrons during intervals A and B, which becomes more prominent closer to Titan from about 20:00 UT where more electrons with energies >60 eV disappear.

Figure 34: T17 electron spectrogram. Closest approach occurred at 20:17 UT. Spacecraft photoelectrons are present before 19:35 UT and after 20:34 UT. 24.1 eV photoelectron peaks can be seen in the marked area. Interval B can be identified as the ionospheric region proper. Interval A seems to be plasma that moved downstream from the ionosphere and forms part of the tail.

The photoelectron peak in the electron energy spectra (not shown but similar to those in Figure 31) is present for most of intervals A and B (indicated in Figure 34), and is also visible in the spectrogram (indicated by white ellipse). The measured energy is again in the 22.2 eV energy bin. Cassini RPWS measurements show that

the lowest spacecraft potential in intervals A and B is -2.7 V (pers. comm. with RPWS team). Taking this negative spacecraft potential and the measured uncertainty into account it matches the 24.1 eV peak (as discussed above in the T40 case).

Pitch angle coverage during the first half of interval A is mostly >75° and then varies covering up to angles >55°. An example is shown in Figure 32 at 19:38:57 UT. Pitch angles in the first half of interval A show photoelectron peaks mainly at angles >105° with higher differential energy flux (DEF) closer to 180°. Peaks are also generally present and/or stronger at smaller angles in the covered range of 55° to 90°. Peaks closer to 90° can be seen occasionally but these are mostly lower in DEF than the peaks closer to 180°. The closer the spacecraft gets to Titan the weaker the dependence on pitch angle becomes. This observation supports the idea that the observed photoelectrons travel mostly along field lines. Coverage does not allow us to check if the photoelectron peaks are enhanced at very low angles close to 0° but the occurrence of most peaks closer to 180° indicates that the observed photoelectrons travel towards Titan. Similarly, most pitch angle observations in interval A indicate that the DEF of the cold electron population (10 eV or below) is slightly higher at pitch angles closer to 180°. It is therefore likely that some of these electrons, as in the T40 case above, are lower energy photoelectrons that are also travelling along field lines.

3.2.3. Case study 3: T15

Figure 35 shows the T15 flyby geometry. The inbound leg of the trajectory is on the positive x-axis. The spacecraft passes through the nominal wake and through the shadow of Titan's solid body where no solar radiation can ionize the atmosphere. Closest approach was at an altitude of 1906 km, on 2 July 2006 at 09:20 UT and at 21:20 SLT. The flyby was in the equatorial plane.

Figure 35: T15 flyby geometry. Arrows show directions towards the Sun and Saturn as indicated. The spacecraft's inbound leg is on the positive x-axis, from the black diamond shape. The trajectory is equatorial and covers a path through the nominal wake and then through the ionosphere, part of which is occulted by Titan's solid body. The purple circle marks the part of the trajectory where photoelectron peaks were detected.

A spectrogram of this flyby is shown in Figure 36. Cold ionospheric plasma can be seen from 08:57 UT to 09:49 UT and in this region the spacecraft potential is again zero or negative. A prolonged bite out is not observed during this encounter, most likely because the CA altitude is too high to observe a significant bite out. Some time variations are visible however, and the density of the magnetospheric (~ 100-1000 eV electrons) population is lower where cold ionospheric plasma is present. This encounter was classified by Rymer et al. (2009) as a plasma sheet encounter (relatively high energy and density environment) with brief occurrences of bimodal populations.

Figure 36: T15 electron spectrogram. Closest approach (CA) occurred at 09:20 UT. Spacecraft photoelectrons can be seen at low energies before 08:57 UT and after 09:48 UT. Cold ionospheric plasma can be observed from 08:57 UT until 09:48 UT, with 24.1 eV photoelectron peaks present as indicated. Part of the spacecraft's trajectory is in Titan's occulted ionosphere, from 09:20 to 09:33 UT.

The region between 09:20 UT and 09:33 UT is occulted from solar radiation by Titan's solid body. The only ionisation source in this interval is Saturn's magnetospheric plasma. The effect of this can be seen clearly in Figure 36. The measured DEF of the cold plasma population in this interval is much lower compared with the population at and around 09:05 UT where solar radiation is present.

Photoelectron peaks in the 22.2 eV energy bin are present during the interval marked with a purple circle in Figure 36 at a maximum altitude of 5760 km (2.2 R_T). RPWS measurements indicate a minimum spacecraft potential of -3.8 V in the

interval from 09:00:11 UT to 09:15:51 UT (pers. comm. with RPWS team). This again matches the 24.1 eV peak (as discussed above in the T40 case). The peaks are also clearly visible in the energy spectra (not shown). The same time period of the spacecraft trajectory is marked in Figure 35, also with a purple circle.

3.3. Discussion and modelling results for T15

In this section we discuss the results of the case studies presented in section 3.2. We also describe hybrid modelling results of T15 to support the theory. We then further discuss Titan's tail structure.

The observation of photoelectrons at large distances presents the question of where these photoelectrons came from. It is highly unlikely that they were created locally. This is because these photoelectrons are produced when neutral N_2 molecules are ionized. However, N_2 densities at such high altitudes are low (e.g. (Garnier et al., 2007)). When neutrals travel away from Titan's atmosphere it is likely that they get ionized by incoming magnetospheric plasma or solar radiation before reaching such large distances from Titan. If these photoelectrons were not created locally we suggest that they were produced closer to Titan in the sunlit ionosphere, and that they travelled along magnetic field lines to the observation sites, as discussed by Gan et al. (1992a), Coates et al. (2007a), and Wei et al. (2007). A global quasi-neutral hybrid Titan model, developed by Sillanpää (2008) at the Finnish Meteorological Institute, was used to test this idea for T15. We compared the Cassini magnetometer data to the hybrid model results along the Cassini trajectory. The agreement is very good: the –Bx lobes coincide almost perfectly and the magnetic field magnitude is mostly within 10 per cent of each other. Sillanpää et al. (2011) completed a separate study on T15 using this model. A global solution was modelled and in this case magnetic field lines crossing the spacecraft's

trajectory were traced. The results are shown in Figure 37. The pink line represents the part of the spacecraft trajectory where photoelectron peaks were observed (purple circles in Figure 35 and Figure 36). The yellow lines are magnetic field lines that are connected to this part of the trajectory. Note that no other magnetic field lines are shown. When following these field lines from the pink line it can be seen that they connect to the ionosphere near the moon's south pole. This area was sunlit at the time of the flyby because the subsolar latitude was 16° south. Therefore these magnetic connections support the idea that the observed photoelectrons travelled to the observation sites via magnetic field lines from the deeper, sunlit ionosphere, which is in this case near the south pole. In addition, the model run indicates that there were no periods when Cassini's trajectory was magnetically linked to Titan's dayside ionosphere when no photoelectron peaks were detected, further supporting this idea. Assuming our interpretation is correct, it is therefore possible to use photoelectron observations as "tracers" of magnetic field lines and escape paths from the dayside ionosphere in order to study Titan's complex plasma environment in more detail.

Figure 37: T15 hybrid modeling results. The pink line is the part of the spacecraft trajectory where 24.1 eV photoelectron peaks were observed. The yellow lines are magnetic field lines connected to this region, showing that there is a magnetic connection to the lower sunlit ionosphere. Only magnetic field lines connected to this region are shown.

It is also likely that some of the electrons in the cold (10 eV or below) populations detected at large distances are lower energy photoelectrons that travel along magnetic field lines too, as predicted by Gan et al. (1992a). This is evident in some pitch angle observations where the detected DEF was slightly higher at these energies at low pitch angles during the T40 blobs, and at pitch angles closer to 180° at T17 during interval A, as described in section 3.

In addition, the three case studies above give us some insight into the structure of Titan's ionospheric tail.

There are some interesting implications of the structure observed on the T40 flyby, where ionospheric plasma blobs and some low density ionospheric plasma without photoelectron peaks were observed. The low energy plasma between 20:50 and 21:22 UT is not continuous like in T17 and the observed DEF is not constant. This suggests that Cassini does not fly through and along the main part of the tail. Furthermore, photoelectron peaks are not present between the blobs. We therefore suggest a few possibilities to explain the observed T40 tail structure.

(1) Flyby close to the actual tail edge. Cassini travels close to the outer part of the tail from 20:55 UT, getting slightly closer to the tail as it approaches Titan. Due to the presence of photoelectron peaks in blobs A and B, these could be parts of the tail that are still magnetically connected to the ionosphere whereas the lower density plasma in between the blobs may have detached earlier and disconnected. This would also explain the higher density in the blobs – more plasma can escape along magnetic field lines, possibly also due to the presence of ambipolar electric fields as discussed in section 1.

(2) Fast dynamic tail. Titan's tail is moving very rapidly about its nominal position between the positive and negative x-axis and possibly some angle to the orbital plane. It crosses Cassini's path at point A and then again at B. The lower density ionospheric plasma without photoelectron peaks between the points could be remains from the tail that passed these locations recently, but having lost their magnetic connection to the ionosphere.

(3) Split tail structure. The ionospheric plasma at A and B could be (separate) split off parts of the tail that Cassini is crossing. These split tails are still connected to Titan's ionosphere. The lower density plasma between the points could be plasma that has come off the main or split tails and is not connected to them or the ionosphere any more.

(4) Detached plasma blobs. The ionospheric plasma detected at A and B used to be connected to the dayside ionosphere when it was closer to Titan but became detached not long before it was detected, which is why the photoelectrons are still present. The blobs could have come off the tail when moving downstream, or due to the motion of a dynamic tail such as a less rapid version of (2).

The tail structure would be very different between T17 (reasonably stationary tail) and (2); hence it is possible that the tail conditions can change from relatively stationary to moving rapidly about its nominal position, however this does not seem very likely. Pitch angle distributions at A and B generally favour the idea that the blobs are still connected to the ionosphere, because the photoelectron peaks are mainly observed at low pitch angles indicating that they are flowing along magnetic field lines. Therefore (4) seems less likely. (3) is quite possible however it might not be a frequent event for parts of the tail to split from the main tail but to keep its magnetic connection to the ionosphere. For these reasons we suggest that (1) or a combination of (1) and (3) are the most likely scenarios.

In contrast to T40, the tail region observed inbound during T17 is continuous. Similarly, the photoelectron peaks are present almost continuously throughout intervals A and B, but with varying intensity. The density of the electrons in interval A is comparable to that of the actual ionosphere. Considering these facts it seems likely that the plasma is part of the main tail, even though the trajectory is at an angle of ~80° to the nominal tail position. Cassini could have entered the tail downstream on its inbound leg and then flown along it towards Titan. It is possible to observe the tail at such a large angle to the nominal tail due to changes in the direction of Saturn's magnetospheric flow, and modulations in the configuration of the magnetospheric magnetic field near Titan. These changes may be due to either internal (periodic or impulsive) or external (changes in the upstream solar wind) effects. It is unlikely that the tail was moving at the time as suggested for T40 in (2)

because the observations were continuous and gathered along a straight line towards Titan. It may be possible that there was a split tail structure (3) similar to that observed during T9 (Coates et al., 2007a) or detached plasma blobs (4) at locations not crossed by Cassini's trajectory during this flyby. Pitch angle observations of the tail region suggest that a considerable flux of photoelectrons is traveling towards Titan, suggesting that a mirroring process operates at a remote location. It is likely that a large amount of photoelectrons are also traveling away from Titan because they can be observed throughout interval A. This cannot be confirmed by pitch angle observations though due to limited coverage as described in section 3. We can also infer from this observation that the minimum tail length at the time of the T17 flyby is ~12000 km = 4.7 R_T (above Titan's surface) based on the distance to the point where the ionospheric plasma is first detected.

3.4. Summary and Conclusions

Solar radiation from the He II line at 30.4 nm can ionize neutral N_2 in Titan's ionosphere. Photoelectrons with energies of 24.1 eV are produced as a result. They can generally be observed in Titan's dayside ionosphere as discrete peaks in CAPS-ELS spectra. We studied three Titan flybys (T15, T17 and T40) where these discrete photoelectron peaks were observed at larger distances (up to 4.7 R_T) from Titan. They are unlikely to be created at such large distances because neutral densities at these distances are too low. We suggest that these photoelectrons originated in the lower dayside ionosphere where neutral densities are sufficiently high. They could then travel along magnetic field lines to the observation sites. T15 modeling results strongly support this idea. Therefore photoelectrons are valuable tracers of magnetic field lines and escape paths from the dayside ionosphere that will allow more in-depth studies of Titan's complex magnetic environment.

We also used the three case studies to understand Titan's tail structure. We discussed different ideas to explain the different tail structure during the T40 and

T17 encounters. For the observed T40 “blob” structures the most likely possibility is that the observations were made during a flyby that was close to the tail edge, possibly combined with a split tail structure. The observed continuous structure during the T17 flyby is likely to be the main tail even though it is at an angle of ~80° to the nominal tail position. We also used these continuous data to determine a minimum tail length of ~12000 km = 4.7 R_T in this case.

4. Electron acceleration regions in Titan's ionosphere

4.1. Introduction

We will describe examples of events that appear at the edge of Titan's ionosphere proper. We refer to these events as 'electron acceleration regions'. In electron spectrograms electrons seem to undergo a change in energy of varying degree as observed by Cassini (up to approximately 100 eV). After describing three case studies we will take a closer look at a survey of these events in order to learn more about where and when they occur.

4.2. Observations

4.2.1. Case study 1: T23

T23 took place on 13 June 2007 with a closest approach altitude of 1000 km. The flyby geometry is shown in Figure 38. The Cassini spacecraft approached from downstream, moving towards Saturn on a southward trajectory inclined to the equatorial plane (on the negative x-axis). The hemisphere of Titan that is on the negative x-axis points away from Saturn. Closest approach took place just on the Saturn facing hemisphere on Titan's dayside near the nominal tail. The outbound leg was on the Saturn facing hemisphere (positive x-axis) as shown in the Figure 38.

Figure 38: T23 flyby geometry in Titan-centred coordinates. Saturn's nominal magnetospheric plasma comes from the positive y-axis and impinges on Titan's (black circle) atmosphere, causing a nominal corotation wake (green) along the negative y-axis. Arrows show directions towards the Sun and Saturn as indicated, and the black line describes Cassini's flyby trajectory 75 minutes before (diamond shape) and after CA.

Figure 39 shows a 2-panel spectrogram of one hour of the T23 flyby, centred at CA (white dotted line). The top panel shows electron data from CAPS-ELS and the bottom panel shows ion data from CAPS-IMS. The electron population < 3 eV

comprises spacecraft photoelectrons which disappear at 08:25 UT and reappear at 08:47 UT. They are not present when the spacecraft potential becomes zero or negative due to Titan's dense ionosphere. Titan's cold ionospheric electron population is present from about 08:27 UT until 08:47 UT. Dayside characteristic photoelectron peaks at 24.1 eV are also visible in this region as discussed in section 3. Typical negative ion signatures can be observed in the ELS data around CA. At the same time, positive ions can be seen in the IMS data where data is available. The dark blue box indicates where IMS did not collect data in order to prevent the instrument from degrading too quickly in Titan's dense ionosphere. The remaining electron populations visible in the data are magnetospheric background plasma. We can start to see a magnetospheric bite out (see e.g. section 3.2.1) at 08:31 UT until 08:47 UT. The bite out is partial at 08:31 UT – 08:34 UT and 08:41 UT – 08:47 UT because some magnetospheric electrons are still present.

Figure 39: T23 ELS (top panel) and IMS (bottom panel) spectrograms. The dark blue box at low energies around CA in the IMS data is a mode to protect the IMS MCPs. Circle A indicates an electron acceleration region. Circle B shows possible pick up ions.

The region of interest is marked by the black circle A in the top panel. It shows a population of electrons undergoing a change in energy. We refer to this region as an 'electron acceleration region'. At approximately the same time we observe a population of ions in the IMS data (circle B). The distributions of these ions are narrow which indicates that they are likely pick-up ions. This is because freshly picked up ions form a ring distribution in velocity space which is seen as a narrow distribution in energy. The ions tend to spread out and scatter after their creation and are hence not seen in narrow distributions any more at later stages of their lives (Coates, 1991).

4.2.2. Case study 2: T36

T36 occurred on 2 October 2007 at a closest approach altitude of 973 km. The flyby geometry is shown in Figure 40. The inbound leg is on the positive x-axis this time, i.e. where Titan's hemisphere points towards Saturn. The trajectory passes through the edge of Titan's nominal tail and then reaches closest approach on Titan's dayside. The outbound leg was approximately in the negative x-axis direction.

Figure 40: T36 flyby geometry in Titan-centred coordinates. Saturn's nominal magnetospheric plasma comes from the positive y-axis and impinges on Titan's (black circle) atmosphere, causing a nominal corotation wake (green) along the negative y-axis. Arrows show directions towards the Sun and Saturn as indicated, and the black line describes Cassini's flyby trajectory 75 minutes before (diamond shape) and after closest approach.

Figure 41 shows a CAPS-ELS (top panel) and CAPS-IMS (bottom panel) spectrogram. We can see spacecraft photoelectrons of energies < 5 eV when the spacecraft potential is positive outside of Titan's dense ionosphere before 04:30 UT and after 04:49 UT. There are some lower energy (mainly < 1eV) spacecraft photoelectrons in the region between 04:27 UT and 04:34 UT, hence the spacecraft potential is still positive here at about 1 V. We can see a population of cold electrons (< 12 eV) that is similar to Titan's cold ionospheric population but more tenuous. Considering the flyby geometry this population is probably part of Titan's tail. We also start to observe a partial magnetospheric "bite out" in this region. This bite out evolves to a region where magnetospheric electrons are essentially missing by 04:39 UT and ends quite abruptly at 04:48 UT. Titan's cold ionospheric electron population is present from approximately 04:36 UT until 04:50 UT. Again, negative ion signatures are present around CA. Photoelectron peaks at 24.1 eV are also visible in the spectrogram, being a characteristic feature of the dayside ionosphere. There are no obvious signs of photoelectron peaks in the observed tail region. This suggests that there is no direct magnetic connection between the dayside ionosphere and this part of the tail.

Figure 41: T36 ELS (top panel) and IMS (bottom panel) spectrograms. The dashed white line marks CA. The dark blue box at low energies around CA in the IMS data is a mode to protect the IMS MCPs. Circle A indicates an electron accereration region. Circle B shows possible pick up ions.

We observe a particularly prominent electron acceleration region on the outbound leg, indicated by the circle A in the ELS spectrogram. The change in energy of these electrons is over 100 eV. Again at the same time, ions are visible in the IMS spectrogram. These may be pick up ions, although the ion distributions are not as narrow in energy as they are during T23.

4.2.3. Case study 3: T48

T48 took place on 5 December 2008 at a CA altitude of 960 km. The flyby geometry is shown in Figure 42. The spacecraft approached Titan from the downstream direction moving northwards on a path strongly inclined to the equator. The inbound trajectory was on the negative x-axis and CA was on the dayside at a low SZA. The outbound leg continued on the negative x-axis. Cassini also continued its high angle trajectory on a northbound path away from the equatorial plane after crossing it near CA.

Figure 42: T48 flyby geometry in Titan-centred coordinates. Saturn's nominal magnetospheric plasma comes from the positive y-axis and impinges on Titan's (black circle) atmosphere, causing a nominal corotation wake (green) along the negative y-axis. Arrows show directions towards the Sun and Saturn as indicated, and the black line describes Cassini's flyby trajectory 75 minutes before (diamond shape) and after closest approach.

Figure 43 shows T48 CAPS-ELS and CAPS-IMS spectrograms. Spacecraft photoelectrons (< 4 eV) are present before 14:11 UT and after 14:38 UT. Inside this time period, Titan's cold ionospheric electron population can be observed. A magnetospheric bite out is present between 14:22 UT and 14:33 UT. Characteristic negative ion and photoelectron peak observations are present in the dayside

ionosphere around CA. Considering the flyby geometry in the x-y plane, one might expect to see a tail population on the inbound leg prior to the ionospheric population. The reason no tail population is observed may be because the actual tail was at an angle to the nominal tail, similar to T17 as discussed in section 3.2.2. Another reason could simply be that Cassini approached Titan at such a high angle to the ecliptic plane that it did not come across the tail. The reason is likely to be a combination of the two.

Figure 43: T48 ELS (top panel) and IMS (bottom panel) spectrograms. The dashed white line marks CA. The dark blue box at low energies around CA in the IMS data is a mode to protect the IMS MCPs. Circles A and B indicate electron accereration regions. Circle C shows possible pick up ions.

During this flyby, we can observe two acceleration regions, indicated by circles A and B. IMS shows some ion data, some of which (circle C) may be pick up ions observed at the same time as the outbound acceleration region. However, the distributions of these are not as narrow in energy as during, for example, T23.

4.3. Survey

A simple survey was conducted of all Titan flybys up to flyby T50. For each flyby it was recorded whether an acceleration region was observed, and whether it took place inbound, outbound, or during both. Possible pick up ion signatures were also noted. The results show that the events generally take place at a larger distance from Titan than the start of the main bite-out region (see section 3.2.1). They also tend to occur outside the photoelectron peak region, i.e. the region in which photoelectron peaks at 24.1 eV can be observed due to local production. The altitudes at which the regions are observed are generally higher than the main electron peak in the ionosphere due to photoionisation and magnetospheric impact ionisation (c.f. Figure 16 and Figure 18). In addition, it was recorded whether the

event took place in the hemisphere of Titan that faces away from Saturn (negative x values on flyby geometry plots), or towards Saturn (positive x values on flyby geometry plots). This has been determined by investigating the flyby geometry for each encounter and considering whether each detected event was observed inbound and/or outbound. 21 events have been identified during 19 encounters of which almost all appear in the hemisphere away from Saturn. Two encounters (including T48) show two acceleration regions (both inbound and outbound); they were flybys during which both legs occurred with negative x-axis values. A large number of these events also seem to be associated with possible pick up ion observations.

4.4. Discussion

We have found that the electron acceleration regions virtually always occur in the hemisphere of Titan that points away from Saturn. At the centre of this hemisphere, the nominal magnetospheric electric field is approximately parallel to the local zenith, i.e. it also points away from Saturn and Titan. This can be demonstrated using Figure 13 in section 1.3.3. The corotation electric field direction is given by $\mathbf{E} = -\mathbf{v} \times \mathbf{B}$. Therefore these events may be regions in which cold, ionospheric electrons are being accelerated in a complex flow field related to the electric field. Another theory is that instead of having cold ionospheric electrons being accelerated, it could be magnetospheric electrons being slowed down by mass loading, a process which removes energy from the flow and hence cools the electrons (also see Hartle et al., 2006). This would explain the association with pick up ions.

Clearly, more analysis is required before drawing definitive scientific conclusions. As future work we plan to determine the actual electric field direction; ideal conditions are often very different from actual conditions. We hope to achieve this by using Cassini magnetometer data and also CAPS ion flow data to determine **E** using $\mathbf{E} = -\mathbf{v} \times \mathbf{B}$. A study by Arridge et al. (2011) investigating the electric field variability near Titan may also be valuable in determining the actual electric field direction. A better knowledge of the electric field during the signatures may improve our understanding of the exact mechanism causing them. The convection electric field due to the solar wind may also need to be considered if the magnetospheric configuration in this region shows dominantly Dungey-cycle characteristics (also see section 1.3.1), rather than the Vasyliunas cycle.

Additionally, in order to determine whether the ions originated in Saturn's inner magnetosphere or at Titan, it will be interesting to study the ion composition where possible and also pitch angle distributions. It may be possible to achieve this by using CAPS - IMS Time of Flight (TOF) data. Knowing the source of the ions might explain which ions are freshly picked up ions and hence whether they are related to the acceleration regions.

4.5. Summary

- We reported on observations of regions in which electrons undergo a change of up to ~100 eV in the topside of Titan's ionosphere
- We refer to these regions as electron acceleration regions
- Three case studies were analysed: T23, T36 and T48
- Survey results indicate that the regions are observed predominantly in the hemisphere of Titan where the corotation electric field points away from the moon

- A number of these events are also associated with possible pick up ions
- The change in energy may be due to ionospheric electrons being accelerated in a complex flow field related to the electric field
- Another theory is that magnetospheric electrons are being decelerated by mass loading, explaining the association with pick up ions

5. Negative ion observations in Titan's ionosphere

5.1. Introduction

The first results on negative ions at Titan using CAPS-ELS were published in Coates et al. (2007b) and Waite et al. (2007) which describe the ions' discovery and initial analysis. The method of analysis has been improved and extended upon by the author in order to investigate the mass and density trends of the negative ions. Due to the unusual nature of analysing unexpected negatively charged ions with an electron spectrometer, the main results of the work presented in this chapter are not only the scientific results such as mass (section 5.5) and density (section 5.6 and 5.7) trends, but also the methods of analysis (sections 5.1.5 to 5.3 inclusive, and the methods in sections 5.5, 5.6 and 5.7).

Section 5.4 provides a summary of Vuitton et al. (2009). The author contributed to this study by providing data analysis and results of the observational data using CAPS-ELS which were compared with the main modelling results. The main reason we have a separate section based on this publication is to introduce the different chemical reactions and because of the results' particular relevance to the low mass negative ion analysis.

Some of the initial scientific mass trend studies have been published in Coates et al. (2009). These are presented in section 5.5. The author was responsible for the majority of the data analysis reported by Coates and colleagues. In section 5.5 an update is presented of this study using a larger data set (due to an increased number of flybys) and an improved data analysis method. We also review and re-analyse some of the scientific results. These are discussed further in later sections (e.g. 5.8). The new scientific result of a possible seasonal dependence is important and may be published as part of an updated mass trend study.

The other scientific results presented in sections 5.6 and 5.7 are presented for the first time in this thesis and we plan to publish them in the near future. We may also publish the data analysis methods separately.

5.1.1. Introducing negative ions

A negative ion is "an atom or molecule to which an extra electron has been attached, giving the whole system a net negative charge" (Andersson, 2009). Charged particles are not subject to any long range Coulomb forces due to neutral atoms. How can negative ions then exist? The electron is not attracted by neutral particles (Andersson, 2009). However, if an electron gets close to the electron cloud surrounding a neutral atom, an electric dipole will be induced which can attract the electron. In this case an induced electric dipole potential will then trap this electron. The atom gains energy in this process, which is described as the binding energy of the negative ion or the electron affinity (EA) of the neutral atom. The EA is defined as

$$EA(A) = E_{tot}(A) - E_{tot}(A^-)$$

Where $E_{tot}(A)$ is the total energy of the neutral atom A ground state and $E_{tot}(A^-)$ the total energy of the negative ion A- ground state. Therefore, a positive EA implies a stable negative ion. A table of some EAs is presented later in section 5.4.

Negative ions in interstellar clouds have been observed and modelled extensively and are summarised by Sittler et al. (2009a). Negative ions have also been observed at comets, e.g. in the inner coma of comet Halley (Chaizy et al., 1991). In addition, negative ions have been measured in the Earth's ionosphere (Coates et al., 2007a) where they coexist with electrons in the D-region (e.g. Hargreaves, 1992). More

recently, negative ions have also been detected at Saturn's moon Enceladus using the CAPS-ELS (Coates et al., 2010).

The first observations of negative ions at Titan were reported by Coates et al. (2007a) and Waite et al. (2007) at altitudes around 1000 km and above. Negative ions were completely unexpected at these altitudes before the arrival of Cassini in the Saturn system. They were only expected at lower altitudes and in the cosmic ray induced ionosphere below 200 km (e.g. Hunten et al., 1984, Borucki et al., 2006). At lower altitudes, they may contribute to possible lightning discharges (Desch et al., 2002). Vuitton et al. (2009) discuss pre-Cassini studies that modelled negative ions in this lower region of the atmosphere.

5.1.2. Introducing CAPS –ELS observations of negative ions at Titan

A typical Titan flyby with negative ion detections is shown in Figure 44. Most negative ion signatures in ELS spectrograms obtained when CAPS was actuating can be identified as a vertical "spike" such as the one inside circle 'B' in Figure 44. These are detected at energies up to 2550 eV, with the lowest energy starting at a few eV. Higher energy ions are generally only detected at lower altitudes, i.e. near closest approach on low encounters (e.g. 1000 km). At higher altitudes (e.g. 1300 km), the main long spike is missing and the signatures generally look like that inside circle 'A' in Figure 44. Signatures at intermediate altitudes can be seen between the two circles and also after 'B' on the outbound leg. We refer to events such as those inside circles 'A' and 'B' as negative ion *signatures*. Each signature is a collection of peaks in the energy spectra and lasts approximately 30 seconds as the ELS FOV is moved through the *ram direction* (the direction in which the spacecraft is travelling).

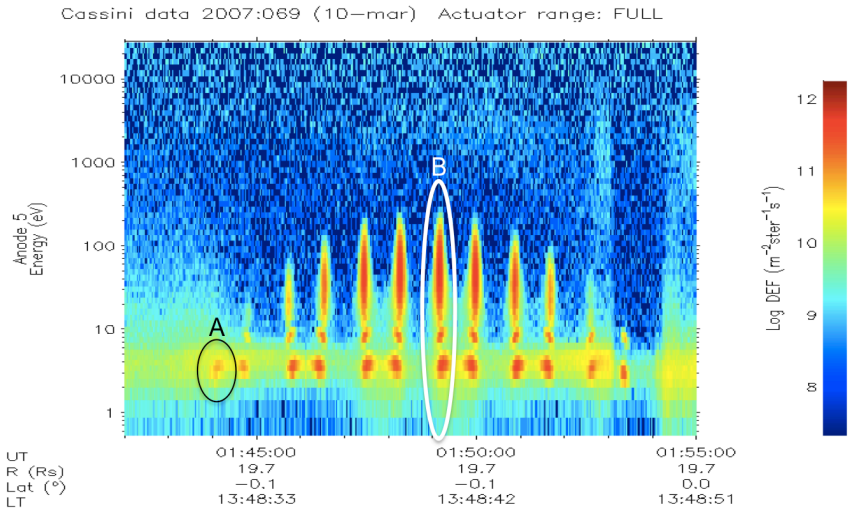

Figure 44: T26 electron spectrogram. Circles A and B indicate examples of negative ion signatures.

We will now examine why these signatures are due to negatively charged ions, rather than electrons (Coates et al., 2007b). The instrument actuator range when the spacecraft passes through Titan's ionosphere is usually around 26° although this varies slightly. The actuator is usually set to actuate between approximately 78° and 104° during typical Titan flybys. The events are detected only when the actuator points in the ram direction – this is why we see a number of signatures rather than a continuous set of data. Ion velocities in Titan's cold ionosphere are small compared to the spacecraft velocity (~6km/s), in contrast to the electrons whose thermal velocities are much higher. The ions are therefore highly supersonic in the frame of the spacecraft and can only enter the instrument when it points in the ram direction. On the other hand, typical electron populations in the magnetosphere or Titan's ionosphere are subsonic and have much more isotropic distributions. They are hence detected at any actuator position.

As described by Coates et al. (2007b), we can convert the detected negative ion energy into mass. This can be done by assuming the observed ram energy as the kinetic energy of the ions, and the spacecraft velocity as the relative speed for each encounter. This is a reasonable assumption, as the velocities of these cold ions in

the Titan frame are expected to be much lower than the spacecraft velocity in the same frame (Crary et al., 2009). The negative ion mass *m* is therefore

$$m = \frac{2E}{v^2}$$

Equation 25

where *E* the observed energy and *v* the spacecraft velocity in SI units. This can be written as

$$m_{amu/q} = cE_{eV}$$

Equation 26

where m_{amu} is the negative ion mass in amu/q, E is the observed energy in eV, and *c* is the conversion factor which consists of the conversion of kg to amu and J to eV, and the value of the spacecraft velocity:

$$c = \frac{1.9297 * 10^8}{v^2}$$

Equation 27

where *v* is in $m.s^{-1}$. Using this method, a singly charged negative ion with an observed energy of 100 eV observed at a spacecraft velocity of 6 km s^{-1} would have a mass of 536 amu, or more generally $m_{amu/q}=5.36\ E_{eV}$. The conversion factor *c* changes as the spacecraft velocity varies. The spacecraft velocity range of the negative ion flybys discussed in this study ranges between approximately 5.96 km s^{-1} and 6.35 km s^{-1}. The theoretical upper mass range limit of the CAPS-ELS instrument using this conversion method is approximately 150,000 amu/q (Coates et al., 2007b). The highest mass observed in Titan's ionosphere to date is 13,800 amu/q.

It should be noted that ELS measures E/q. Hence if an ion carries multiple charges then the mass would be larger (e.g. Coates et al., 2007b). This may be the case for ions with very large masses (e.g. aerosols: Horanyi et al., 2004) for which the calculated values can be treated as lower limits. Each negative ion signature in ELS spectrograms essentially represents a mass spectrum. Two time slices at the times of the signatures inside 'A' and 'B' are shown in Figure 45 and Figure 46, respectively. These energy spectra include the negative ion counts and also the ambient electron counts. In Figure 45 one prominent peak can be seen at 3.5 eV which corresponds to the kidney shaped signature inside circle 'A' in Figure 44. This peak is also present in Figure 46 at the same energy in addition to another similar peak and a much broader peak at higher energies. The two lower energy peaks correspond to the two kidney shaped negative ion signatures inside circle 'B' and the broader peak to the vertical spike. There is also a small bump near the broader peak. We examine the structure of negative ions spectra in more detail in section 5.3.

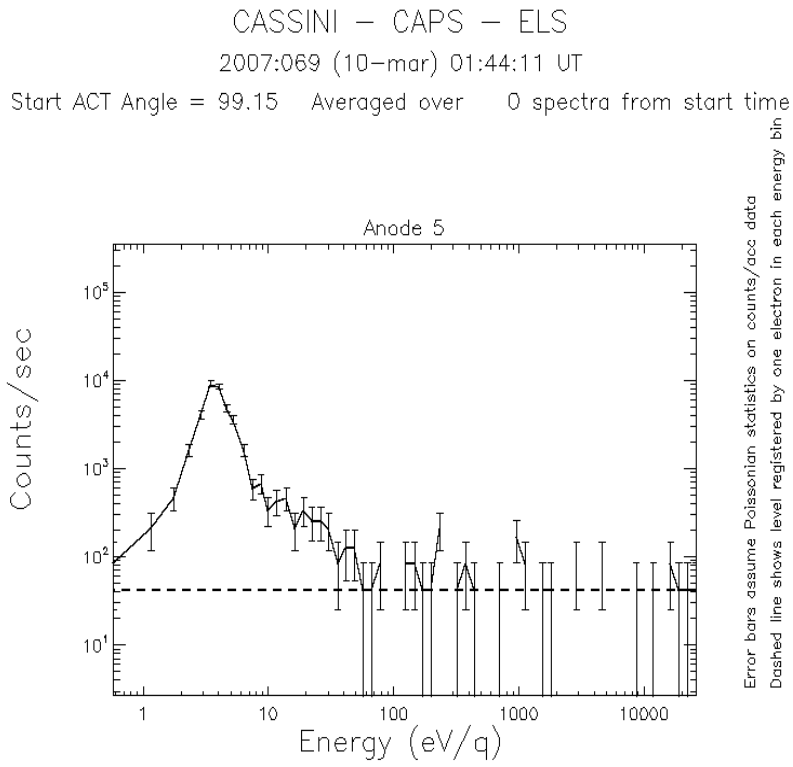

Figure 45: T26 CAPS-ELS spectrum at 'A' in Figure 44 showing the negative ion signature.

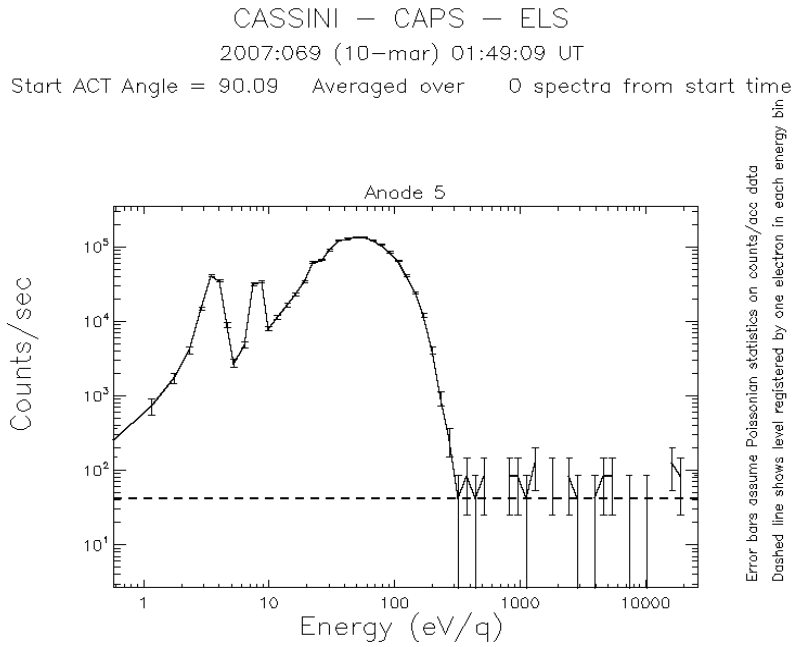

Figure 46: T26 CAPS-ELS spectrum at 'B' in Figure 44 showing the negative ion signature

Coates et al. (2007b) describe a number of candidate species for some of the mass ranges observed. These were summarised in a table by Coates (2009) which is shown in Table 2.

Table 2: Some candidates of negative ion species for some of the mass ranges observed. From Coates (2009).

Coates et al. (2009) continued the analysis of CAPS observations of negative ions by investigating where the highest masses are found. We discuss the findings and present an update on the topic in section 5.5.

5.1.3. The role of negative ions at Titan

The combination of nitrogen and carbon (from methane) in Titan's atmosphere makes Titan a natural production factory of organic synthesis with high abundances

of nitrogen and carbon compounds (e.g. hydrogen cyanide HCN) (Liang et al., 2007, and references therein). One of the reasons for this is that Titan has a relatively low gravity resulting in a high rate of hydrogen escape (e.g. Yelle et al, 2006). This results in a low hydrogen abundance and rich hydrocarbon production. Large enough orders of hydrocarbon and nitriles can condense to form aerosols.

Waite et al. (2010) explain the current understanding of organic material formation in Titan's upper atmosphere using Figure 47. Solar ultraviolet radiation and energetic particles causing ionisation and dissociation of methane and molecular nitrogen set off a rich ion neutral chemistry. Heavy positive ions and neutrals are produced which eventually form macromolecules. A large number of these are negatively charged. The macromolecules precipitate from the formation layer around 1000 km to 550 km where they are slowed by atmospheric viscosity to form the haze layer.

Figure 47: Cartoon illustrating processes in Titan's upper atmosphere (adapted from Waite et al., 2007)

The sources and processes resulting in Titan's aerosols has been a long-standing question (Liang et al. (2007), and references therein). Waite et al (2007, 2010) and Coates et al. (2007b) explain that the very high mass negative ions may not be true molecules but most likely aerosols are formed by the clumping of smaller molecules. Liang et al. (2007) state that the synthesis of complex hydrocarbon and nitrogen compounds is believed to eventually saturate resulting in coagulation and precipitation. The chemical compositions of condensable species are still being identified and discussed. Some are considered in e.g. Liang et al (2007) who believe that C_6N_2 is the simplest condensable compound. Waite et al. (2007) describe possible aerosol formation processes and explain that benzene is an important one of these condensable species.

Sittler et al. (2009) propose that the detected heavy ions may be seed particles for aerosols at much lower altitudes. These could be in the form of hydrogen atom containing PAHs (C_nH_x). Another possible form may be a type of molecule that does not contain hydrogen atoms: Hollow shells of carbon atoms in a cage structure (Bohme, 1992) called fullerenes such as C_{60} which has a spherical shape and a mass of 720 amu, or C_{70} with ellipsoidal shape and a mass of 840 amu. Due to the hollow nature of fullerenes, other ions such as water, oxygen or hydroxyl ions from Saturn's magnetosphere can be implanted inside them and transported closer to the surface with them. Sittler et al. (2009) also explore the trapping of such particles and its possible consequences. They note that oxygen is an important ingredient of all amino acids attributed to life and discuss the exobiological importance of this. They also discuss the mass flux of the heavy ions and their transport to the surface quantitatively and compare their results to the aerosols at altitudes <100 km investigated by Tomasko et al. (2005) using the Huygens DISR imaging system. The role of fullerenes is also reviewed by Sittler et al. (2010).

Liang at al. (2007) found aerosol particles in Titan's mesosphere and thermosphere (reaching altitudes above 1000 km) using the Cassini Ultraviolet Imaging Spectrograph (UVIS) stellar and solar occultations at Titan. They use Mie theory and assume a radius of 12.5 nm for the particles to fit the spectra. They suggest these particles are tholins and the number density at 1000 km is approximately 50 cm^{-3}. They explain that the altitude range between 468 km and 550 km is likely the primary aerosol source region but also that aerosols are extensively distributed in the thermosphere due to scattering signatures at 1250 km.

Michael et al. (2011) computed concentrations of charged aerosols in the upper atmosphere of Titan (950 km – 1200 km). They estimate the aerosol mass density to be 1-10 kg/m^3 and also explain that the aerosols must have a radius smaller than 10 nm in order to agree with observational CAPS-ELS data.

Ågren et al. (2012) report the detection of negative ions with RPWS Langmuir Probe data in the deep ionosphere of Titan during Cassini's lowest encounter so far, T70. This encounter had a CA (Closest Approach) of 880 km which is 70 km lower than any other previous Cassini Titan flybys. Using the data they present negative ion densities comparable to, or higher than the measured electron density of 760 cm^{-3}. CAPS did not point in the ram direction during this encounter due to mission planning constraints, therefore we cannot compare these densities to ELS data.

Vuitton et al. (2009) use an ionospheric chemistry model to investigate the lower mass ions observed with CAPS-ELS. We discuss this study in some detail in section 5.4.

5.1.4. Negative ion flybys used in this study

Negative ion signatures have been detected with CAPS-ELS during 34 encounters between the first Titan flyby (TA) and T76 (8 May 2011). They are detected if (i) the encounter is low enough (~<1400 km) and (ii) the instrument points in the ram direction.

Flyby	Date	UT	DOY	Altitude	SLT	TLT	Latitude	SZA	In shadow?
		hh:mm:ss		km	hh:mm:ss	hh:mm:ss	° N	°	
TA	26-Oct-04	15:30:26	300	1176	10:36:16	16:53:26	39.4	92.9	no
T16	22-Jul-06	00:24:58	203	954	02:26:42	18:29:17	87.8	106.7	no
T17	07-Sep-06	20:17:33	250	1000	02:19:47	10:44:30	21.7	41.8	no
T18	23-Sep-06	18:58:54	266	960	02:17:03	14:23:49	70.5	89.6	no
T19	09-Oct-06	17:30:00	282	980	02:14:13	14:14:34	61.4	81.3	no
T20	25-Oct-06	15:57:15	298	1042	02:11:40	10:52:39	8.6	29	no
T21	12-Dec-06	11:40:05	346	1002	02:02:51	20:52:30	49.4	128.4	no
T23	13-Jan-07	08:38:03	13	1004	01:57:26	13:53:46	33	54.3	no
T25	22-Feb-07	03:11:57	53	1003	13:51:21	00:30:38	27.9	163.9	(yes)
T26	10-Mar-07	01:47:27	69	981	13:48:38	01:25:32	23.6	157.3	(yes)
T27	26-Mar-07	00:23:50	85	1013	13:46:03	01:49:46	42.9	141.9	(yes)
T28	10-Apr-07	22:56:51	100	992	13:43:23	01:21:14	44.1	144.2	(yes)
T29	26-Apr-07	21:31:34	116	983	13:40:47	01:10:22	51.9	138.2	(yes)
T30	12-May-07	20:08:54	132	961	13:38:21	01:06:30	62.8	128.1	(yes)
T32	13-Jun-07	17:46:52	164	965	13:35:00	04:35:48	87.2	102.9	no
T36	02-Oct-07	04:41:57	275	973	11:29:25	16:45:54	-59.2	71.8	no
T39	20-Dec-07	22:58:08	354	970	11:21:52	11:24:47	-69.1	60.4	no
T40	05-Jan-08	21:30:30	5	1015	11:19:41	14:28:17	-11.1	36.6	no
T41	22-Feb-08	17:32:37	53	1003	11:13:04	12:48:37	-33.2	27.6	no
T42	25-Mar-08	14:27:15	85	1001	11:07:07	12:49:10	-28.9	24.3	no
T43	12-May-08	10:01:52	133	1002	10:59:11	13:46:27	17.8	36	no
T46	02-Nov-08	17:38:11	308	1109	10:28:14	00:37:34	5.3	170.6	yes
T48	05-Dec-08	14:25:36	340	961	10:22:18	10:25:44	-11	24.5	no
T49	21-Dec-08	12:59:16	356	972	10:19:24	06:36:19	-47.5	81.3	no
T50	07-Feb-09	08:50:52	38	967	10:12:33	01:42:58	-33.8	136.2	(yes)
T55	21-May-09	21:26:08	141	966	21:57:06	22:00:27	-19.1	144.4	(yes)
T56	06-Jun-09	19:59:12	157	968	21:54:40	22:00:57	-28	139.5	(yes)
T57	22-Jun-09	18:31:10	173	955	21:52:10	22:07:31	-34.9	135.8	(yes)
T58	08-Jul-09	17:02:35	189	966	21:49:38	22:07:42	-44.7	128.5	(yes)
T59	24-Jul-09	15:32:35	205	957	21:47:00	22:08:20	-54.7	120.6	no
T61	25-Aug-09	12:50:29	237	961	21:42:18	18:09:34	-18	92.4	no
T64	28-Dec-09	00:16:51	362	952	16:57:49	17:19:36	82.7	86.5	no
T65	12-Jan-10	23:10:35	12	1074	16:56:39	04:38:16	-82.2	95.2	no
T71	07-Jul-10	00:22:35	188	1004	16:03:36	07:22:56	-56.3	83	no

Table 3: Negative ion flybys. This table shows information about all flybys with observed negative ion signatures that were used in this study. DOY – 'day of year', SLT – 'Saturn Local Time', TLT – 'Titan Local Time', SZA – 'Solar Zenith Angle'. Each 'yes' in parenthesis in the 'in shadow?' column means that part of the flyby where negative ions were observed was in shadow (extended version of table from Coates et al., 2009). The yellow highlighted flybys were analysed in the Coates et al. (2009) maximum mass study which we describe in more detail in section 5.5.

We can see that most of the CA altitudes are below 1100 km and a considerable number are below 1000 km. The altitude range for most flybys is up to around 1200 km but some negative ions are detected up to almost 1400 km. We also notice that the flybys occur in Saturn local time groups i.e. there are groups of flybys that occur at a similar local time, e.g. T16 – T23 all occurred around 02:00 Saturn local time. The Titan Local Time, latitude and SZA (solar zenith angle) actually vary considerably during a flyby because of the fast flyby speed of approximately 6 km/s; for instance even though the SZA of T40 at its lowest altitude negative ion detection is 36°, the SZA angle range during this flyby from the first signature to the last is 55° to 19°. The 'in shadow' column indicates when the spacecraft was flying through a region where the solar radiation is occulted by Titan (i.e. Titan's nightside). Each 'yes' in parentheses indicates when only some of the detected negative ion signatures were observed in shadow. We need to keep in mind that even though the terminator at the surface is at SZA = 90°, it is at a higher SZA at higher altitudes. This is discussed in more detail in section 5.6.

Cassini arrived in the Saturn system in 2004 which was after the northern winter solstice of 2002 for both Saturn itself and Titan. Equinox occurred in mid-2009 and the northern summer solstice will be in 2017. Therefore the earlier flybys may see some late winter effects in the northern hemisphere and late summer effects in the southern hemisphere, whereas the more recent flybys occurred closer to equinox.

5.1.5. Effects of spacecraft rotations

The negative ion signatures are generally detected in the two instrument anodes that are closest to the ram direction. During most flybys, these are the two central anodes (anodes 4 and 5), however there have been several cases where the ram direction was closest to other anodes. This is simply a result of different mission planning constraints. During some flybys, negative ion signatures or signature

traces are detected in more than two anodes. This happens as a result of a spacecraft rotation during the flyby and is not uncommon. An example is shown in Figure 48. During this flyby, most of the signatures can be seen in anodes 4 and 5, however, there are also signatures in anode 6 on the inbound leg, and in anode 3 on the outbound leg. For each signature, the one with the highest counts is chosen, which is also the anode closest to the ram direction. The white circles in Figure 48 indicate which signatures were selected. This is discussed further in the next section.

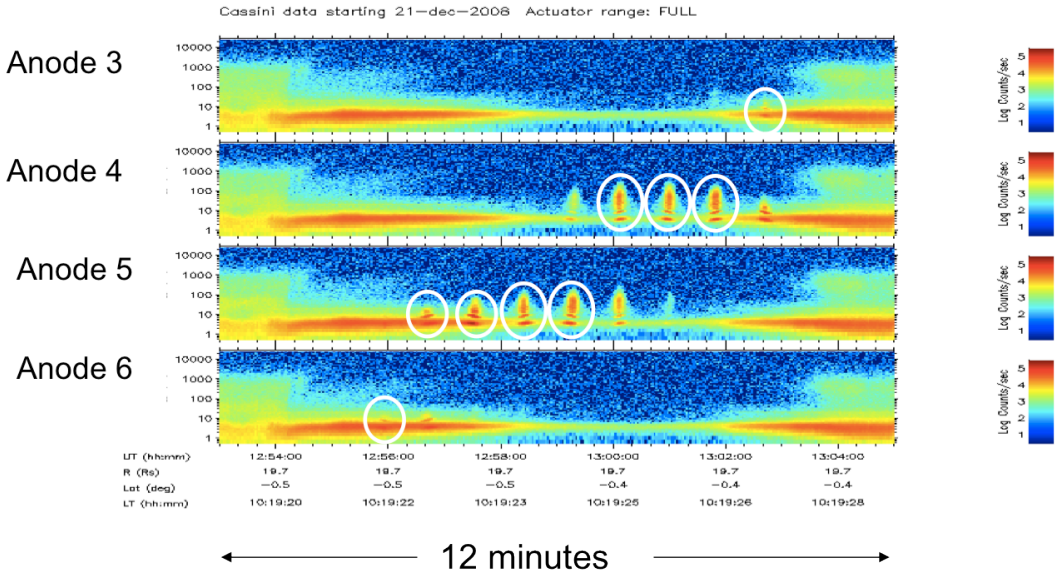

Figure 48: T49 ELS spectrogram - example of a spacecraft rotation. The anode that is closest to the ram direction changes as the spacecraft rotates, therefore negative ion signatures are observed in four different anodes (in this case). The white circles indicate which negative ion signatures were selected.

5.2. Method of obtaining normalised negative ion counts

In this section we describe how we obtain a type of negative ion normalised count rate from raw CAPS-ELS counts (see section 2.2.1) that takes into account the electron background, the response of different anodes, the spacecraft potential and effects that result from a non-zero spacecraft potential. The dataset resulting from this derivation forms the basis of all subsequent negative ion data analysis in this work.

5.2.1. Negative ion signature selection

The first step in this analysis is to find a negative ion signature. The spike-shaped structures are usually found within +/- 15 minutes of CA and are very obvious to spot during the vast majority of flybys. To check that a signature is due to negative ions rather than electrons we need to compare the spectrograms using a number of different anodes. If the signatures appear only in the anodes closest to the ram direction, we can use the fact that typical ambient electron populations have much more isotropic distributions and are visible in all directions whereas the negative ion signatures are only observed in the ram direction, as described in section 5.1.2.

The next step is to identify the anode with the strongest signature. This is done by simply comparing the maximum count rates of the two anodes closest to the ram direction and selecting the one with the highest count rate. As described in section 5.1.5, the spacecraft could be going through a rotation which means the ram direction changes with respect to the anodes. Therefore individual signatures during the same flyby need to be checked and the correct anode chosen. An example of which anodes were used in T49 is shown in Figure 48.

The centre of the negative ion signature can now be identified by comparing raw counts spectra of the signature. Sometimes the peak count rate of different masses occurs at slightly different times during the signature. The centre of the signature is selected where most of the count rate peaks fall. In order not to miss any such peak counts, four energy sweeps before and after the selected centre of the signature are also selected. This means we are now looking at the centre of the signature +/- 8 seconds. A typical negative ion signature lasts approximately 26 seconds. This period is from the time the spectrum starts to be different from other anodes that are not pointing in or near the ram direction due to the first signs of the negative ion signature, until the spectrum again resembles that of neighbouring anodes. However, the period of time during which a negative ion signature is observed sometimes varies widely. There are a number of observations where there is not even a gap between two negative ion signatures, though only at low energies. This is due to an effect that was named the *actuator walk* and is described in more detail in section 5.2.5.

We chose eight seconds before and after the centre of the signature because this time period seems to include the maximum counts in each energy bin as part of the negative ion signature. We decided not to select a shorter time period because this might not cover the maximum counts for all energies. We decided not to select a longer time period because this would cause problems with the electron background subtraction, as we shall see shortly. We also want to stay close to the centre of the signature for the following reasons: In later sections of this chapter we look for mass and density trends at, for instance, different solar zenith angles (SZA). We can currently only assign one SZA for each negative ion signature, yet the time stamps of the data taken can in theory be anywhere during the time period of the negative ion signature centre +/- 8 seconds. Therefore we cannot allow this time period to be very long because then the SZA would be more inaccurate for some readings. In practice and using the +/- 8 second time period this is not a big

problem because the majority of peak times selected are either the central time stamp, or only one or two energy sweeps away from the central time stamp.

In order to select the maximum count rate in each energy bin we now loop over the 9 energy sweeps. The resulting array has 63 entries for each energy bin. The content of each entry is the maximum count rate from the 9 selected energy sweeps.

5.2.2. Anode scaling

In order to account for the fact that different anodes have different instrument responses, we need to apply a scaling factor. We use anode 5, one of the two central anodes, as the default anode. Therefore as part of the process we multiply the count rate of each anode used by the scaling factor GF_{sc}:

$$GF_{sc} = \frac{GF_5}{GF_n}$$

Equation 28

where GF_5 is the geometric factor of anode 5 and GF_n is the geometric factor of the anode being used.

5.2.3. Spacecraft potential shift

We need to take into account the electrical potential of the spacecraft when dealing with detected count rates and energies. The spacecraft potential varies throughout a flyby, therefore we adjust the value for each signature. RPWS measurements of the spacecraft potential were kindly made available to this study (pers. communication with RPWS team, 2012). The times provided mostly do not

match the times of the negative ion signatures exactly and we use the time that is closest.

In order to subtract the spacecraft potential, we need to convert the data into phase space density. According to Liouville's theorem, phase space density is conserved during a shift in particle energy, therefore the subtraction must be done in phase space density. Once the subtraction is complete, the data are converted back (Baumjohann and Treumann, 1997).

5.2.4. Background subtraction

The electron background subtraction is an important part of obtaining a form of normalised negative ion counts. The data we have described so far still include all counts registered in the instrument. This includes the electron counts which we also see in anodes where no negative ion signatures are detected. We will now examine a number of methods that have been tested to remove this electron background, such that the remaining counts match, as accurately as possible, those due to the negative ions only.

There are two main background subtraction methods: (i) "*gap subtraction*" and (ii) "*other anode subtraction*". *Gap subtraction* selects a sample of electron counts before and/or after the negative ion signature of interest, usually in the gap between two consecutive signatures. *Other anode subtraction* uses a sample at the time of the negative ion signature central time stamp but using an anode where no traces of negative ions are present.

Both principles have advantages and disadvantages over the other. The background sample using *gap subtraction* is not taken at the same time as the negative ion signature and may therefore be different to the background when the

ions are detected. This depends on the local variability of Titan's ionosphere. An additional problem with this method is that sometimes there is no clear gap and therefore a pure background cannot be subtracted without subtracting some negative ion traces too. In these cases the background sample needs to be taken from a different gap that may be at a greater separation from the signature both in time and hence also in space. This of course causes problems with consistency and much larger uncertainties.

With *other anode subtraction* a time that coincides with the negative ion signature is chosen. However the problem with this method is that electron distributions are not perfectly isotropic and thus there are differences from anode to anode. These differences are generally larger the further the selected background anode is away from the negative ion signature anode. Therefore an anode needs to be selected that is as close to the ion anode as possible but that also does not show any traces of negative ion signatures such that no actual ion counts are subtracted. Furthermore, an additional source of uncertainty is introduced: the scaling factor to account for different anode geometric factors, as described in section 5.2.2.

After numerous tests we decided to use a form of *other anode subtraction*. Quantitatively, the electron background samples subtracted using the two different methods are comparable, provided there is a clear gap between the negative ion signatures, and the local variability of Titan's ionosphere is low. However, when gaps are not clear, and/or the local electron environment is more variable over short periods of time, gap subtraction samples can fluctuate considerably. *Other anode subtraction* provides much more reliable and consistent electron background samples. In addition, the main sources of uncertainty using this method can be analysed. This analysis is described in section 5.6.2.

To select the appropriate background anode when using *other anode subtraction*, we need to again compare the data in different anodes using spectrograms and

spectra. The anode that does not show any negative ion traces and is physically closest to the previously selected ion signature anode is chosen. We now follow a method similar to the ion signature selection. We choose the same time period as that used to find the maximum count rate for each energy, i.e. the centre of the ion signature +/- 4 energy sweeps. We loop over all energies, again selecting the maximum count rate at each energy and end up with an array that is the same format as the negative ion array. The data can now be scaled and the spacecraft potential corrected as described above. Finally, this electron background can be subtracted from the main data set, leaving a set of normalised negative ion counts.

5.2.5. The actuator walk

The 'actuator walk' refers to an effect on the negative ion signatures that can be observed in ELS spectrograms. We initially believed it to be related to the motion of the actuator alone, hence it was named the actuator walk. We show a relatively extreme case of the effect in a T27 spectrogram in Figure 49. It shows T27 negative ion signatures around CA (00:24) in anodes 6 and 7, and traces in anode 5 and 8. The 5th panel indicates the changing actuator angle and the bottom panel an indication of the spacecraft attitude. The fact that the curves are not horizontal lines means that the spacecraft is slewing slowly. This is why the signatures are initially the most prominent in anode 7 and after CA they become stronger in anode 6.

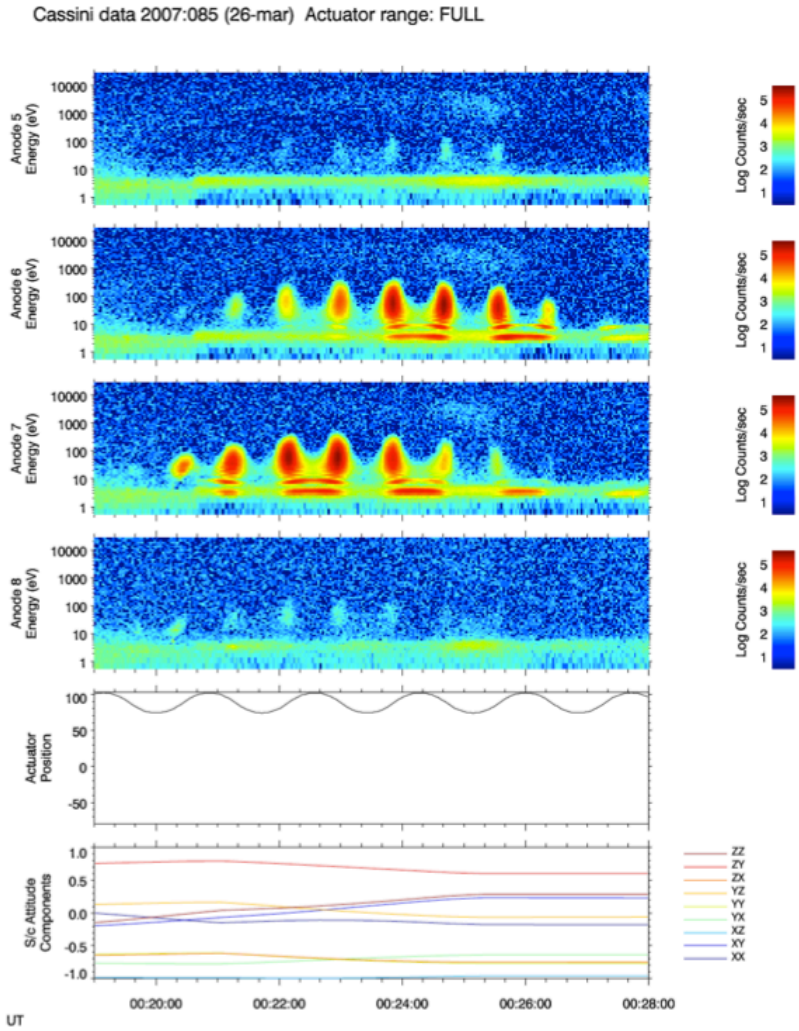

Figure 49: T27 spectrograms, instrument and spacecraft information. From top to bottom: Spectrograms of anode 5, 6, 7 and 8, actuator position showing the angle to the central position, and spacecraft attitude data. The fact that the curves in the bottom panel are not straight means that the spacecraft is rotating. Clear negative ion signatures can be seen in anodes 6 and 7; negative ion traces are also visible in anodes 5 and 8. The negative ion signatures in anodes 6 and 7 show relatively strong effects of the actuator walk.

Instead of seeing straight, vertical signatures when the instrument points in the ram direction and equally sized gaps in between as one might expect, we see a number of irregularities that we refer to as actuator walk effects. When the actuator angle is increasing, i.e. approaching its maximum value, the two lower energy (or mass) parts of the signature are first observed at a slightly lower energy which increases as the actuator angle gets closer to its maximum. When the actuator angle is decreasing and approaching its minimum, the two lower mass parts of the signature are detected at a slightly higher energy initially which then decreases as the angle gets closer to the minimum. This effect is also often observed during less

affected flyby data, e.g T26 (Figure 44). During such less affected flybys, the two lower mass parts can be described as looking 'kidney shaped'. In more strongly affected cases such as T27, the effect is so extreme that the two signatures before and after actuator angle maxima seem to merge together and pair up, such that the signatures at low energies do not form discrete peaks any more. The result is what appears to be one large, combined signature. On the other hand, at actuator angle minima there is a greater gap between the ion signatures.

The higher energy (mass) parts of the ion signatures are generally not as affected as the lower masses but tend to slant out and then curve back. They slant to the left when the actuator angle is increasing, and to the right when the angle is decreasing. The signature 'pairing' at actuator angle maxima is also present but the effect is not as extreme and the signatures do not bleed together like the lower mass signatures do. The peak count rate is also still at the centre of the signature, whereas at lower masses the count rates are more constant throughout the 'paired' signature.

Depending on the flyby, some signatures are also much longer in duration, for example T27 in Figure 49. In less extreme cases (e.g. T26 (Figure 44) or T16 (Figure 51 described in the next section) the signatures are narrower and the slanting effect is still present but the signatures do not quite pair up and bleed together as in T27 (Figure 49).

Further analysis by Jones et al. (2011) shows that part of the explanation as to what causes the actuator walk effects lies in the spacecraft potential. Negative ions are generally observed arriving from a direction slightly closer to the spacecraft surface than the ram direction. Positive ions, on the other hand, are generally observed to arrive from a direction further away from the spacecraft. The least massive ions are affected the most; the arrival direction is therefore a function of mass. This phenomenon can therefore be explained by the deflection in the ion trajectories

near the spacecraft as a result of the negatively charged surface, which is demonstrated in Figure 50.

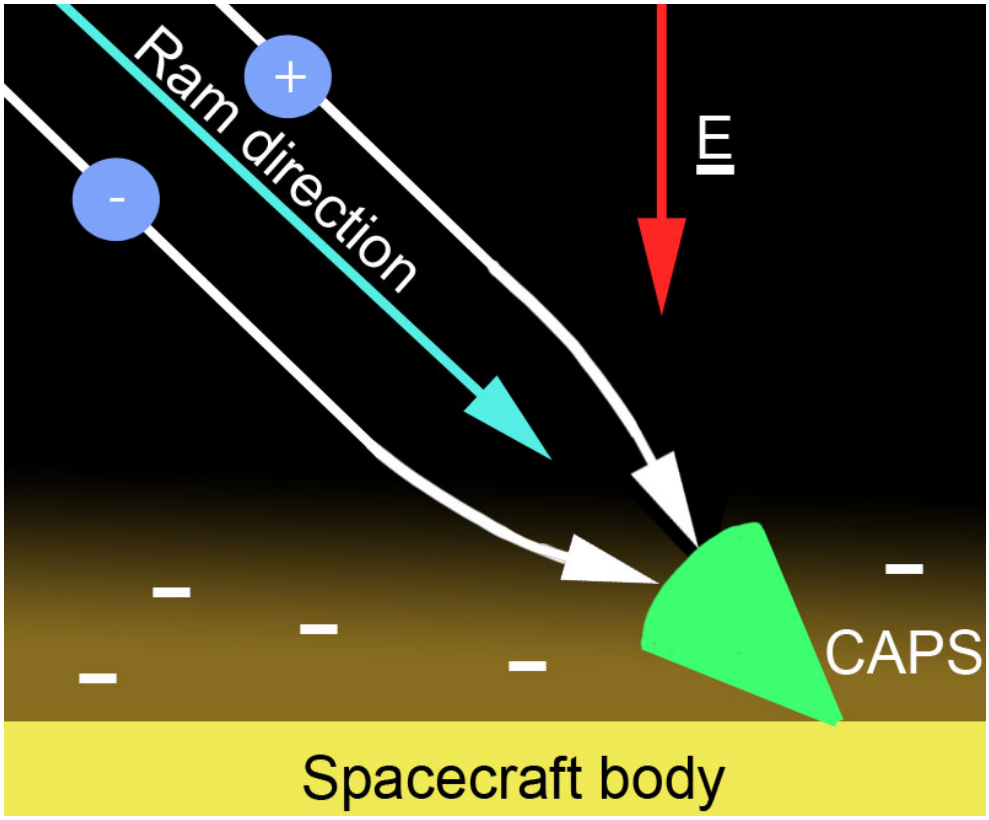

Figure 50: The actuator walk. Ion paths get deflected as a result of the negatively charged spacecraft surface. (Jones et al., 2011)

However, if this is the only cause, then the effect would be strongest when the spacecraft potential is more strongly negative, which is only sometimes the case. Hence there may be other factors affecting the degree of this ion deflection. One of these may be ion winds (as observed for positive ions by Crary et al., 2009; Jones et al., 2011). Further work will include testing the magnitude of the deflections as a function of actuator angle because, for example, the range of actuation is not always the same for every Titan flyby. Also a more detailed analysis of the spacecraft potential dependencies is required.

It is also interesting to see that the anodes that point near the ram direction, e.g. anodes 5 and 8 in Figure 49, see traces of higher mass ions, but no traces of lower

mass ions. This suggests that maybe the lower mass ion beams are narrower, or as suggested above, more deflected by the spacecraft potential and therefore cannot be observed at all by those anodes.

The actuator walk effects highlight why it is important to select the maximum count rate of the signatures from a few energy sweeps before and after the centre of the signature during the process of determining normalised counts. Similarly, it demonstrates why the *other anode subtraction* electron background subtraction method is the only option for some flybys – *gap subtraction* cannot be used when there is no gap between signatures because this would subtract negative ion counts.

5.3. Negative ion mass groups

Now that we have a form of normalised negative ion counts, we can investigate the mass spectra. We will start by looking at T16; during this flyby the highest ion masses ever seen with CAPS-ELS were observed. It was also discussed by Coates et al. (2007b). T16 took place on 22 July 2006 with CA at 00:25:13 UT at a polar latitude of 85.2 degrees. It is one of a number of flybys with a very low CA altitude of 950km (see Table 3 to compare CA altitudes of other flybys); the only flyby that occurred at a lower CA altitude was T70 at 880 km however no negative ions were detected because CAPS did not point in the ram direction due to mission planning constraints. A spectrogram of the T16 negative ion signature can be seen in Figure 51. T16 is another example of a flyby where the spacecraft was rotating around CA as described in section 5.1.5. Therefore the signatures are seen in four anodes as shown in the spectrogram. The first signature is visible in anodes 5 and 6 at 00:21:35 UT and the last signature is visible in anodes 3 and 4 at 00:29:20 UT. The highest mass signature is the tallest in the spectrogram, at 00:25:55 UT. We show a

mass spectrum of this signature from anode 4 in Figure 52. All of the following mass spectra use the normalised counts described in section 5.2.

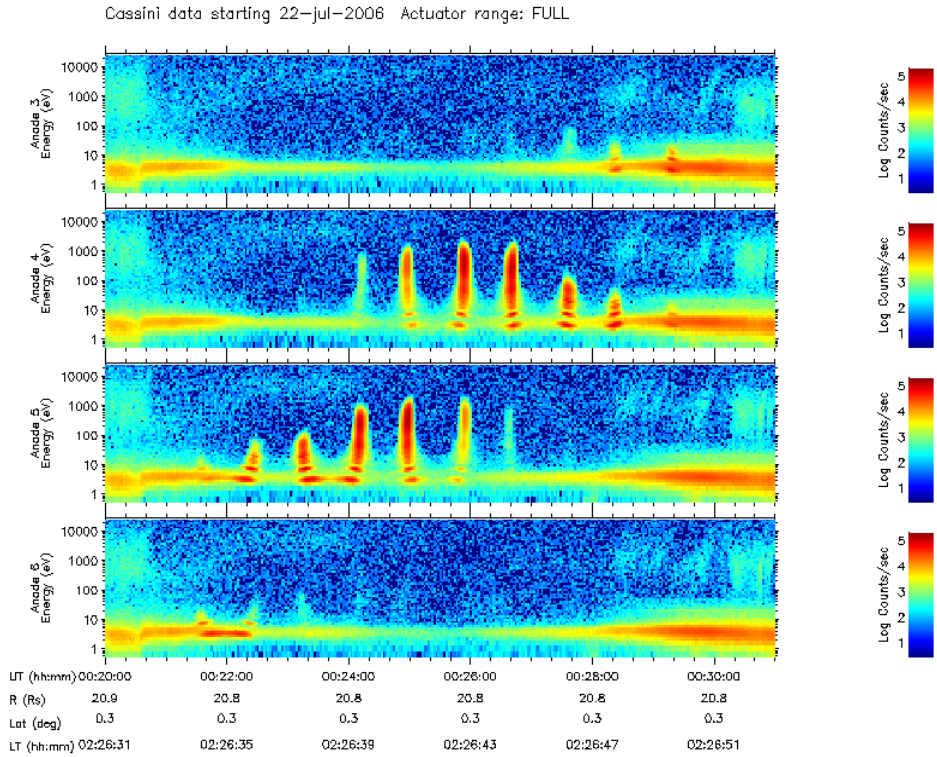

Figure 51: T16 CAPS-ELS spectrograms. Negative ion signatures are visible in all anodes (3-6) shown which is due to a spacecraft rotation. The highest mass negative ion signature is the tallest signature at 00:25:55 UT in anode 4. The corresponding mass spectrum is shown in Figure 52.

In this spectrum (Figure 52), the first two lowest mass peaks are narrow and can be found at 22 amu/q and 45 amu/q as marked in the figure. The next two peaks are less prominent but still narrow, at 67 amu/q and 108 amu/q. We then find a bump at 169 amu/q, followed by a broader peak at 269 amu/q. There are two further peaks at 1494 amu/q and 2795 amu/q making up one very broad peak which shows the highest counts of this signature.

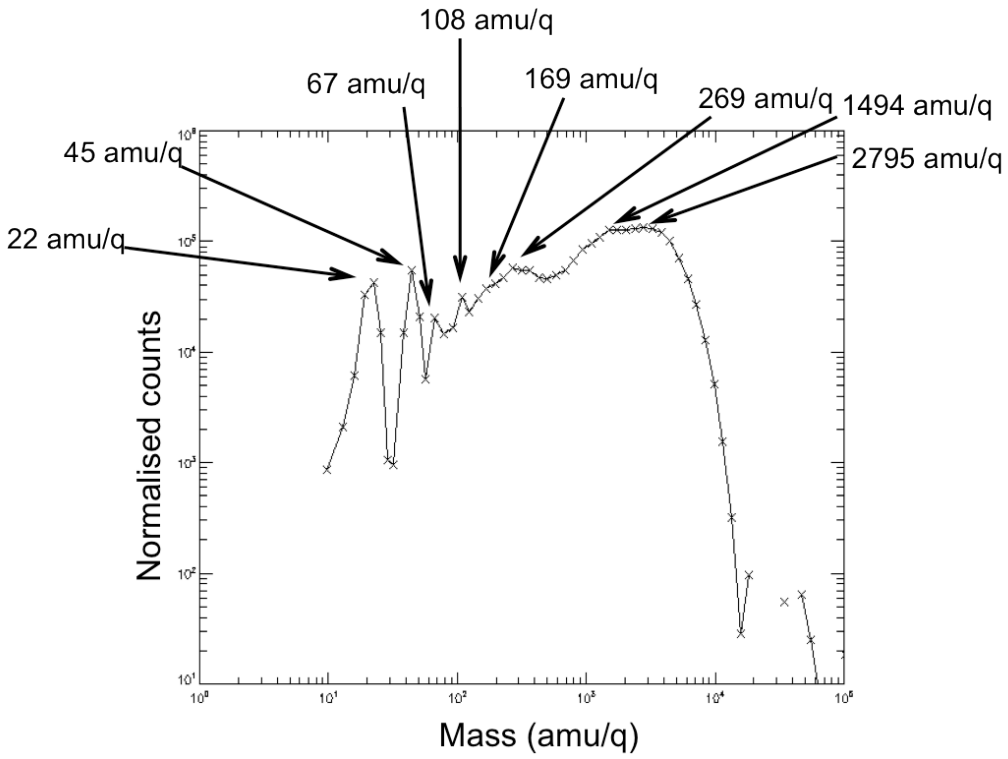

Figure 52: T16 mass spectrum. This is the highest mass negative ion signature observed with CAPS-ELS to date. The spectrum is a timeslice of the tallest negative ion signature in the T16 spectrogram (Figure 51) at 00:25:55 UT.

With the exception of the broad highest mass peak, the mass peaks of most other flybys have similar values. Coates et al. (2007b) stated six mass ranges into which most peaks could be grouped. These six “mass groups” are shown in Table 4. We have since determined slightly different boundaries for these mass groups in order to ensure each peak or prominent bump, such as in the T16 mass spectrum, gets placed in a separate group. The new boundaries are slightly narrower and a seventh group has been added. They are also shown in Table 4.

	Mass range (amu/q)	
Mass group	Coates et al. (2007b)	This study
1	10-30	12-30
2	30-50	30-55
3	50-80	55-95
4	80-110	95-130
5	110-200	130-190
6	200+	190-625
7		625+

Table 4: Negative ion mass groups. The central column shows the mass groups from Coates et al. (2007b), The right hand column shows the new mass groups.

The negative ion analysis in this study is based on these new seven mass groups. The eight peaks described in the T16 spectrum each fall into one of the new mass groups each. The only exceptions are the two highest mass peaks which both fall into the highest mass group (7) because T16 is one of only very few flybys with a peak at a mass as high as 2795 amu. As we shall see later in this section, group 7 is only sometimes present during other encounters, and it is not as prominent most of the time. When present, the group 7 peak is often a bump that extends the broad peak of group 6.

We will now take a closer look at T40 negative ion signatures to show an example of a case where mass group 7 is not as prominent. In the spectrogram in Figure 53 we again see higher masses closer to CA i.e. at lower altitudes. The negative ion signatures can be seen in anodes 4 and 5, the two central anodes closest to the ram direction. Negative ion traces can also be seen in anodes 3 and 6 at intermediate energies (around 100 eV) as shown in Figure 53. Figure 54 shows two mass spectra of the signatures marked ‘2’ and ’4’ in the spectrogram (Figure 53). The top panel is the mass spectrum of the second signature from the left (at 21:28:00 UT) and the bottom panel the fourth signature from the left (at 21:29:40 UT). The lower to intermediate mass peaks can be seen well in the mass spectrum of signature 2 at

23, 45, 83, 111, 152 and 242 amu/q. Each of these fit into a separate mass group (1-6). These groups are also visible to some extent in the spectrogram in signature 4. In signature 4 clear peaks in mass groups 1-4 can be seen in the spectrum, in addition to a broad group 6 peak centred at 524 amu/q. This broad peak is likely to hide the group 5 peak due to its broad width and higher count rate. It may also be hiding part of the group 7 peak. A clue to this is the bump at 1564 amu/q. The centre of the group 7 peak may be at a lower mass value. As mentioned in the previous paragraph, group 7 traces are often visible as bumps like this in other flybys, instead of seeing a fully developed, broad peak as shown in the T16 spectrum above.

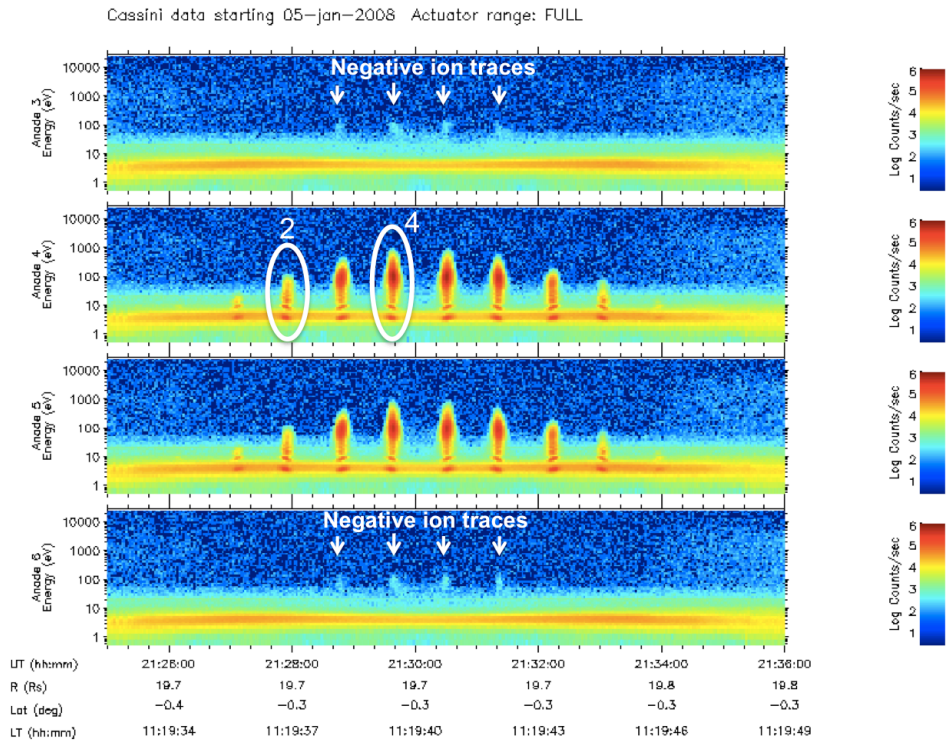

Figure 53: T40 CAPS-ELS spectrograms. Clear negative ion signatures can be observed in anodes 4 and 5 (central panels). Mass spectra of the second and fourth signature from the left (marked '2' and'4') are shown in Figure 54. In anodes 3 and 6 negative ion traces are visible as shown.

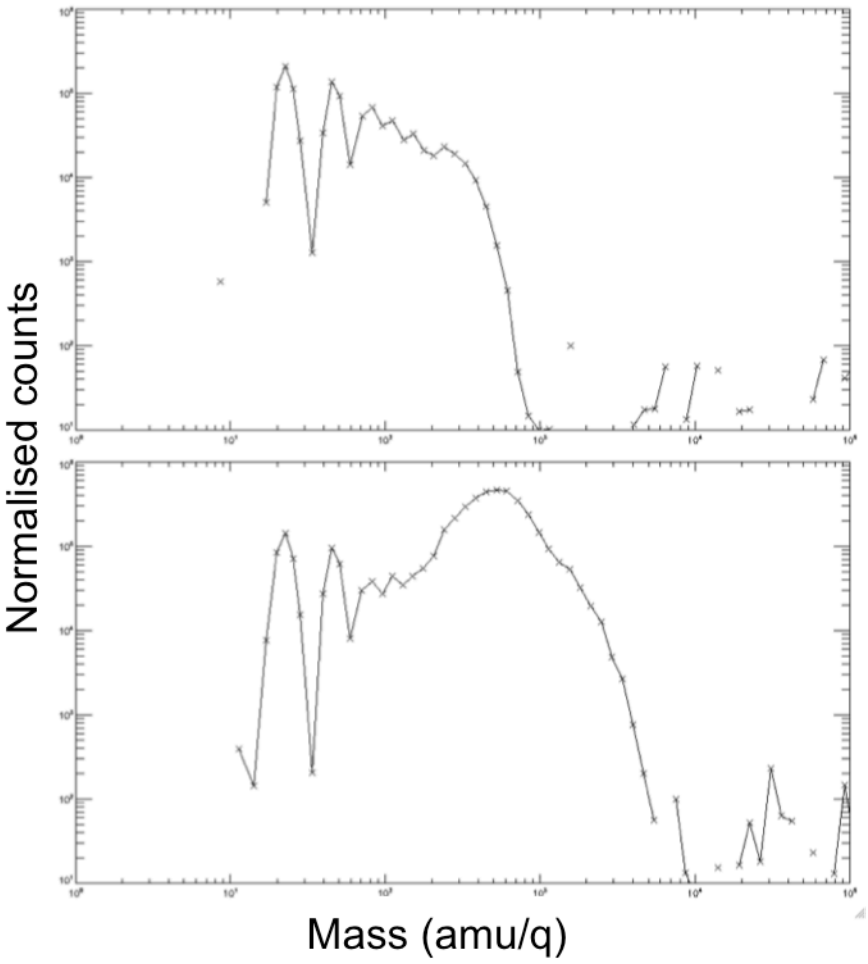

Figure 54: T40 mass spectra. Top panel: Mass spectrum of the second negative ion signature from the left shown in Figure 53 (marked '2') at 21:28:00 UT.Bottom panel: Mass spectrum of the fourth negative ion signature form the left marked '4') at 21:29:40 UT.

Some possible candidate species for the mass groups were shown in Table 2. In the next section we also discuss candidates for the lower mass groups in more detail. The mass group structures are discussed further in section 5.7.3 where we study their evolution during T57. This was a flyby where the actuator was fixed in the ram direction which meant that a continuous set of negative ion data is available without any gaps.

5.4. Analysis of the low mass groups by Vuitton et al. (2009)

Vuitton et al. (2009) presented the first chemical model of Titan's upper atmosphere to include negative ions. They compared the model results with CAPS-ELS data in order to identify some of the negative ions. In this section we summarise the study which includes an introduction to some chemical reactions relevant to the analysis of the results in later sections.

The model is an ionospheric chemistry model that solves the continuity equation in one dimension in the altitude range 700 km to 1200 km. Local chemical equilibrium is assumed. A detailed description of the model can be found in Vuitton et al. (2007) in which the processes controlling the positive ion formation in Titan's ionosphere at the abundances observed with the INMS instrument were modelled. The model was also used to study the ion-neutral chemical processes controlling the formation of the observed benzene in Vuitton et al. (2008).

The model results of Vuitton et al. (2009) show a total negative ion density peak at 1050 km where it reaches approximately 1 cm^{-3}. This only makes up around 1/1000 of the total positive ion density. The density peaks for individual ion species are between 800 km and 1100 km. The most abundant ion at 1000 km is CN^- (m/q = 26) with a density of 1 cm^{-3} followed by C_3N^- (m/q = 50) with 0.2 cm^{-3}. Below 850 km, C_5N^- (m/q = 74) becomes the most prominent ion. Here, C_4H^- and C_6H^-, which are created from polyyine species, also have significant relative densities. The peak density of C_4H^- is near 1050 km. All other ions have negligible densities at all altitudes considered in the model. These results are shown in Figure 55 and Figure 56.

Figure 55: Negative ion density altitude plot from the results of the ionospheric chemistry model by Vuitton et al. (2009). The results also include those shown in Figure 56.

Figure 56: Negative ion density altitude plot from the results of the ionospheric chemistry model by Vuitton et al. (2009). The results also include those shown in Figure 55.

The two low mass peaks in the CAPS-ELS spectrum are centred at 22±4 amu/q and 44±8 amu/q and, considering the model densities described above, were therefore identified as being due to CN^- and C_3N^-. The third small peak at 82±14 amu/q is also consistent with C_5N^-. It is suggested that at altitudes above 1100 km, C_4H^- also contributes to the second negative ion peak due to its density relative to C_3N^- that increases with altitude, as can be seen in the figures.

We now summarise the different types of reactions involved in the above results as discussed by Vuitton et al., 2009. The results can be understood in terms of the production and destruction rates of CN^- and C_3N^- shown in Figure 57 and Figure 58, respectively.

Figure 57: Important production and destruction rates versus altitude for CN^- as calculated by the Vuitton et al. (2009) ionospheric chemistry model.

Figure 58: Important production and destruction rates versus altitude for C_3N^- as calculated by the Vuitton et al. (2009) ionospheric chemistry model.

Radiative electron attachment is a photochemical reaction in which thermal electrons are attached to atoms or radicals:

$X + e_T^- \rightarrow (X^-)^* \rightarrow X^- + h\nu$

Example:

$CN + e_T^- \rightarrow CN^- + h\nu$

Dissociative electron attachment is a photochemical reaction that is usually endothermic because the energy of the bond broken is larger than the electron affinity. Therefore, a suprathermal electron is required to overcome this difference:

$AB + e_S^- \rightarrow A- + B$

Example:

$C_4H_2 + e_S^- \rightarrow C_4H^- + H$

Electron attachment seems to be the major negative ion production mechanism at higher altitudes. Dissociative electron attachment on HCN and HC_3N produces most of the CN^-:

$HCN + e^- \rightarrow CN^- + H$

$HC_3N + e^- \rightarrow CN^- + C_2H \rightarrow C_3N^- + H$

The second part of the latter reaction produces C_3N^-. It only adds a small amount to the C_3N^- abundance though because the cross section for the second part is lower than for the first part. On the other hand, radiative electron attachment is negligible for the production of CN^-, however, it does play a significant role in the production of C_3N^- at altitudes below approximately 1050 km.

Proton transfer reactions are chemical reactions where a strong acid donates a proton to a strong base:

$AH + B^- \rightarrow BH + A^-$

Proton transfer reactions of ions with more acidic neutrals are important at lower altitudes. Transfer from HCN to C_xH^- in the reaction

$C_xH^- + HCN \rightarrow CN^- + C_xH_2$

is important in adding CN^- to the atmosphere below 800 km.
The proton transfer reaction

$$CN^- + HC_3N \rightarrow HCN + C_3N^-$$

is the dominant production reaction for C_3N^- but also a destruction reaction for CN^-.
Proton transfer on C_xH^- in

$$C_xH^- + HC_3N \rightarrow C_3N^- + C_2H_2$$

also contributes to the C_3N^- abundance below 800 km. Proton transfer from HC_5N to C_3N^- is not included in the model because of a lack of information about this reaction.

In **ion-neutral associative detachment** the negative ion attaches to a neutral, producing a metastable species that then ejects the electron:

$$A^- + B^{\bullet} \rightarrow (AB^-)^* \rightarrow AB + e^-$$

The neutral is usually a radical because associative detachment reactions only occur when the electron detachment energy is less than the energy of the bond produced. This is usually the case with reactions involving radicals because they produce stable molecules. The two most common radicals in Titan's upper atmosphere are H and CH_3. Ion-neutral dissociative detachment reactions through the radicals H and CH_3 are the main destruction processes generally for negative ions in this model and also specifically for CN^- and C_3N^-.

In **ion-ion recombination**, a positive and a negative ion combine to form a neutral molecule:

$X^+ + Y^- + Z \rightarrow [XY] + Z$

Destruction of negative ions due to ion-ion recombination with positive ions becomes progressively more important at higher altitudes. It is still relatively small for CN^- at high altitudes and negligible at lower altitudes. It is also largely negligible for C_3N^- especially at low altitudes.

If a negative ion absorbs a photon of sufficient energy, **photo-detachment** can occur:

$A^- + h\nu \rightarrow A + e^-$

Photo-detachment also becomes more important at higher altitudes. Loss of CN^- due the reaction

$CN^- + h\nu \rightarrow CN + e^-$

is negligible in the lower atmosphere and small in the upper atmosphere. The loss of C_3N^- due to

$C_3N^- + h\nu \rightarrow C_3N + e^-$

is negligible at all considered altitudes because C_3N^- has a high electron affinity.

Ion-pair formation is another photochemical reaction. Photo-ionisation can produce a positive/negative ion pair:

$AB + h\nu \rightarrow A^- + B^+$

Ion pair formation reactions such as

$HCN + h\nu \rightarrow CN^- + H^+$

are mostly negligible in these simulation results. Ion-pair formation from HC_3N producing C_3N^- is not included in the model because not enough information about this reaction was available but it is believed that this reaction would not contribute significantly to the production of C_3N^-.

Table 5 shows the EA of some species discussed above. Some of these reactions will be discussed further in section 5.8 in order to analyse the results of sections 5.5, 5.6 and 5.7. The following three sections make up the main results of this chapter.

Table 5: Electron affinities (EA) of some species in Titan's upper atmosphere (Vuitton et al., 2009).

5.5. Maximum Mass study

5.5.1. Introduction

In order to see where the maximum masses of the negative ions occur, we determined the measured maximum mass during each flyby for each negative ion signature. Coates et al. (2009) show results of the first 23 negative ion encounters

(highlighted in table Table 3) investigating maximum mass trends with altitude, latitude and solar zenith angle (SZA).

To find the maximum mass for a negative ion signature, a count level was defined to determine where at the high mass end of the spectrum the maximum mass has a sufficient number of counts. This count level was then used consistently for all flybys and all anodes.

Now, three years after the Coates et al. (2009) study was published, we have a larger number of flybys (34, compared to 23 in Coates et al. (2009)) which includes 339 negative ion signatures, and we have updated and improved the results. The normalised counts used in this updated study are more accurate because we used an improved background subtraction method called *other anode subtraction* (described in section 5.2.4). In Coates et al. (2009) a subtraction method was used based on subtracting the background between the signatures (*gap subtraction*, as described in section 5.2.4).

5.5.2. Latitude and SZA sampling

In this subsection we present data demonstrating the latitude and SZA coverage which is shown in Figure 59 and Figure 60, respectively. The total number of samples is the number of negative ion signatures from the 34 encounters where clear negative ions were observed. This means every flyby where the spacecraft was at a low enough altitude to detect negative ions (below 1400 km) and the actuator pointed in the ram direction.

The histograms in Figure 59 and Figure 60 show the number of samples in 15° latitude and SZA bins. The total number of samples included in the yellow histogram is 336. These are all samples that were observed below an altitude of

1368 km. We show three additional histograms which include all samples observed below the altitudes indicated. The blue, green and red histograms have a total number of 313, 251 and 216 samples, respectively.

The reason we are showing samples at different altitude ranges is as follows: In this section and the next section (5.6) we look for trends in the largest masses and densities. As we shall see shortly, the larger masses and higher densities are observed at lower altitudes. When we look for latitude and SZA trends, we consider all 339 samples. However, some of these samples will be low in mass or density only because they were observed at a higher altitude, and not because they are found at a particular latitude or SZA. In order to expose this bias, we show the coverage below certain altitudes as indicated in the figures. The specific altitude of 1368 km was chosen because it is the *reference altitude* for the lowest mass group. We refer to the *reference altitude* as the maximum altitude at which negative ions were detected above a certain minimum density. This is described in detail in section 5.6.2.

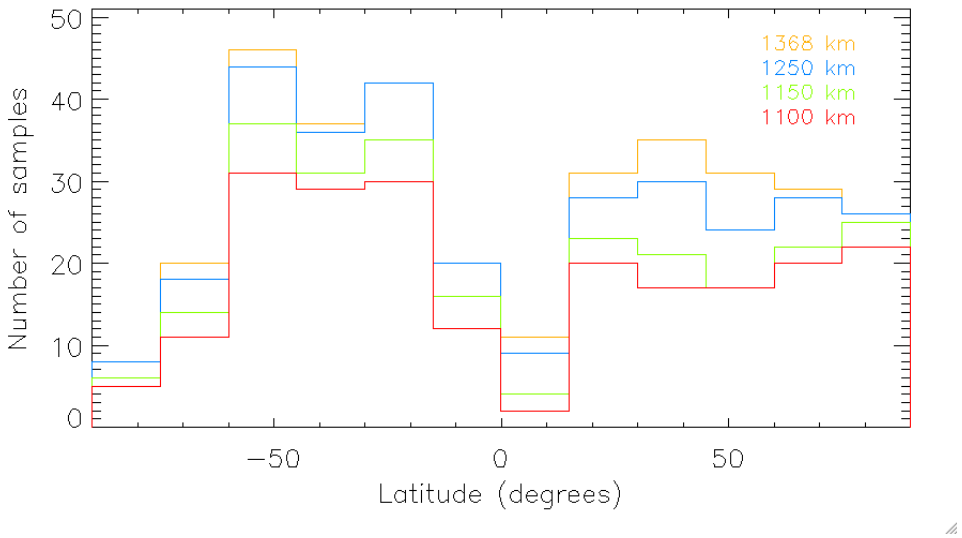

Figure 59: Latitude sampling of negative ion signatures. The horizontal axis shows 15° latitude bins. The vertical axis shows the number of samples in each bin. The histograms include all samples that were observed below the indicated altitude.

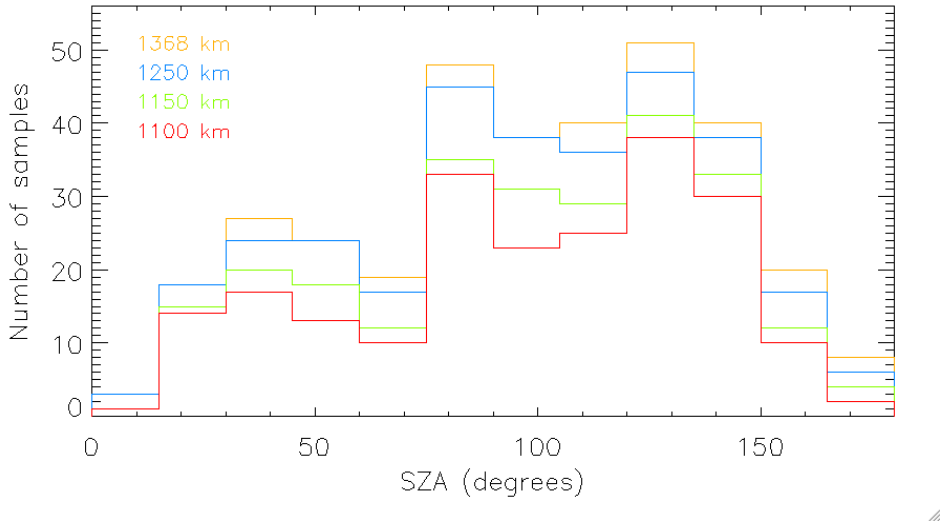

Figure 60: SZA sampling of negative ion signatures. The horizontal axis shows 15° SZA bins. The vertical axis shows the number of samples in each bin. The histograms include all samples that were observed below the indicated altitude.

We note that the shape of the different coloured histograms is similar. This is probably due to the following reasons: We generally observe a number of negative ion signatures per flyby; the average is nine (excluding the actuator fixed flybys described in section 5.7). For example, we have 12 samples from T26 (spectrogram shown in Figure 44). Samples from the same flyby have similar ephemeris data because they occurred close together. When we restrict the samples to those observed below a certain altitude, the number of samples per flyby is often simply reduced, and hence the number of samples in e.g. that latitude region. For example in the T26 spectrogram, only the central six signatures are observed below an altitude of 1100 km (red histograms in Figure 59 and Figure 60).

5.5.3. Maximum mass – altitude trends

Figure 61 and Figure 62 show the altitude trends from Coates et al. 2009 and from the updated current study, respectively. The results are all in mass/q. Altitude is on the vertical axis and the maximum mass on the horizontal axis. The lowest Titan flybys occurred at a CA altitude of 950 km with one exception. The T70 flyby had a

CA altitude of 880 km, however, CAPS did not point in the ram direction due to mission planning constraints, hence no negative ions were observed with CAPS-ELS. Coates et al. (2009) described the result as demonstrating a clear preference for larger mass at lower altitude. Figure 62 clearly confirms these results.

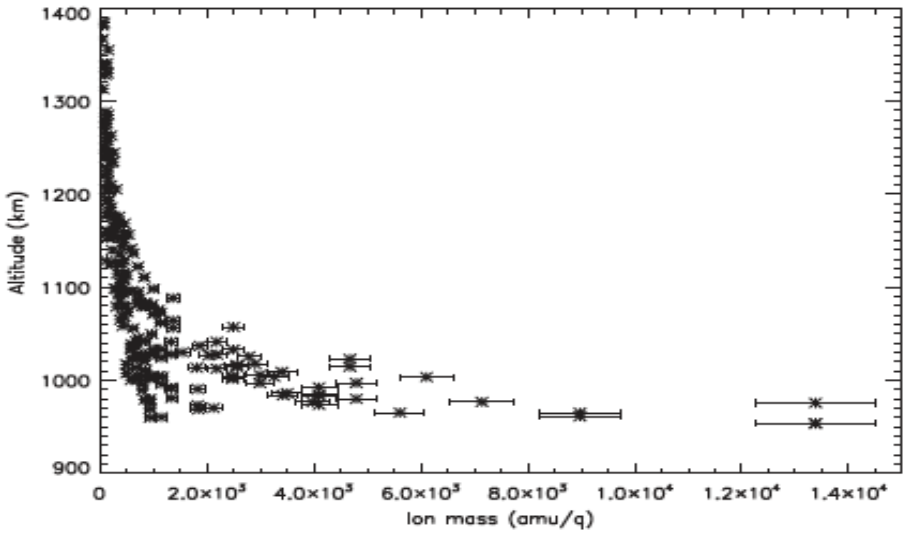

Figure 61: Coates et al. (2009) maximum negative ion mass – altitude plot using data from 23 negative ion flybys.

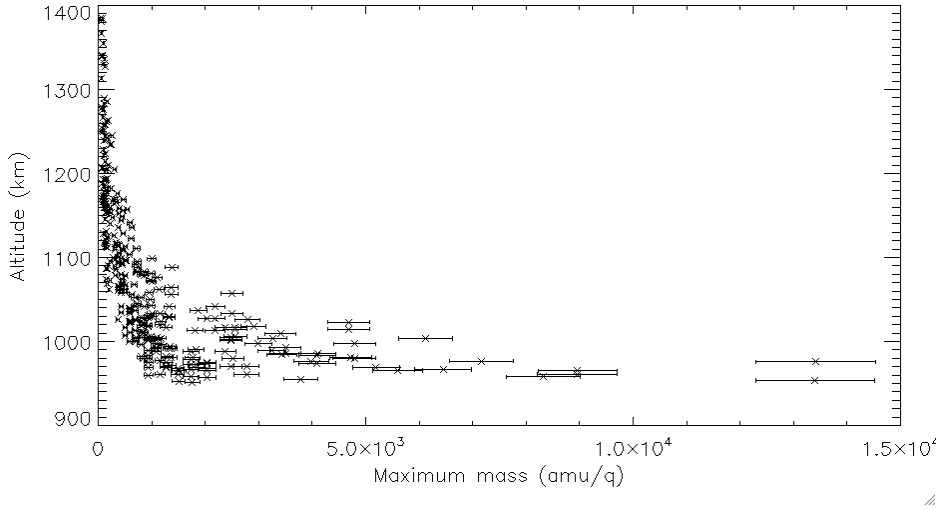

Figure 62: Updated maximum negative ion mass - altitude plot using data from 34 negative ion flybys.

5.5.4. Maximum mass – latitude trends

Figure 63 shows the Coates et al. (2009) latitude - maximum negative ion mass plot. The result was described as a trend for larger mass at higher latitude in both the Northern and Southern hemisphere. Figure 64 shows the new results and demonstrates that this trend does not necessarily apply because there are also higher masses at lower latitudes e.g. at 40°S. The lack of higher masses in the equator region is possibly due to low sampling (see Figure 59).

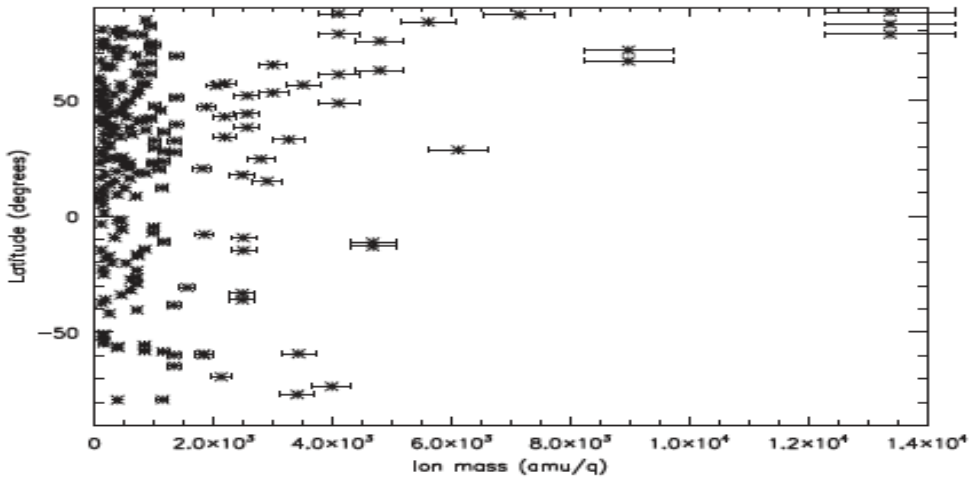

Figure 63: Coates et al. (2009) maximum negative ion mass – latitude plot using data from 23 flybys.

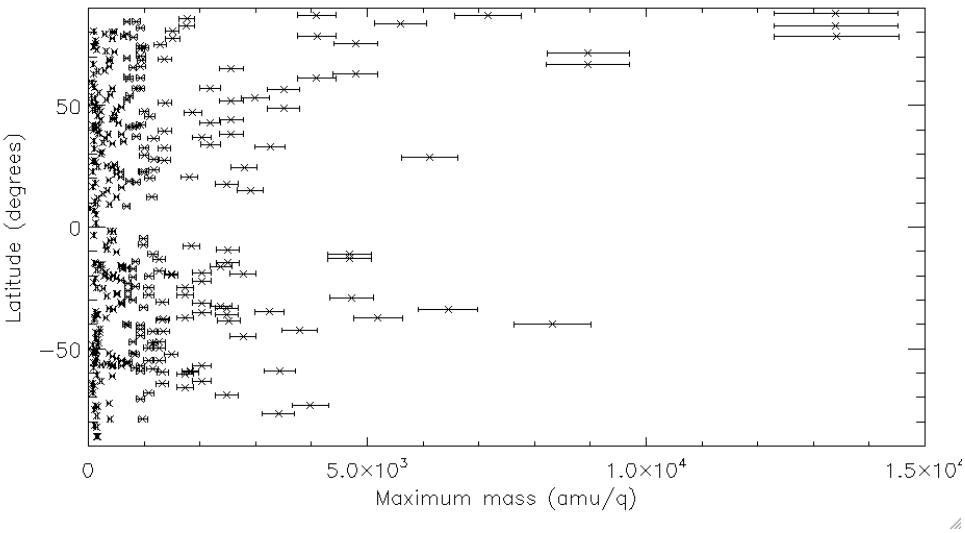

Figure 64: Updated maximum negative ion mass – latitude plot using data from 34 flybys.

5.5.5. Maximum mass – SZA trends

The solar zenith angle (SZA) is the angle between the line pointing to the Sun and the local zenith, as shown in Figure 65. A SZA of 0° means the sun is at the local zenith i.e. directly above you. On the surface, the terminator is at a SZA of 90°. However, at higher altitudes the terminator moves to higher SZAs: At typical Cassini flyby altitudes, e.g. at 1000 km, the terminator is at a SZA of approximately 135° as shown in Figure 65. Therefore only the parts of the atmosphere beyond 135° are in in complete darkness (due to Titan's solid body's shadow). Parts of the atmosphere close to 135°, e.g. the region 90° to 135°, are exposed to reduced solar flux due to a longer path length through the atmosphere.

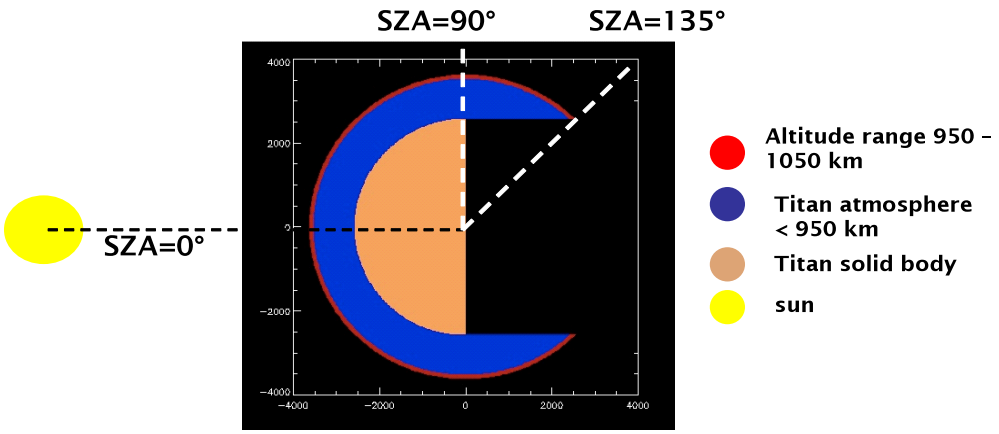

Figure 65: Solar Zenith Angle (SZA) at Titan.

Figure 66 shows the Coates et al. (2009) SZA - maximum mass plot. Coates et al. (2009) described the result as showing a trend for the highest mass to be observed near the terminator (90° SZA). Figure 67 shows the new SZA results. The picture has generally not changed much and the highest masses are observed near the surface terminator at 90°. However, the highest masses are always observed at SZAs higher

than the surface terminator (90° SZA). There also appears to be a lack of high masses around 90° SZA. This will be discussed further below. In addition, sampling is low near 0° and 180° SZAs (see Figure 60). More future flybys will show whether higher masses can be found in these regions.

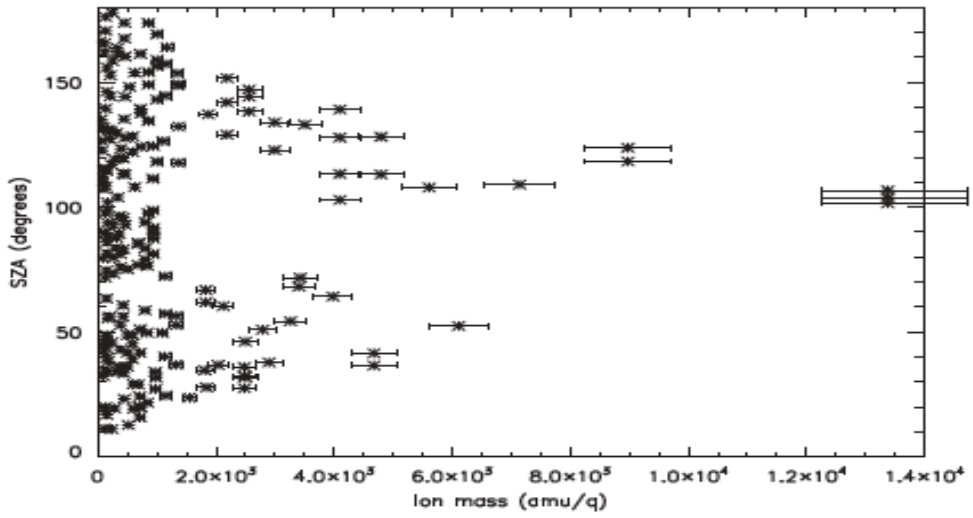

Figure 66: Coates et al. (2009) maximum negative ion mass – SZA plot using data from 23 flybys.

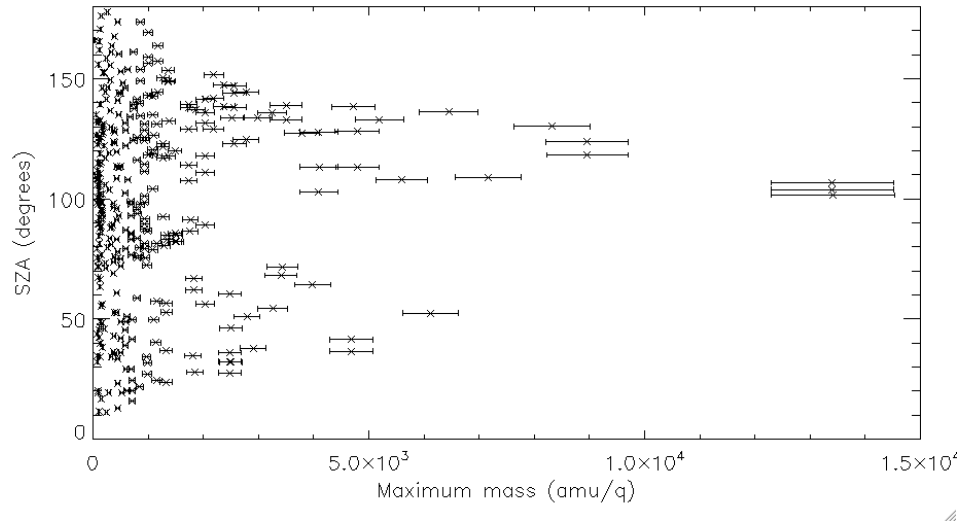

Figure 67: Updated maximum negative ion mass – SZA plot using data from 34 flybys.

5.5.6. Discussion

In this section we will discuss general aspects of this study and also compare the results to those of Coates et al. (2009). We will discuss the scientific implications of the results further in section 5.8, where we also have density trend information and can discuss both where the maximum masses appear and where different masses are abundant or rare.

The altitude trend is by far the clearest and there is little doubt about the fact that highest masses are observed at the lowest altitudes. This can also be observed to some extent in spectrograms in which we see the 'longest' spike-shaped signatures near CA and shorter ones further away from CA i.e. at higher altitudes. In addition, in the maximum mass – altitude plots we can see that at the lowest altitudes there is a lower limit for the lowest mass data points: Even the lowest mass data points have a higher mass than the highest masses observed at higher altitude. These lowest data points at low altitude are of course still the maximum mass during that observed signature and therefore this can be treated like a lower limit for the maximum mass observed. As can be seen from the mass spectra in section 5.3 and also later in section 5.7.3, there is a large range of masses during most signatures, especially the low altitude encounters.

When comparing the latitude results of Coates et al. (2009) (Figure 63) and this updated study (Figure 64), the additional higher mass data points at mid-latitudes show that a larger number of samples is important. It is still possible that the very largest masses are only formed at high latitudes near the poles, however as the

new results show, high masses can also be observed at mid latitudes. The polar T16 encounter is the only flyby with exceptionally high masses and the three very high data points at high Northern latitude shown in both figures are all T16 signatures.

The highest mass observed is 13,800 amu/q which was detected during T16. A spectrum of this flyby signature can be seen in section 5.3 (Figure 52). We note that the results of this study are in mass per charge (see section 5.1.2) which means that the actual masses shown may be much larger if the ions are not singly but multiply charged as discussed by e.g. Coates et al. (2007b). The maximum T16 masses are much higher than any other flyby, which makes the T16 conditions unusual. Why did we observe such high masses only during T16? T16 is a polar flyby. Conditions at the pole are likely to contribute. However we do have data from other polar and near-polar flybys, which did not show such very high masses. A clue to why we observe such high masses here may lie in the seasons (also see Figure 7). There were three other negative ion Titan flybys (i.e. flybys where CAPS pointed in the ram direction and was low enough to detect negative ions) that took place above 80° northern or southern latitudes. T32 took place at 87°N in June 2007 and showed a high maximum mass (5,600 amu/q), but not by far as high as during T16. The other flybys are T64 and T65, whose minimum altitudes occurred at 83°N in December 2009 and at 82°S in January 2010, respectively. This is very close to equinox in August 2009. The highest mass observed during T64 and T65 was 1,760 amu/q and 170 amu/q, respectively. T16 took place in July 2006 and is therefore the closest polar flyby in time to the 2002 northern winter solstice. Therefore maybe the long-term effect of more limited winter solar radiation allows the ions to grow larger without high destruction rates due to photochemical reactions such as photo detachment. It will be of great interest to see whether this theory holds when we get closer to the southern winter solstice in 2017. Currently there is one planned flyby in the south polar region: T116 on 1 February 2016 at 84°S. However, unfortunately the current planned CA altitude is 1400 km which is not low enough to detect negative ions.

Coates et al. (2009) stated that high masses are found near the terminator. High masses can be observed in the range between 100° and 140°, however there appears to be a lack of high masses in the region between 80° and 100° SZAs. This trend is probably real and unrelated to sampling issues (Figure 60). Even though there is a slightly lower number of samples at 90° SZA compared to neighbouring bins, the number is even lower in e.g. the 50° SZA bin where a number of higher masses are observed. We will discuss this further and compare the results with the density trends in section 5.6.

This maximum mass study is most useful for the altitude trend study as we can see the clearest maximum mass trend.

5.6. Density trends

5.6.1. Introduction

The normalised counts calculated as described in section 5.2 can be used to calculate the negative ion number density. To do this we assume that the counts represent a current of ions in the ram direction:

$$n = \frac{C}{A_{eff}\varepsilon v}$$

Equation 29

where n is the negative ion density, C is the count rate, A_{eff} is the effective area of the instrument estimated from aperture size and ground calibration data, ε is the estimated MCP efficiency for ions at this bias voltage and v is the spacecraft velocity (Coates et al., (2007b). We note that the product is the negative ion number

density. When we refer to negative ion densities in this work we imply the number density unless otherwise stated.

It is difficult to estimate the MCP efficiency because negative ions were not expected at Cassini flyby altitudes, therefore the CAPS-ELS MCPs were never tested or calibrated using negative ions on the ground. Fraser (2002 investigated ion detection efficiencies of MCPs. Figure 68 from this study shows some MCP efficiency data from calculations. The numbers near the curves indicate the ion energies in keV. If we assume that the trends continue in the same or similar pattern at the lower energies observed by CAPS-ELS, we can see that the value of 0.05 for the MCP efficiency used in Coates et al. (2007b) seems adequate, however the uncertainty due to this poorly understood value for CAPS-ELS is high, which is discussed in section 5.8.2.

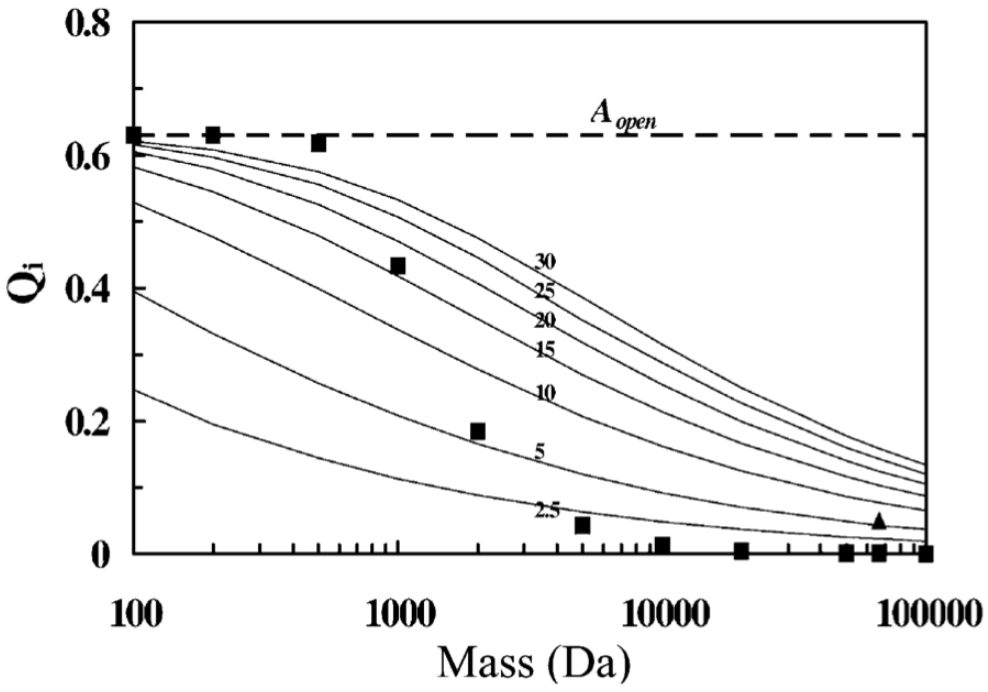

Figure 68: Microchannel plate (MCP) efficiency curves from Fraser (2002). The numbers near the curves indicate the ion energy for that curve in keV.

We now have a set of densities in each energy (i.e. mass) bin from which we can calculate total densities. We can also add up the mass bins to make up the mass

groups described in section 5.3. To keep the addition of electron background low, the upper boundary of mass group 7, the highest mass group, is determined individually for each flyby.

5.6.2. The negative ion 'reference density'

The largest random uncertainty in determining the densities is the subtraction of the background electrons. The following study was performed in order to determine the uncertainty due to background subtraction. This uncertainty was then used to define the *reference density.* These reference density values are used to describe the minimum density for a certain mass group that can be used scientifically in the density trend study and are not at risk of being a background subtraction artefact.

The method used to establish an estimate of the background subtraction uncertainty is similar to the actual background subtraction method described in section 5.2.4. However, instead of subtracting counts of an anode without a negative ion signature from an anode with the strongest negative ion signature, one background anode is subtracted from another background anode. We refer to one anode as the *background anode* and the other as the *pseudo-negative ion anode*, because we treat the latter as if it were an anode with negative ions from which we subtract an electron background. If the background was exactly the same in all anodes, the result would be zero. Therefore the difference between the results and zero can be an estimate of how large the uncertainty due to the different anodes and the electron anisotropies is. Uncertainties due to inter-anode scaling contribute to this uncertainty too. The data is used to calculate a product in the same way that the negative ion densities were calculated. One can think of the product as an artificial or pseudo "negative ion density" for each mass group that describes the uncertainty due to the sources described above. Therefore the results

have the same format, i.e. there are readings for each pseudo negative ion signature for all seven mass groups for each negative ion flyby. This results in a total of 339 readings for each mass group. Even though anodes without any negative ion signatures are used, the time stamps of the signatures were kept the same as when the ions were observed.

Results of this study are shown in Table 6. The right hand column shows the maximum difference between the pseudo density and zero from results using the method described above. We use the modulus of this maximum discrepancy to define the *reference density* mentioned above for each mass group. Negative ion densities above this value are considered 'real' and can be used for scientific analysis. We estimate a 90% confidence that negative ion samples above the reference density are due to negative ions. These density values may not, however, be purely due to negative ions. A fraction of the converted normalised counts may still be due to background electrons or inter anode scaling uncertainties. The uncertainty due to these sources is given by the value of the reference density, and therefore the percentage uncertainty due to these sources decreases with increasing density. These and other negative ion density uncertainties are further discussed in section 5.8.2

Mass group	Maximum discrepancy from 0
1	-5.34
2	-3.46
3	-0.49
4	-0.26
5	-0.1
6	-0.16
7	-0.23
Total	-9.74

Table 6: Results from a study investigating the uncertainty related to electron background subtraction and inter anode scaling (see text for details). The modulus of each value in the right hand column is the reference density for each mass group.

Densities below the reference density will still be shown as part of the density trend study results in the next sections but may not be real, especially very low values. They will, however, give an idea of the general sampling in addition to Figure 59 and Figure 60.

One might wonder why all the values are negative. The reason is not fully understood. However, it appears to be unrelated to the anode order. A test was performed where the anode roles were reversed i.e. the subtraction anode was swapped with the anode that was being used as the artificial negative ion anode. The results were the same except that all were positive.

The default artificial ion anode was generally one of lower numerical order than the background anode, e.g. anode 3 (artificial density) normalised counts were subtracted from anode 2 (background anode) normalised counts. As described in section 5.2.2, all anodes are scaled with respect to anode 5, one of the two central anodes. The scaling is done using the geometric factors of the anodes. Each geometric factor has an uncertainty of 10% (Lewis et al., 2010). Hence the reason as to why we get these consistent negative values may be due to geometric factor uncertainties. Nevertheless, the reference density is an estimate of the uncertainties due to exactly this inter anode scaling, and also due to the electron background. The sign of the reference density is not relevant. It may be worth investigating whether there really is such an anode bias in the future. If a systematic uncertainty can be found it may be possible to eliminate or at least reduce the effect.

The reference density is important in determining which negative ion samples are real. This is, for example, significant when determining the highest altitude at which a mass group is observed, which is shown in the right hand column of Table 7.

5.6.3. Density altitude trends

In this section we look at how the negative ion densities vary with altitude. Figure 69 - Figure 76 show the total density versus altitude and the individual mass group density versus altitude plots of the 34 encounters which make up 339 negative ion signatures and hence 339 data points per mass group. There is generally a range of densities between the lowest density and the highest density at a given altitude. Therefore for each mass group we can describe the behaviour of the highest and lowest densities observed at a given altitude, and the density range at a given altitude. We can also determine the altitude at which the maximum density is observed and the maximum altitude at which negative ions were detected above the reference density. We refer to the latter altitude as the *reference altitude*. This information is summarised in Table 7.

Mass group	Mass range	Maximum density	Flyby (of max density)	Altitude (at max density)	SZA (at max density)	Reference altitude
	amu/q	cm^{-3}		km	°	km
Group1	12-30	112	T43	1050	34.1	1367
Group2	30-55	92	T41	1030	23.7	1355
Group3	55-95	36	T43	1018	37.8	1336
Group4	95-130	43	T41	1030	23.7	1285
Group5	130-190	83	T29	1017	138.2	1263
Group6	190-625	593	T23	1004	52.4	1205
Group7	625+	331	T30	980	128.1	1098
Total		948	T23	1004	52.4	1355

Table 7: Summary of negative ion density altitude and SZA trends. The first column from the left indicates the negative ion mass group. The second column shows the maximum observed density for each mass group. The third, fourth and fifth columns show during which flyby, at which altitude and which SZA the maximum density reported in the second column was observed. The sixth column shows the reference altitude which is the maximum altitude at which negative ions are observed above the reference density.

Total densities

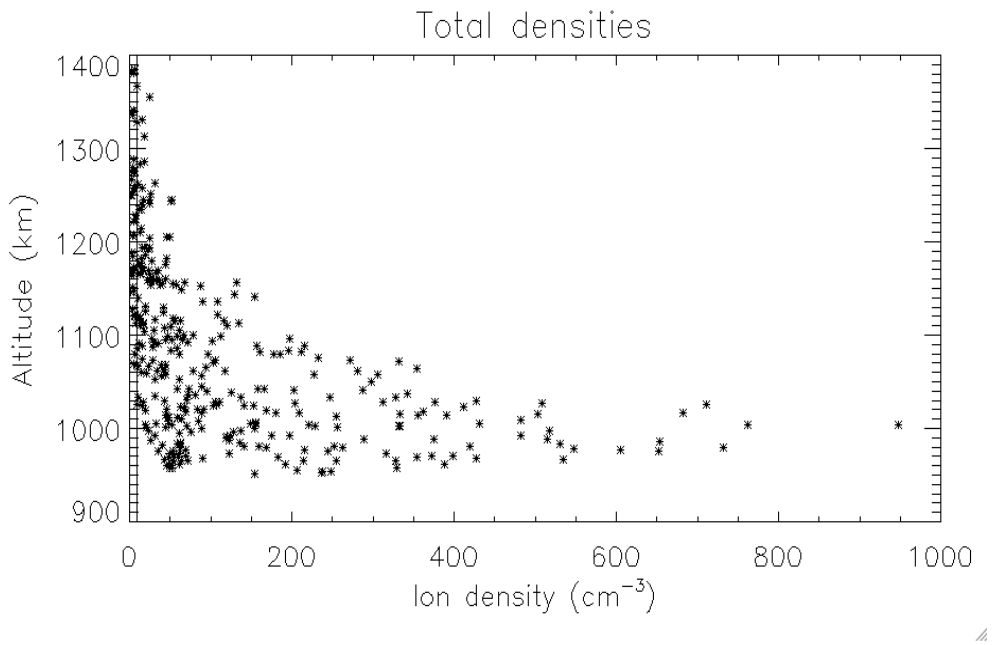

Figure 69: Negative ion density versus altitude: Total densities.

Figure 69 shows a plot of total negative ion densities vs. altitude. The vertical line at 10 cm^{-3} indicates the reference density. The maximum density observed is 948 cm^{-3}. The associated signature was observed during T23 at an altitude of 1004 km, a latitude of 29° and at a SZA of 52°. Below this altitude the highest densities start to decrease with decreasing altitude. The maximum altitude at which densities above the reference density were observed is 1355 km. There is generally a range of densities present between the reference density and the highest density at a given altitude. The lowest densities at a given altitude are scattered around the reference density for most altitudes. One noticeable exception is at altitudes below approximately 1000 km where the lowest densities increase to values up to about 50 cm^{-3}.

Group 1

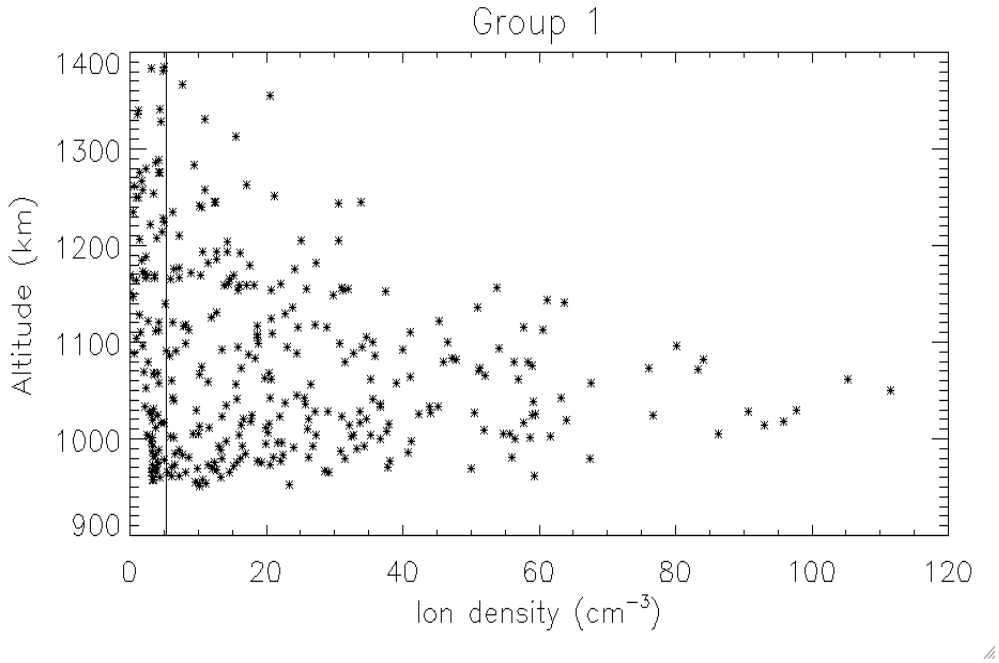

Figure 70: Negative ion density versus altitude: Group 1 (12 – 30 amu/q) .

The reference altitude for group 1 is 1367 km. Highest densities at a given altitude increase with decreasing altitude from 1367 km to the maximum density at 1050 km. The highest densities then decrease with decreasing altitude below this maximum.

Group 2

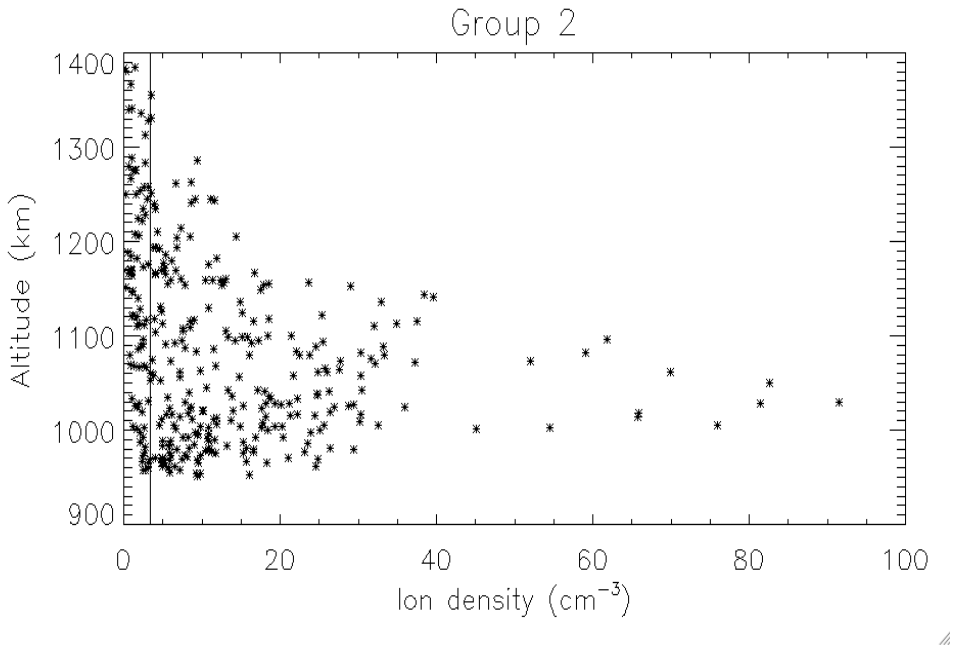

Figure 71: Negative ion density versus altitude: Group 2 (30 – 55 amu/q) .

Highest densities increase slowly with decreasing altitude in the range 1355 km (reference altitude) to 1160 km. They then increase more rapidly until the density maximum at 1030 km. The increase is particularly rapid at altitudes 1160 km to 1140 km. Below the maximum density the highest densities decrease with decreasing altitude. Densities as high as 45 cm^{-3} and above are only detected in the altitude range 1000 – 1100 km. The drop in highest densities at low altitudes (below 1000 km) is more pronounced than in group 1.

Group 3

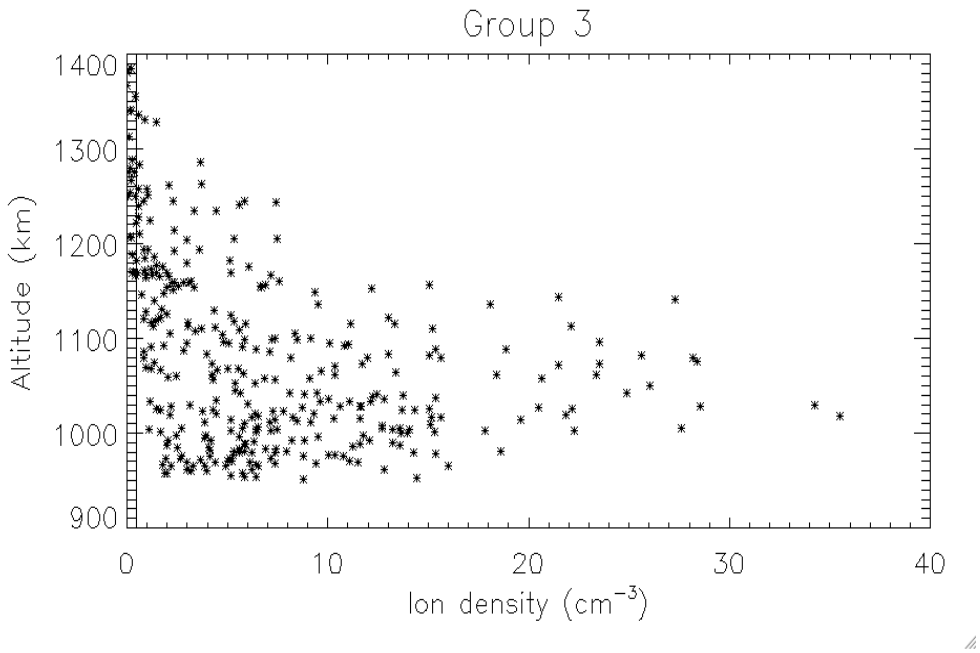

Figure 72: Negative ion density versus altitude: Group 3 (55 – 95 amu/q) .

Highest densities increase with decreasing altitude in the range 1336 km (reference altitude) – 1160 km after which they stay approximately constant in the altitude range 1160 – 1000 km with the exception of two higher data points around 1025 km. Highest densities below 1000 km then decrease slowly with decreasing altitude. At altitudes below 1160 km all densities are above the reference density.

Group 4

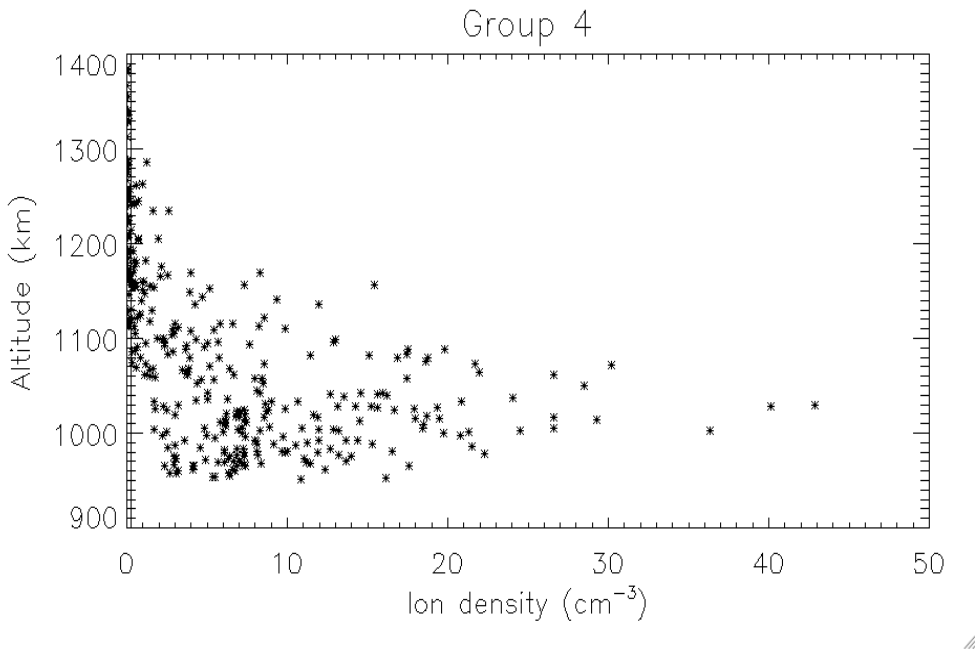

Figure 73: Negative ion density versus altitude: Group 4 (95 - 130 amu/q) .

Highest densities increase in the altitude range 1285 km (reference altitude) – 1030 km and then decrease with decreasing altitude. All densities are well above the reference density at altitudes below 1060 km.

Group 5

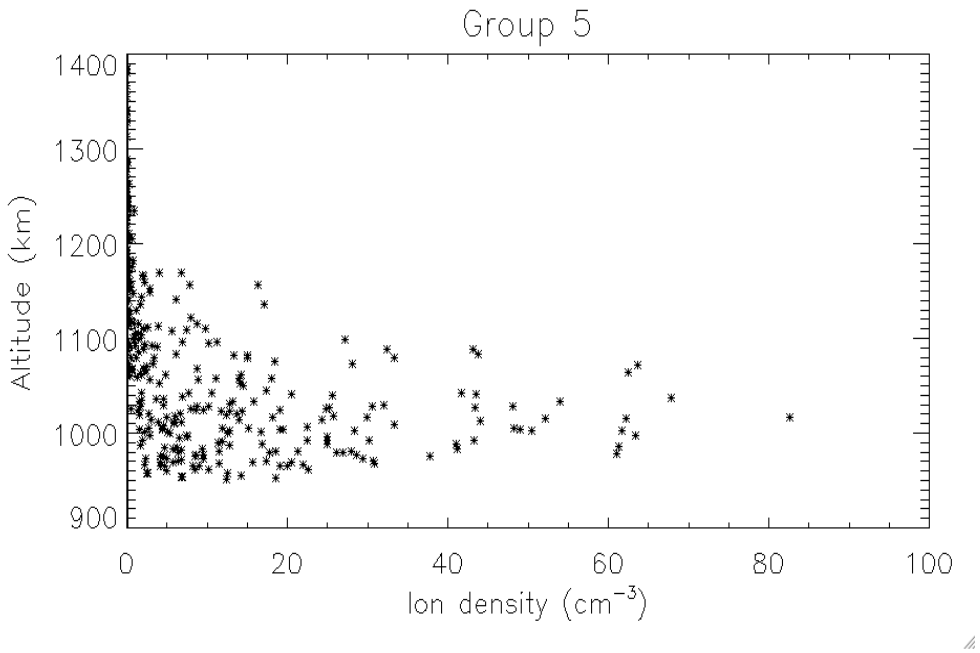

Figure 74: Negative ion density versus altitude: Group 5 (130 – 190 amu/q).

Although present above the reference density from an altitude of 1263 km, group 5 densities only start to get higher than 1 cm^{-3} below 1169 km. From here the highest densities increase until the highest measured density at 1017 km is reached. They then decrease with decreasing altitude. All densities are above the reference density below 1050 km.

Group 6

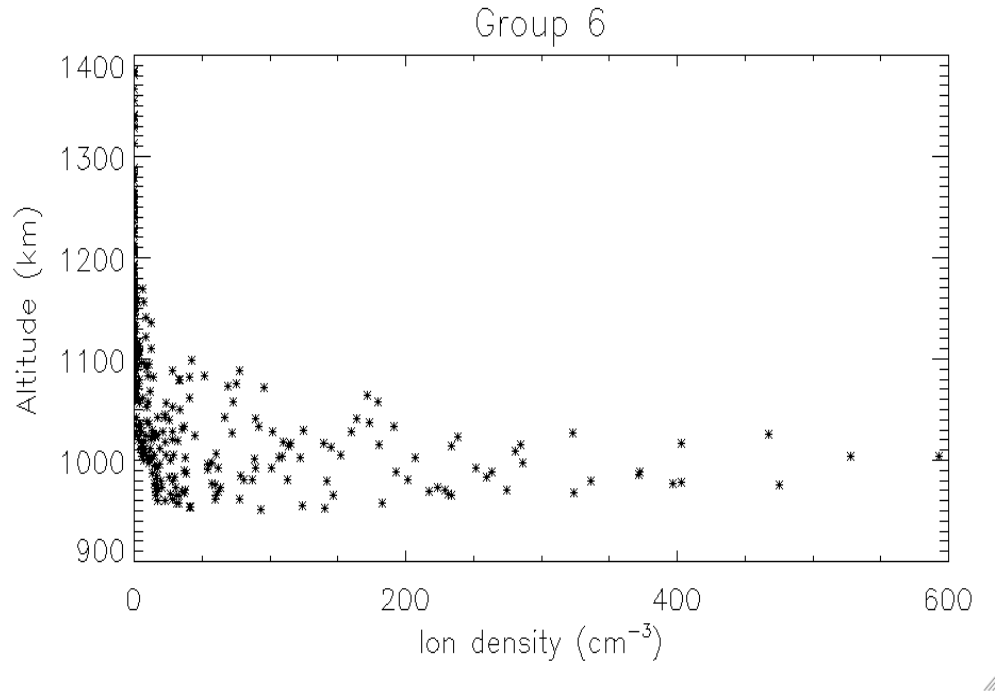

Figure 75: Negative ion density versus altitude: Group 6 (190 - 625 amu/q) .

Densities are present from a reference altitude of 1205 km. Highest densities increase slowly below this altitude and then more rapidly from 1100 km, reaching a maximum at 1003.5 km. Highest densities decrease below this maximum. Even the lowest densities are greater than 10 cm^{-3} at altitudes below 1000 km which is also well above the reference density.

Group 7

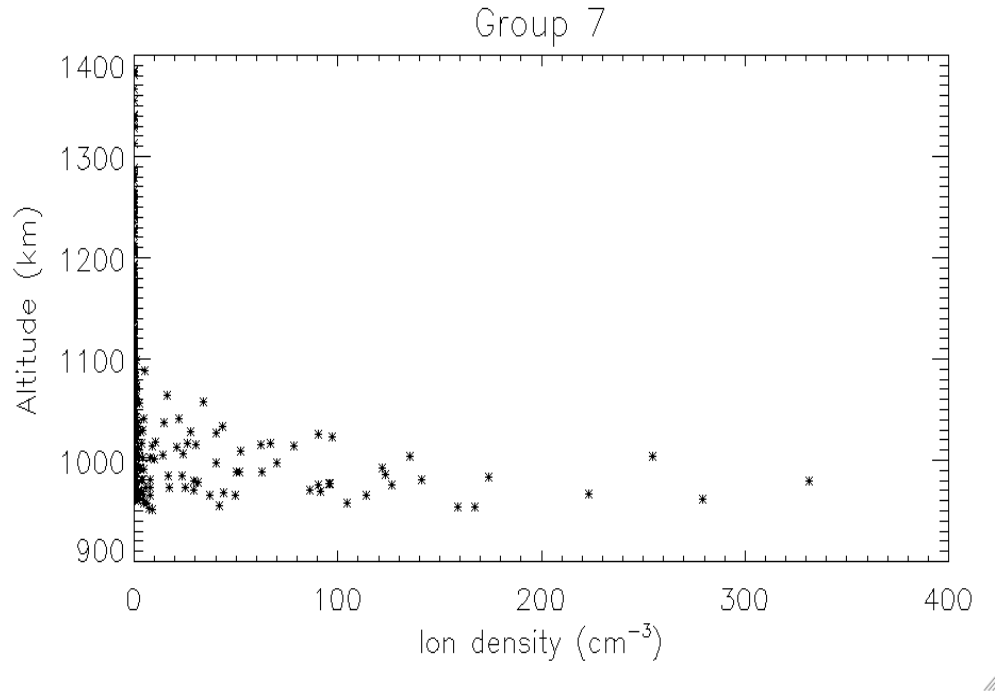

Figure 76: Negative ion density versus altitude: Group 7 (625+ amu/q) .

The reference density is 1098 km and the highest densities increase rapidly from here until the maximum density at 980 km. The fact that the maximum density is present at such a low altitude also means that the highest densities are still relatively high near the altitude observation limit (950 km).

In summary, the density altitude plots demonstrate that the highest densities are found at low altitudes. It should be noted that generally the range of densities observed also increases at lower altitudes – low densities are still present at low altitudes, too, although in most cases the lowest densities are observed above the reference density at lower altitudes. We also notice from the summary data presented in Table 7 that the reference altitude decreases with increasing mass group.

5.6.4. Density SZA trends

In this section we investigate how the negative ion densities vary with solar zenith angle (SZA). The SZA at Titan was described in more detail in section 5.5.5. Plots of negative ion density versus SZA of the total densities and the individual mass groups are shown in Figure 77 to Figure 84. There are dashed horizontal lines in each figure at the 90° and 135° SZAs. These are the surface terminator and terminator at approximately 1000 km altitude, respectively. The maximum densities for each mass group, and the SZAs at which these are observed, are shown in Table 7. Descriptions of the plots are summarised in the table below the respective plots.

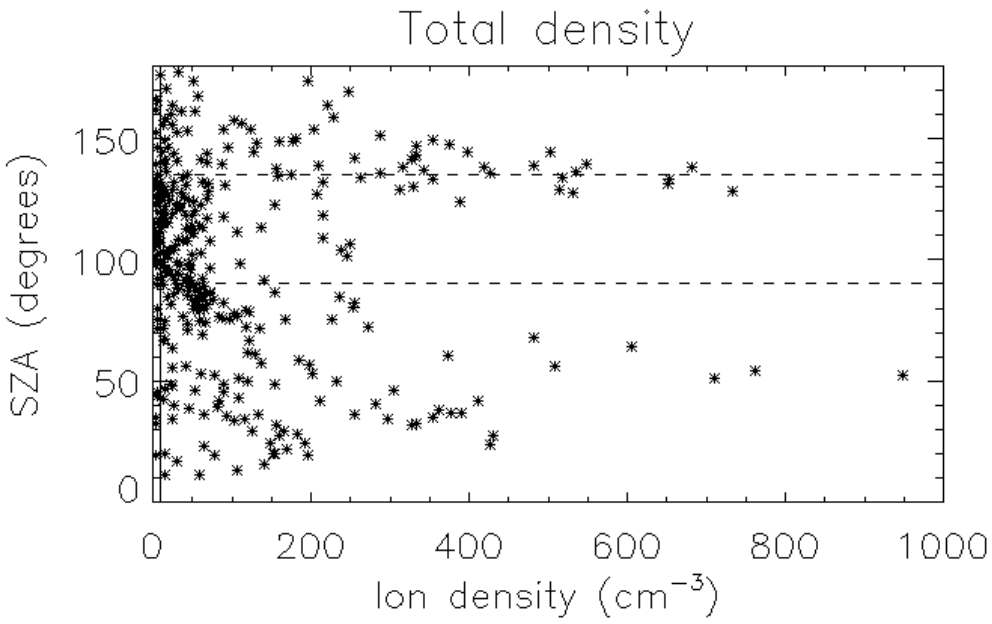

Figure 77: Total negative ion density versus SZA.

SZA (°)	Total observed densities
< 50	Low to intermediate.
50 - 70	Large range, low to high.
70 – 120	Low to low intermediate, mostly low.
120 - 150	Low to high.
>155	Low coverage. Low and low intermediate.

Table 8: Total negative ion density SZA trends summary.

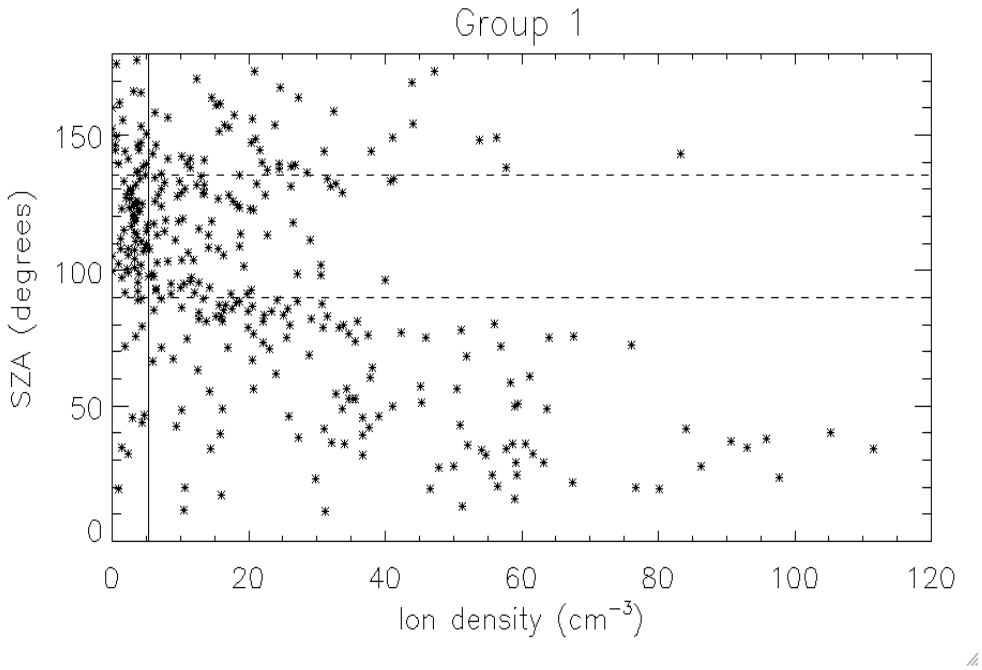

Figure 78: Negative ion density versus SZA: Group 1 (12 – 30 amu/q) densities.

SZA (°)	Group 1 (12 – 30 amu/q): observed densities
< 50	Large range, low to high.
50 - 80	Low to high intermediate.
80 - 90	Low to low intermediate, mostly low intermediate.
90 - 130	Mostly low densities. A considerable number below and around the reference density, plus some in the low intermediate region.
130 - 155	Low to intermediate, plus one high density data point.
> 155	Low coverage. Low to intermediate.

Table 9: Group 1 negative ion density SZA trends summary.

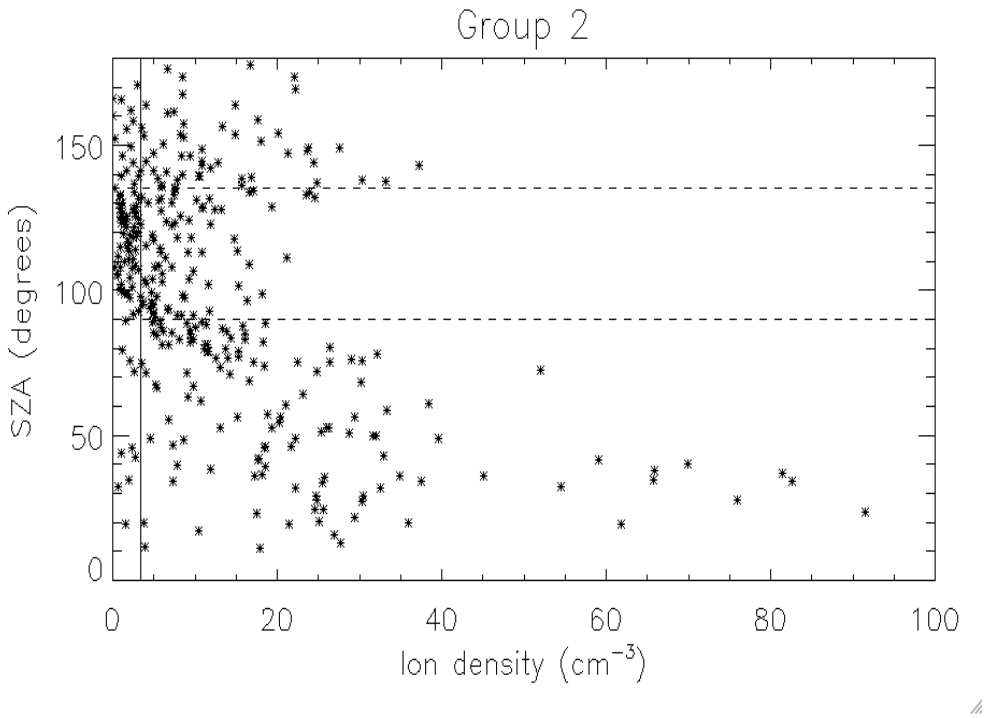

Figure 79: Negative ion density versus SZA: Group 2 (30 – 55 amu/q) densities.

SZA (°)	Group 2 (30 – 55 amu/q): observed densities
< 40	Large range, low to high.
50 - 80	Low to intermediate plus one high intermediate density data point.
80 - 100	Mostly low to low intermediate at around 80°. Densities decrease as 100° is approached.
100 - 130	Low to low intermediate, mostly low around the reference density.
130 - 155	Low to intermediate.
> 155	Low coverage. Low to low intermediate.

Table 10: Group 2 negative ion density SZA trends summary.

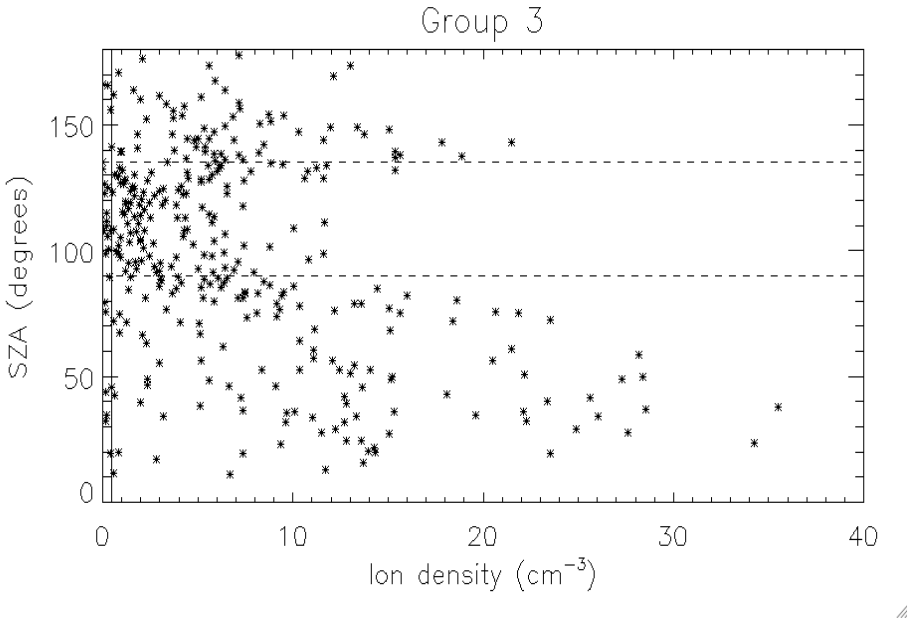

Figure 80: Negative ion density versus SZA: Group 3 (55 - 95 amu/q) densities.

SZA (°)	Group 3 (55 – 95 amu/q): observed densities
< 60	Large range, low to high.
60 - 90	Low to high intermediate.
90 - 130	Low to low intermediate, mostly low.
130 - 150	Low to intermediate.
> 150	Low coverage: Low to low intermediate.

Table 11: Group 3 negative ion density SZA trends summary.

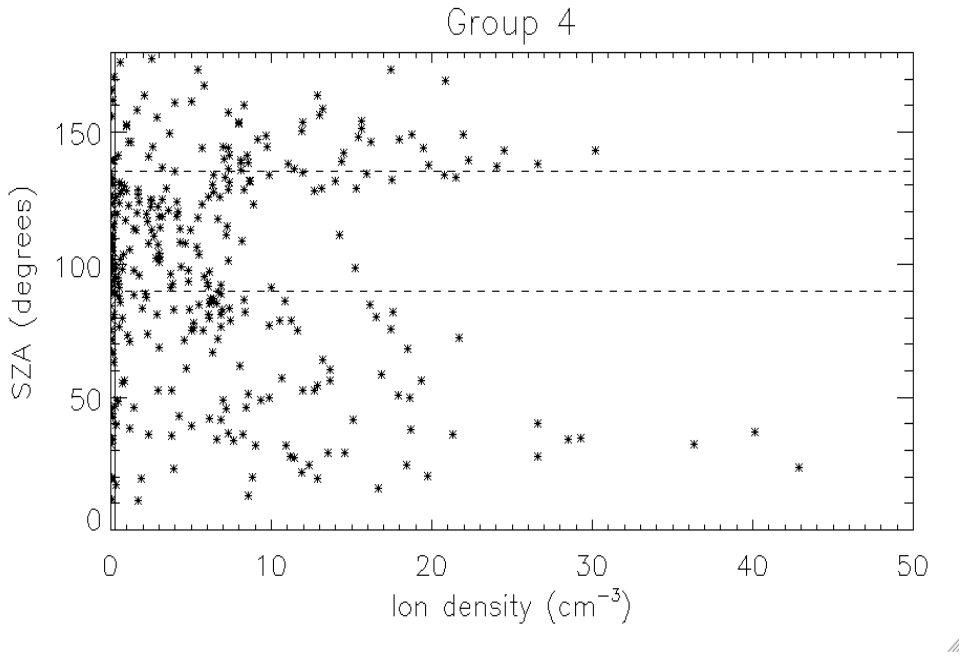

Figure 81: Negative ion density versus SZA: Group 4 (95 - 130 amu/q) densities.

SZA (°)	Group 4 (95 – 130 amu/q): observed densities
< 40	Low to very high.
40 - 70	Low to intermediate.
70 - 90	Low to low intermediate, mostly low.
90 - 125	Mostly low, two data points at intermediate densities.
125 – 150	Low to high intermediate.
> 150	Low coverage. Low to intermediate.

Table 12: Group 4 negative ion density SZA trends summary.

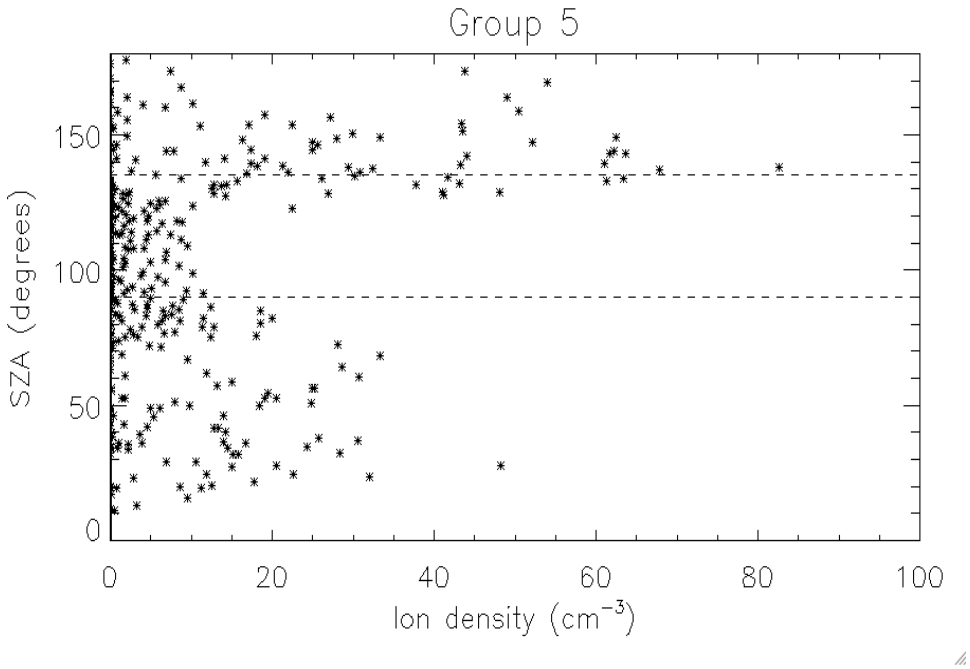

Figure 82: Negative ion density versus SZA: Group 5 (130 – 190 amu/q) densities.

SZA (°)	**Group 5 (130 – 190 amu/q): observed densities**
< 70	Low to intermediate. One high intermediate data point.
70 - 90	Low to low intermediate.
90 - 120	Low.
120 - 160	Large range including very high.
> 160	Low coverage. Some low and some high intermediate.

Table 13: Group 5 negative ion density SZA trends summary.

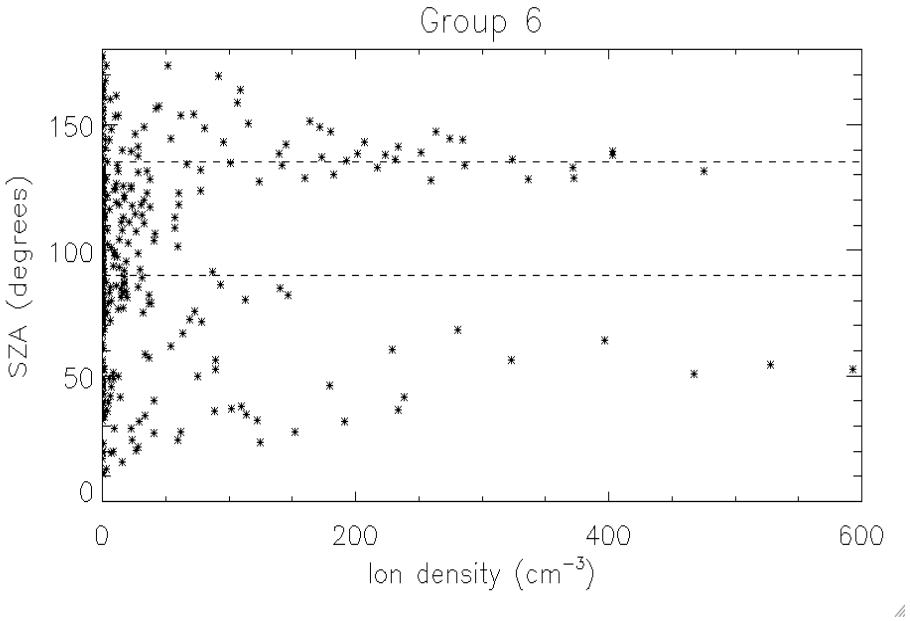

Figure 83: Negative ion density versus SZA: Group 6 (190 – 625 amu/q) densities.

SZA (°)	Group 6 (190 – 625 amu/q): observed densities
< 40	Low to intermediate.
40 - 70	Large range from low to very high.
70 - 100	Low to low intermediate.
100 - 120	Low.
120 – 150	Low to high.
> 150	Low coverage. Low to low intermediate.

Table 14: Group 6 negative ion density SZA trends summary.

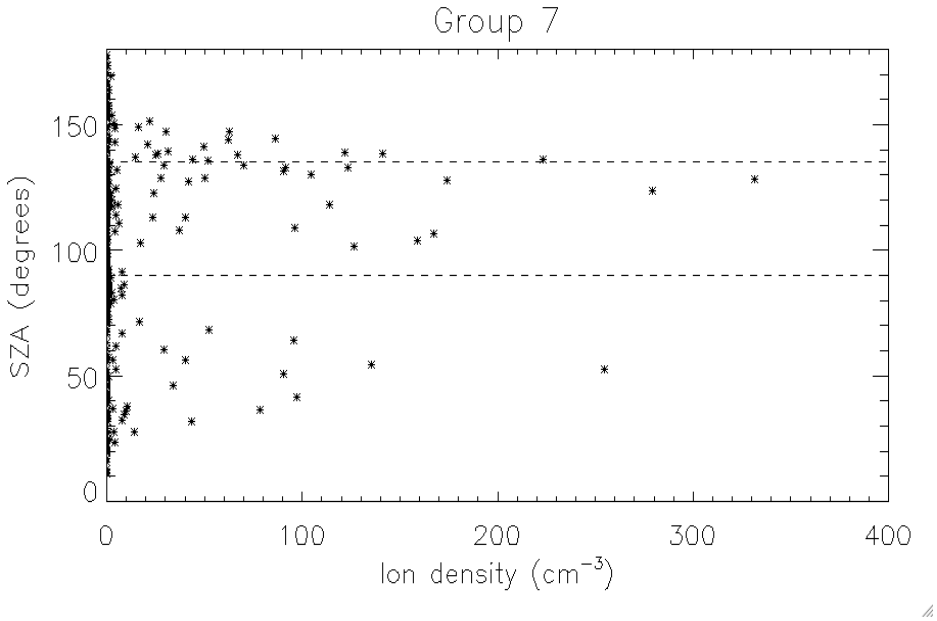

Figure 84: Negative ion density versus SZA: Group 7 (625+ amu/q) densities.

SZA (°)	Group 7: observed densities
< 20	Low coverage. Low.
20 - 75	Low to intermediate, plus one high data point.
75 - 100	Low.
100 - 120	Low to intermediate.
120 – 150	Low to intermediate, plus three higher data points.
> 150	Low coverage. Low.

Table 15: Group 7 negative ion density SZA trends summary.

In summary, groups 1 to 3 seem to share the trend that the highest densities are found on the dayside, predominantly low densities around 100° – 120° SZA, and then a range of low to intermediate or higher densities on the night side (but not as high as on the day side). These trends are still present in group 4 however the day side high densities are only present at SZA < 50**°**. Groups 5 and 7 are the only

groups where the highest densities occur on the night side, although this trend is much more pronounced in group 5. We refer to the presence of predominantly low densities in the region around 100° – 120° (i.e. between the surface terminator at 90° and the actual terminator at 135°) as the *near terminator depression* (NTD). It can also be observed in the higher mass groups 5 – 7 where it is more pronounced than at lower masses. Group 6 has high densities on both the day and night side, which makes the presence of only low densities in the NTD region particularly pronounced. Group 7 also has a strong NTD, however the effect occurs at slightly lower SZAs (75° to 100°).

It is difficult to determine the boundaries of the NTD region precisely from the scatter plots (Figure 78 to Figure 84), however the upper SZA boundary appears to be between 120° and 130° for all mass groups except group 7 (100°). It is therefore close to the terminator, but always at lower SZAs. The lower boundary is found between approximately 90° and 100° for mass groups 1 – 6 and at 75° for mass group 7. We discuss possible reasons to explain the NTD region in section 5.8. Before this, we explore this interesting effect further in section 5.7.4, where we analyse altitude profiles of four flybys that occurred in or near the NTD region.

5.7. Actuator fixed flybys

5.7.1. Introduction

For a number of flybys, the CAPS actuator was fixed in order to obtain continuous ion measurements. During these encounters the actuator is positioned such that the angle between the two central anodes and the ram direction is kept small. As a result, we see a continuous negative ion structure in the spectrograms instead of the spike-like structures observed when the actuator is moving. These fixed

actuator encounters are T55, T56, T57, T58, T59 and T61. Some of the properties of these flybys are similar. For instance, they all occur near the terminator. In this section we analyse the data of T55 – T58. Having access to continuous data, rather than just a handful of measurements, allows for a more detailed analysis.

In this section we use the actuator fixed flyby data to expand on some results in sections 5.3 and 5.6. To introduce the flybys, we will first look at the individual spectrograms of these four selected flybys. We will then investigate T57 in more detail by studying a large set of mass spectra. This is in order to learn more about how negative ion mass spectra are structured and change over short time periods. Finally, we will investigate some combined density profiles of the four flybys in order to discuss the implications compared with the results from the altitude and SZA density trend studies.

5.7.2. T55 – T58

Figure 85 to Figure 88 show spectrograms of flybys T55 - T58. The two central anodes are shown in the two top panels of each figure. In addition, the angle between the ram direction and the anodes is shown in the bottom panel. We can see that during T57, this angle was kept constant throughout the duration of the negative ion observations. As a result, the spectrograms in the two anodes shown are almost exactly the same. This was also the case during T59, which is not analysed here and will be a part of future studies.

The spectrograms in Figure 85 to Figure 88 show 15 minutes of the lowest part of each of the four flybys. We can clearly observe one large, continuous negative ion signature in the centre, marked by the white circles. Most of the mass groups (see section 5.3) are included in the main structure. However, the two lowest mass groups (12-30 amu/q and 30-55 amu/q) can be observed separate from the main

structures. They are the two structures at lower energies that resemble thick, horizontal lines.

The vertical striation structures most prominently visible during T57 around 18:33:30 UT and during T58 around 17:02:30 UT, but also briefly during T56 around 20:01:20 UT in anode 4, are not yet understood but were investigated by Jones (pers. comm., 2009) and are subject to future work. This type of observation is only possible during continuous negative ion observations like these actuator fixed flybys.

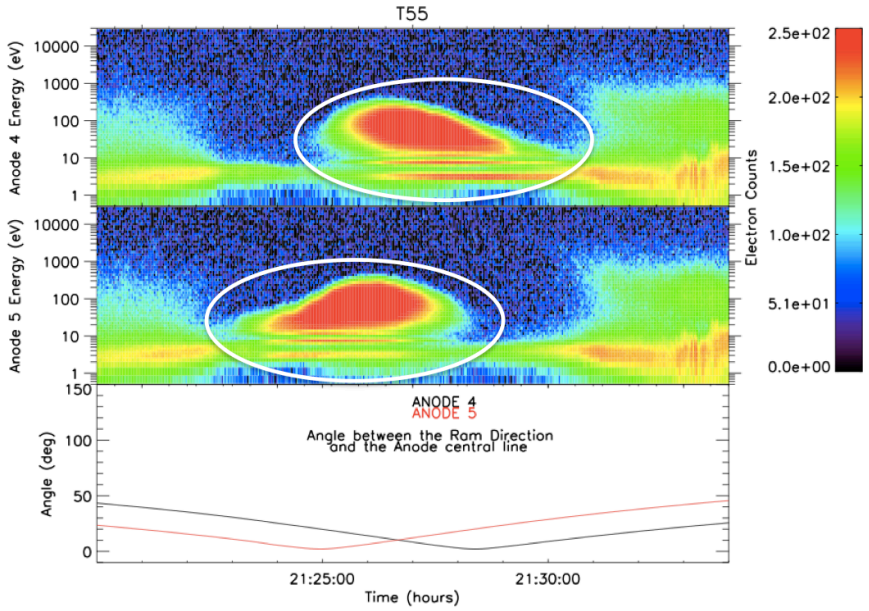

Figure 85. Top two panels: T55 spectrograms of anodes 4 and 5. A continuous, large negative ion structure is visible during this actuator fixed flyby (marked by white circles). Bottom panel: Angle of the two central anodes with respect to the ram direction.

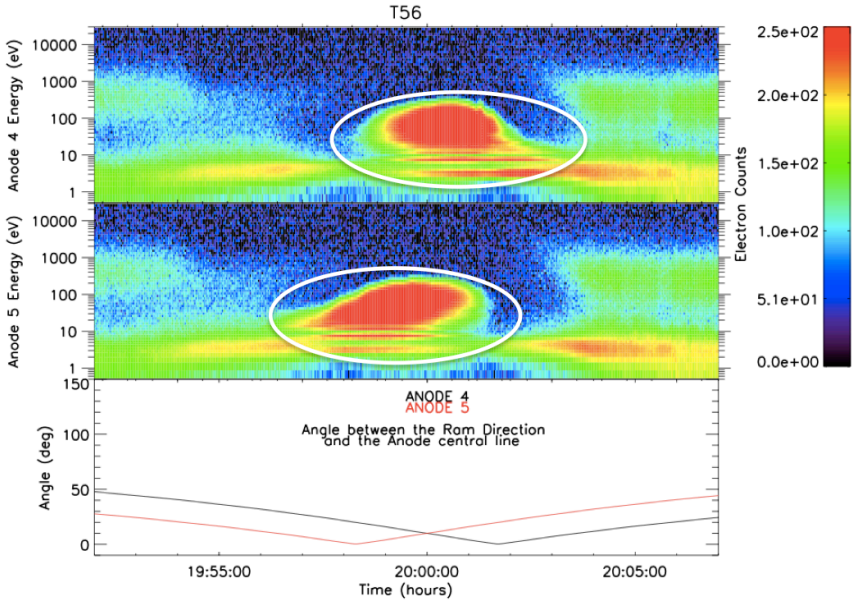

Figure 86. Top two panels: T56 spectrograms of anodes 4 and 5. A continuous, large negative ion structure is visible during this actuator fixed flyby (marked by white circles). Bottom panel: Angle of the two central anodes with respect to the ram direction.

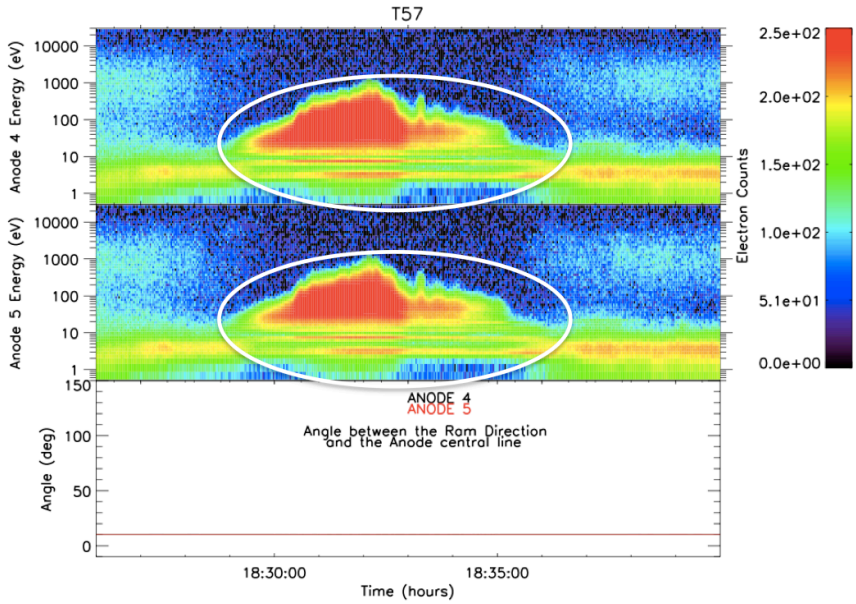

Figure 87. Top two panels: T57 spectrograms of anodes 4 and 5. A continuous, large negative ion structure is visible during this actuator fixed flyby (marked by white circles). Bottom panel: Angle of the two central anodes with respect to the ram direction. This is the only flyby out of the four shown where the ram angle was kept constant.

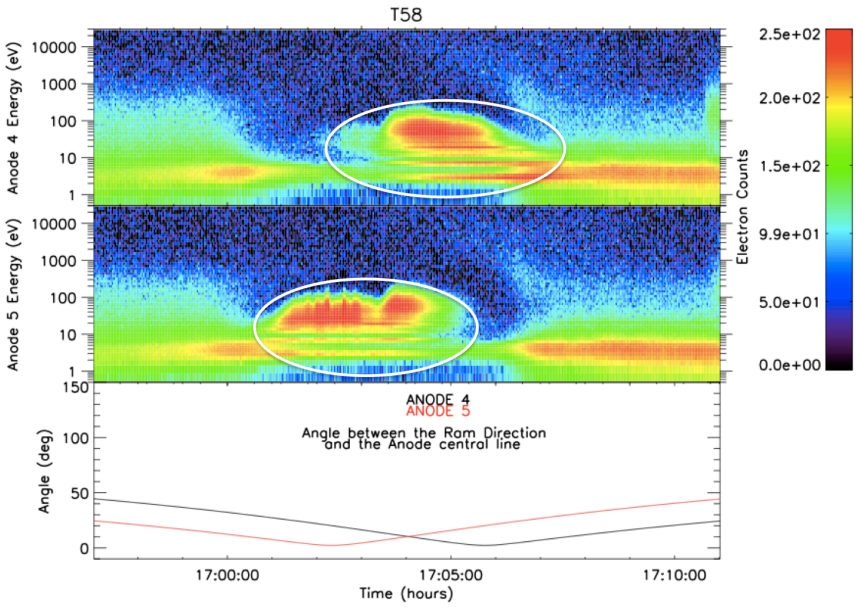

Figure 88. Top two panels: T58 spectrograms of anodes 4 and 5. A continuous, large negative ion structure is visible during this actuator fixed flyby (marked by white circles). Bottom panel: Angle of the two central anodes with respect to the ram direction.

5.7.3. Mass spectra time lapse: A closer look at T57

The aim of this section is to show how the shape of negative ion mass spectra evolves throughout an encounter. We chose T57 for this analysis because it is one of only two flybys (T59 being the other one) where the angle between the two central anodes and the ram direction was kept constant throughout the flyby (see section 5.7.2 and Figure 87). Figure 89 and Figure 90 show a total of 44 individual T57 mass spectra. They are spaced 10 seconds apart and are each taken from one energy sweep only.

The first spectrum shown is at 18:29:10 UT (c.f. Figure 87) and the last at 18:36:20 UT. CA was at 18:32:35 UT which is between the spectra numbered 21 and 22 in Figure 89. The spacecraft is in shadow on the inbound leg and the terminator is between the spectra numbered 15 and 16 at 18:31:35 UT.

The structure of the mass spectra can be described as consisting of three parts: The two lowest mass group peaks and the main body which is a broad peak made up of a number of smaller peaks. These peaks are the same as the peaks of the mass groups described in section 5.3. As we get closer to CA, the main body becomes wider i.e. it starts to extend towards the higher energies, while the smaller peaks stay at roughly the same energies. The highest peak of this main body also increases in mass as the altitude decreases. From spectrum number 17 we start to see a bump at higher energies than the main peak. This is part of the group 7 peak described in section 5.3 which is only found during some encounters. Some of the smaller peaks disappear because they seem to get “consumed” by the energy extent of the highest peak. For example, in spectrum 11 there is a small bump left of the highest peak. This is not properly visible any more in signature 12.

After CA, these developments start to reverse. However, after crossing the terminator i.e. when the spacecraft comes out of Titan's shadow (from spectrum number 16), the intensity of most masses decreases quickly. This effect seems to be most pronounced at the higher masses. We further discuss this effect later in this and the next section.

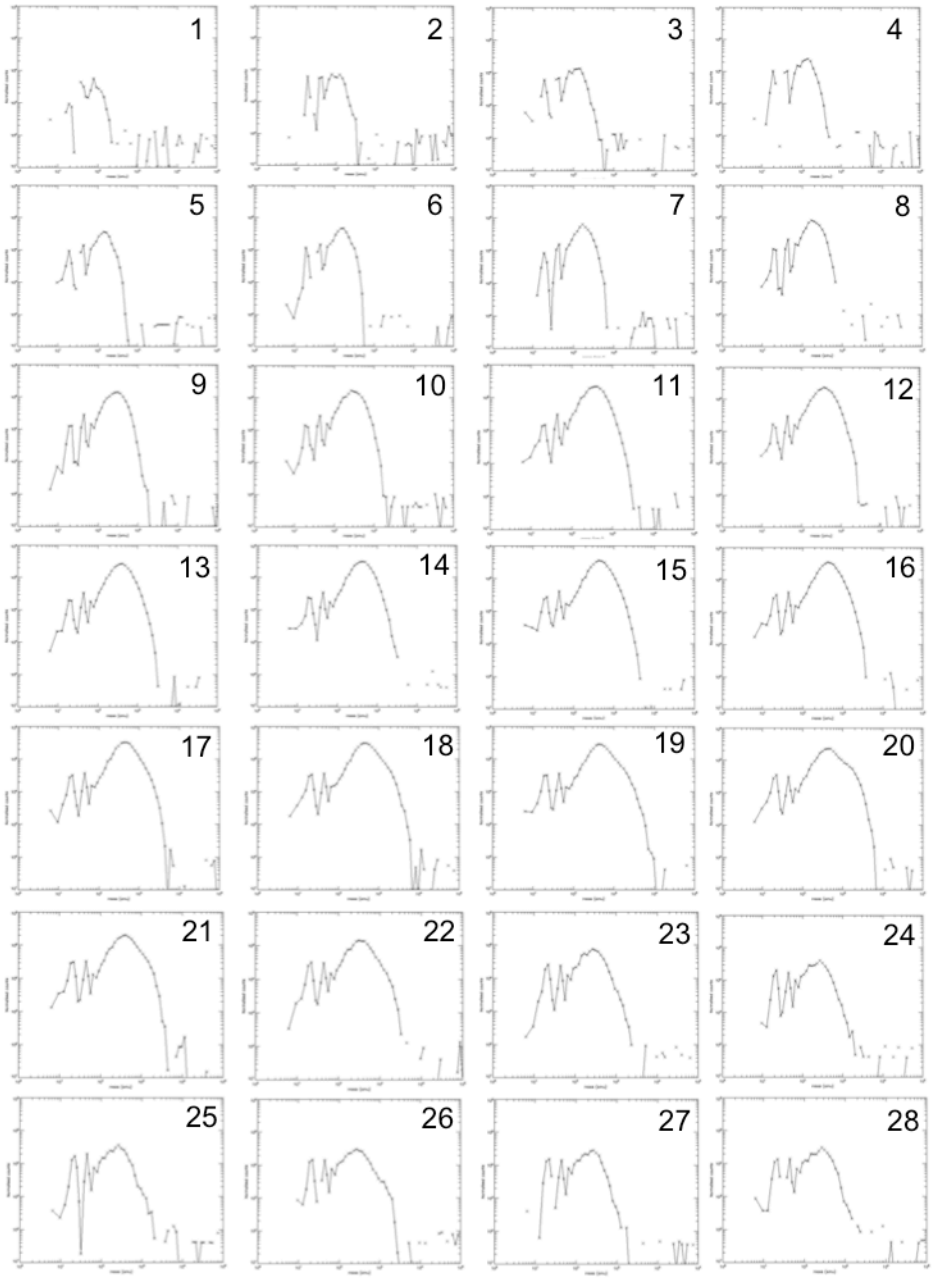

Figure 89: T57 negative ion mass spectra spaced 10 seconds apart. The horizontal axis is in amu/q and the vertical axis in normalised counts. This figure shows the first 28 spectra. They continue in Figure 90.

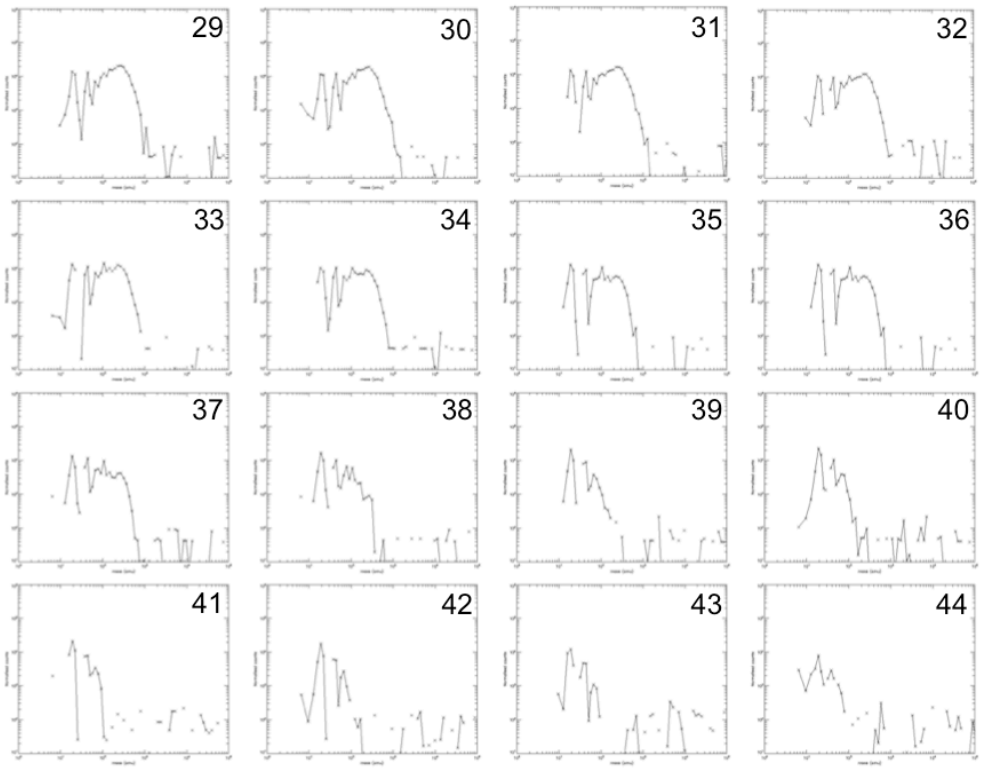

Figure 90: T57 negative ion mass spectra spaced 10 seconds apart. The horizontal axis shows mass in amu/q and the vertical axis shows normalised counts. The first 28 spectra are shown in Figure 89. This plot shows the last 16 spectra.

5.7.4. Altitude profiles

The four flybys we are considering all involve a crossing of the terminator during the time period when negative ions are observed. In addition, the actuator is fixed and therefore we have a set of continuous data available. The combination of these observations in one data set provides a unique opportunity to study possible changes in density that occur as a result of being shielded from solar radiation initially when the spacecraft is in shadow, to then being exposed to a low solar flux after crossing the terminator to the NTD (near terminator depression) region (see section 5.6.4). In this subsection we investigate the possible effects of these changes in more detail.

5.7.4.1. SZA – altitude coverage

Figure 91 shows T55 - T58 flyby information. The T55 observations were in shadow until shortly after CA. The spacecraft crossed the terminator just after and before CA during T56 and T57, respectively. During T58 the observations were on the night side until just below 1100 km on the inbound leg.

As we discuss the individual mass groups in the next subsections, we need to keep in mind the altitude bias (described in section 5.5.2) that becomes increasingly important with higher masses. The reference altitude (Table 7) gives some indication of when we can expect higher mass negative ion densities. However, the reference altitude only shows at which altitudes we start to see low densities. We need to refer to Figure 70 to Figure 76 to see at which altitudes it is possible to observe higher densities, too, and what SZA range is available for each flyby at this altitude range from Figure 91.

In section 5.6.4 we found that in the NTD region predominantly low densities are observed. The upper boundaries of the affected region are between 120° and 130° for all mass groups except group 7, for which it is approximately 100°. With the four slightly different SZA ranges available from T55 – T58, we can investigate whether this NTD region boundary is present in the data shown. Considering the restrictions related to the altitude bias and using Figure 91, we find that there is only a very small window to observe changes for each flyby that may be related to changes in solar input, especially at the higher masses.

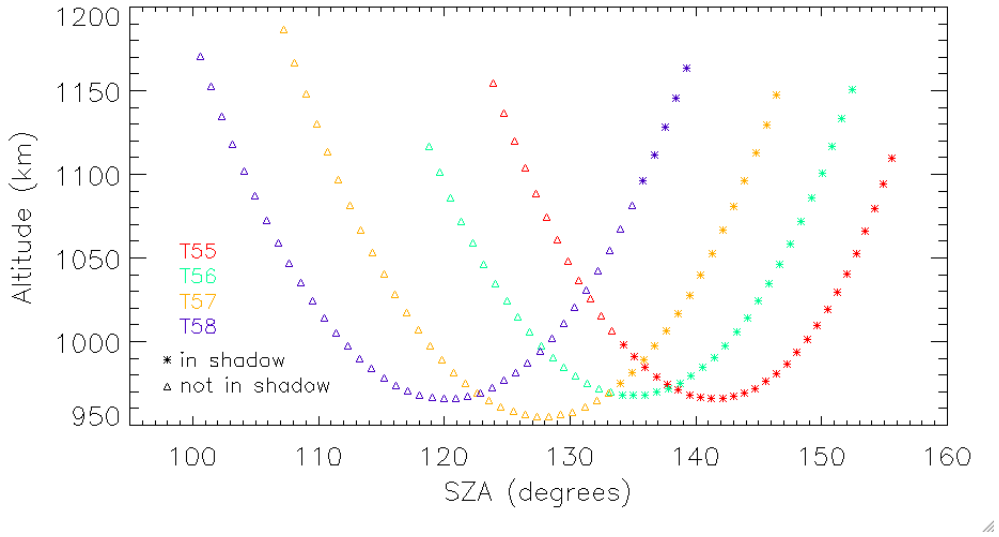

Figure 91: T55 – T58 flyby information. Each data point represents one time stamp of the negative ion sample. The data points show corresponding altitude and SZA information for each flyby. The colours shown indicate the flyby. The symbols (asterisks or triangles) indicate whether the sample was observed when the spacecraft was in shadow. All four flybys were in shadow on their initial part of the inbound leg. Hence the start of the inbound leg can be identified by the asterisks.

5.7.4.2. Results

Figure 92 to Figure 98 show altitude density plots of T55 – T58. Information about when the spacecraft was in Titan's shadow (i.e. on the night side) is also included. The change from asterisk to triangle marks the terminator crossing (in Figure 92 to Figure 98 and also Figure 91) which is at approximately 135° but the terminator SZA increases slowly with altitude. The data points in Figure 92 to Figure 98 are joined by lines only to show the order of the data points. The reference densities (see section 5.6.2) are indicated by the dashed vertical line. The higher mass group reference densities are low, hence they are not visible in the figures.

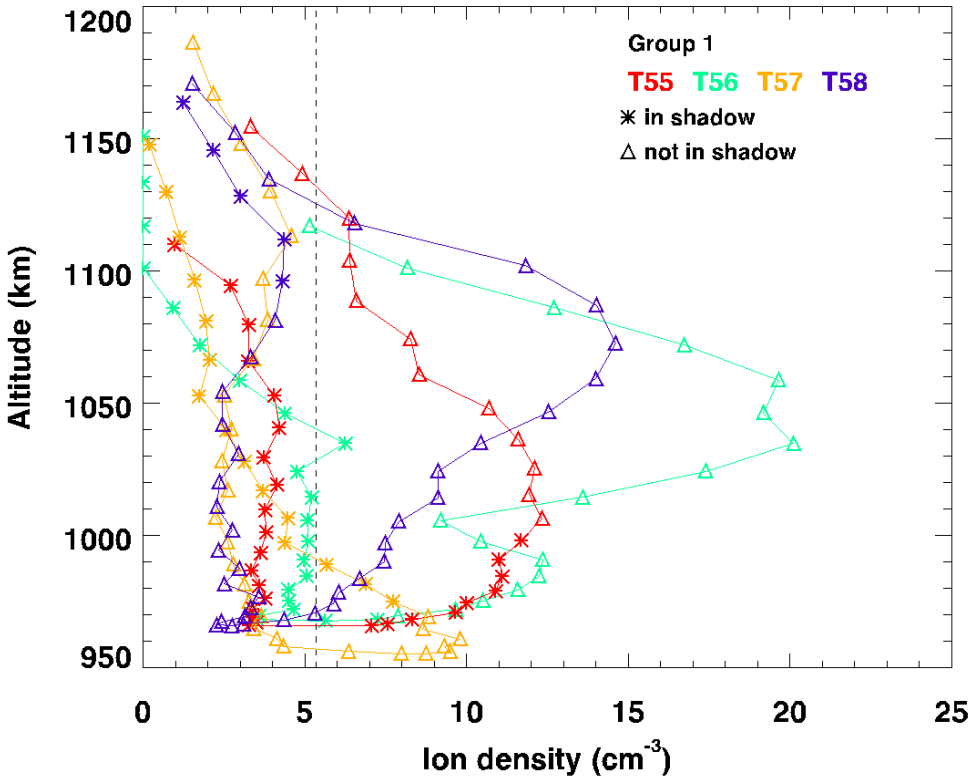

Figure 92: Group 1 density profiles of data from the four actuator fixed flybys T55 – T58. The different colours correspond to the respective flybys. The symbols (asterisks or triangles) indicate whether the sample was observed when the spacecraft was in shadow. The vertical dashed line indicates the reference density.

The group 1 densities do not show much variation on the inbound leg; densities generally remain approximately constant or increase by a small amount. However, almost all data points of the inbound legs of all four flybys are below the reference density. T55, 56 and 58 densities are higher on the outbound leg when they are not in shadow any more. These densities peak at altitudes around 1050 km and decrease at lower altitudes. T57 densities are slightly higher on the outbound leg when they are not in shadow any more, and peak at the lowest altitudes.

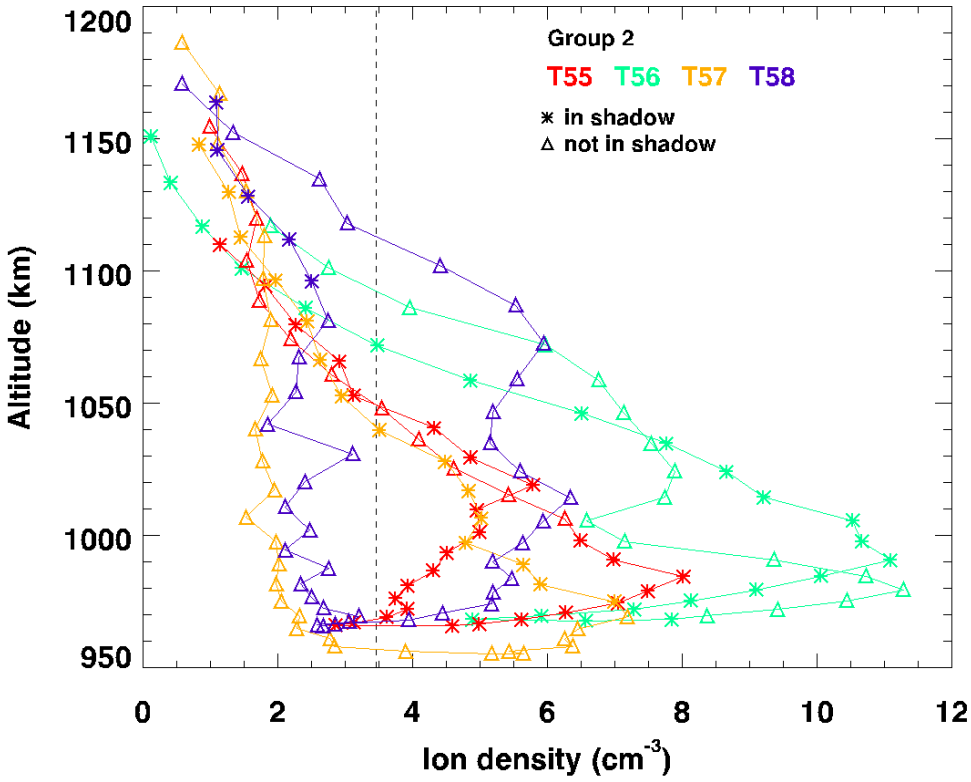

Figure 93: Group density profiles of data from the four actuator fixed flybys T55 – T58. The different colours correspond to the respective flybys. The symbols (asterisks or triangles) indicate whether the sample was observed when the spacecraft was in shadow. The vertical dashed line indicates the reference density.

Group 2 densities are more varied and the four flyby data exhibit different behaviours. Again, a number of data points are below the reference density. T55 densities are notably similar during the inbound and outbound legs at altitudes above 1000 km. At these altitudes they increase steadily with decreasing altitude. Below 1000 km the inbound densities (in shadow) decrease with decreasing altitude until just before CA. Around CA, densities suddenly increase even though the altitude remains almost constant. The peak density is reached at 975 km, only a few seconds before crossing the terminator. Densities then decrease steadily with increasing altitude.

T56 group 2 densities are also similar on the inbound and outbound legs at altitudes above 1020 km where they increase rather quickly with decreasing altitude. Below 1020 km, data from both legs seem to suddenly fluctuate and both drop to much lower values quite rapidly near CA when the altitude does not change much, just shortly after reaching the peak density around 980 km. The terminator is crossed just after CA.

The inbound densities of T57, which increase slowly with decreasing altitude, are higher than the outbound densities. When the terminator is crossed near CA, densities drop quite rapidly and stay approximately constant at a low density for the rest of the outbound leg.

T58 inbound densities are lower than the outbound densities and they "meet" at CA. The terminator is crossed early during the inbound leg.

The findings of mass groups 1 and 2 are inconclusive. Some of the flyby densities are higher after the terminator crossing into daylight, some higher before it. A fairly large amount of the data, including most of the group 1 inbound legs, are below the reference density and therefore may not be accurate relative to the other data. In addition, the reference density also indicates the size of the density uncertainty due to the electron background subtraction and inter anode scaling, as discussed in section 5.6.2. This is the dominant random uncertainty. The differences in density between the inbound and outbound leg data are less than this uncertainty in most cases. Moreover, compared to the densities of all flybys in section 5.6, the group 1 and 2 densities of the actuator fixed flybys are all in the low density range. The group 1 and 2 actuator fixed density maxima were only approximately 20% of the overall group 1 maximum, and 10% of the overall group 2 maximum, respectively. For these reasons the density fluctuations observed may not be real, or may simply be due to other natural fluctuations as a result of small changes in the environment.

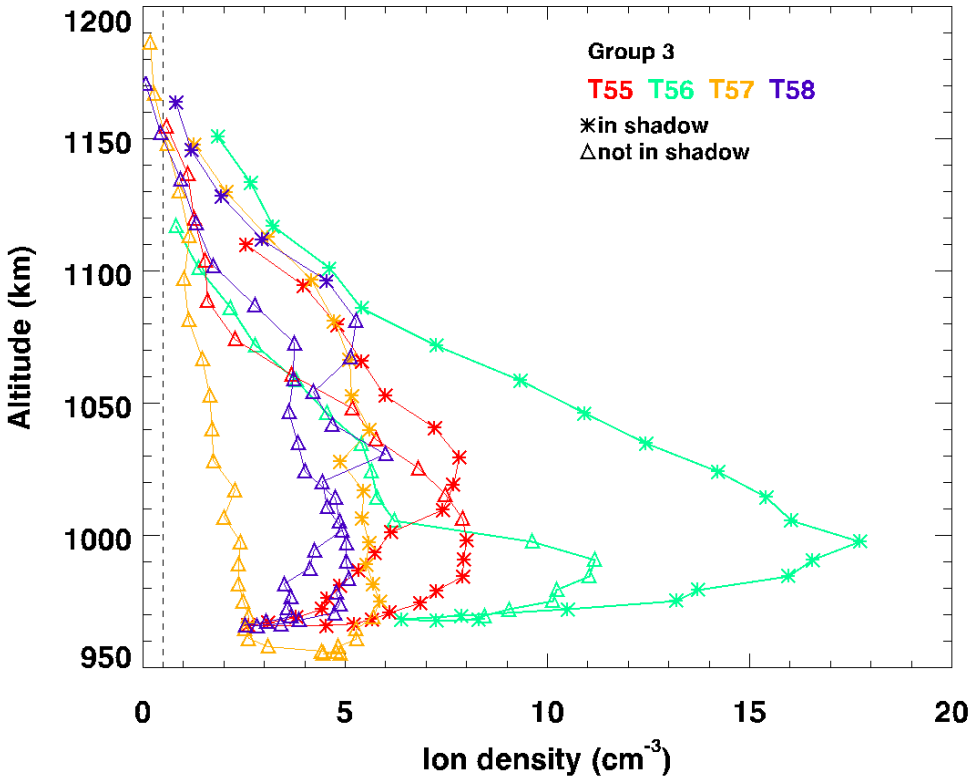

Figure 94: Group 3 density profiles of data from the four actuator fixed flybys T55 – T58. The different colours correspond to the respective flybys. The symbols (asterisks or triangles) indicate whether the sample was observed when the spacecraft was in shadow. The vertical dashed line indicates the reference density.

Group 3 densities are mostly higher on the inbound leg. Almost all data points are above the reference density. T55 densities of the inbound leg are similar but higher than the outbound leg above 1010 km. Here, the inbound densities peak and then decrease with decreasing altitude, crossing the densities of the outbound leg which peak at a slightly lower altitude. Both the inbound and outbound legs then "meet" at CA at a lower density. The peak of the outbound densities coincides with the terminator crossing; the outbound densities are only lower than those of the inbound leg when the inbound leg is in shadow.

T56 densities increase quite rapidly on the inbound leg with decreasing altitude and reach a peak just under 1000 km. They then decrease until CA after which they

increase again to reach a lower density outbound peak around 980 km just after the terminator is crossed. Densities then decrease for the rest of the outbound leg. The rate at which they decrease around 1000 km is very rapid and also higher than the rate at which the inbound densities increase. Overall, the inbound densities are notably higher than the outbound densities above 1000 km, which is at a SZA of 127° and lower.

T57 inbound and outbound densities start off at similar values at 1150 km but then the inbound leg increases slowly whereas the outbound leg remains almost constant, increasing slightly with decreasing altitude. Densities on the inbound leg cease to increase significantly below 1070 km but are overall higher than outbound densities throughout the flyby. The only major change occurs at the terminator crossing when densities drop quite rapidly.

T58 densities are similar inbound and outbound. Densities on both legs fluctuate but only in quite a narrow density range. The inbound leg densities are slightly higher for the majority of the flyby.

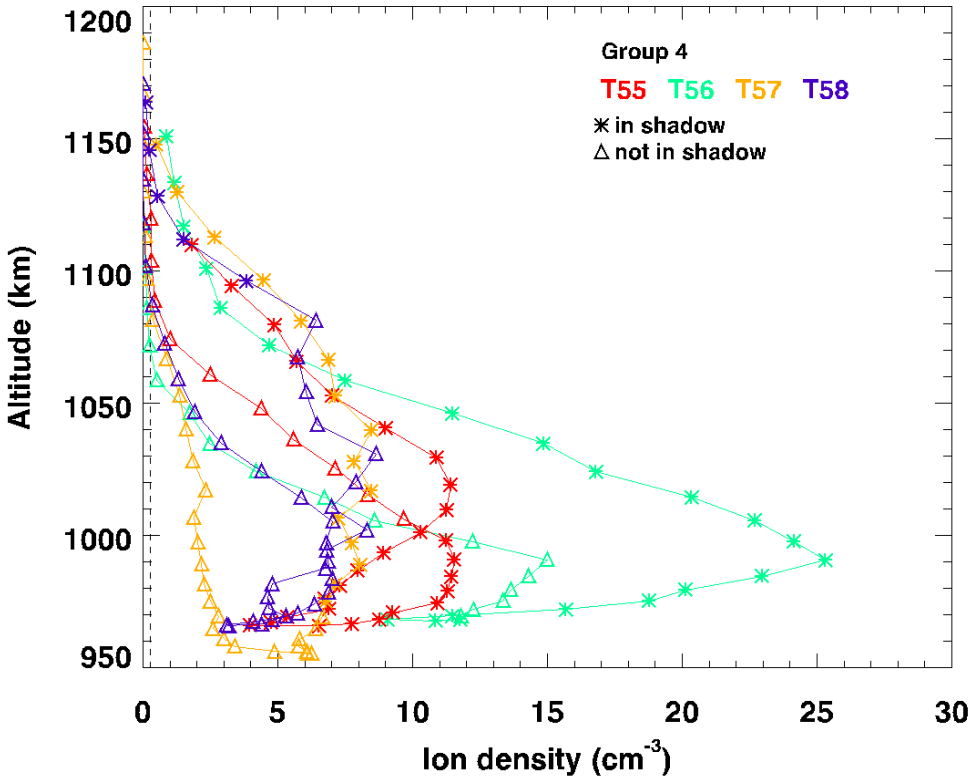

Figure 95: Group 4 density profiles of data from the four actuator fixed flybys T55 – T58. The different colours correspond to the respective flybys. The symbols (asterisks or triangles) indicate whether the sample was observed when the spacecraft was in shadow. The vertical dashed line indicates the reference density.

Group 4 densities are very similar to group 3. Densities start to increase at slightly lower altitudes. The difference between T58 inbound and outbound densities is higher above 1030 km. Below 1030 km, T58 densities decrease with decreasing altitude, as opposed to a slow increasing trend at higher altitudes. The other flyby data resemble those of group 3.

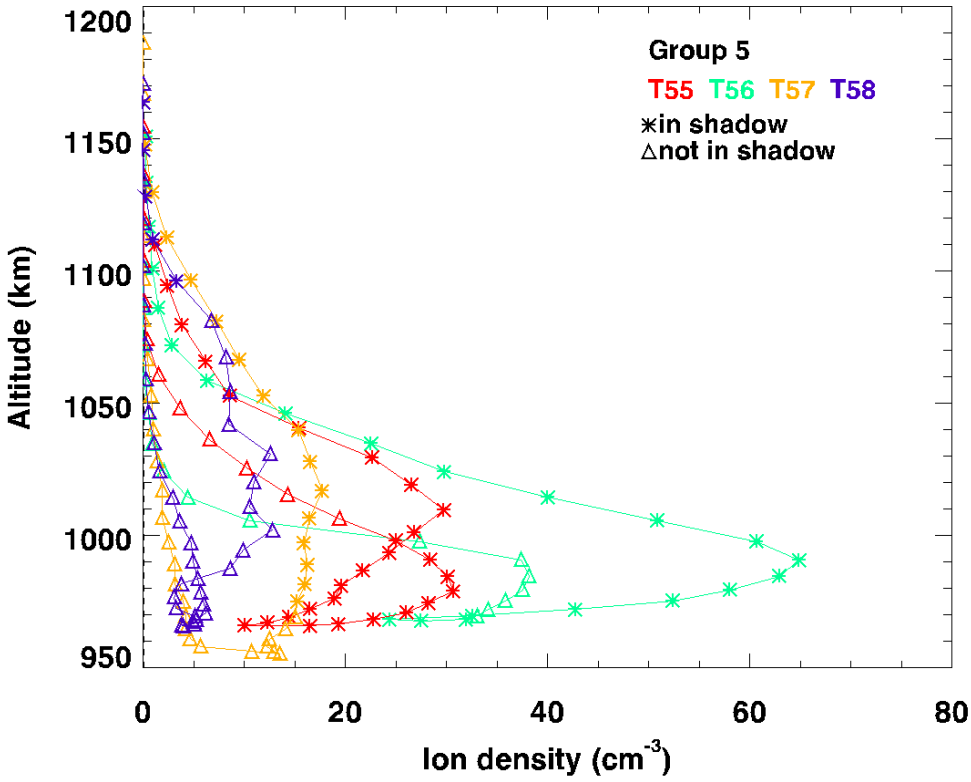

Figure 96: Group 5 density profiles of data from the four actuator fixed flybys T55 – T58. The different colours correspond to the respective flybys. The symbols (asterisks or triangles) indicate whether the sample was observed when the spacecraft was in shadow. The vertical dashed line indicates the reference density which is quite low in this case hence very close to the altitude axis.

Group 5 densities are, again, very similar to groups 3 and 4 apart from the fact that the densities only start to increase at yet lower altitudes. The T58 outbound densities are lower relative to the other flybys and the inbound densities are higher than the outbound ones for the entire flyby except near CA where they are comparable.

Groups 3 and 4 are also mostly in the low and intermediate density range compared to all flybys in section 5.6.4. The group 5 density axis scale is almost the same as that of all flybys in Figure 82, however this is mainly due to high T56 densities. The other group 5 flyby densities also reach low to intermediate values. Therefore, some of the small density changes could be related to minor changes in the ambient conditions.

Nevertheless, group 3 to 5 results generally agree well with the findings related to the NTD presented in section 5.6.4. The outbound densities (not in shadow i.e. mostly exposed to low solar flux) of T56 and T57 are lower than their respective inbound densities (mostly in shadow i.e. no solar flux). This supports the result that lower densities are found in the NTD (near terminator depression) region (where only low solar flux is present). The upper SZA boundary of the NTD region for T57 seems to be very close to the terminator. During T56, densities increase initially after CA and the terminator crossing (which almost coincide in this case) but then decrease rapidly around 1000 km / 127° SZA. The initial increase on the outbound leg could be because the NTD boundary during this flyby is at a slightly lower SZA, which is in the range described in section 5.6.4. On the other hand, the initial increase could also be due to the altitude trend that the density peak is reached just over 1000 km (depending on the mass group, see Table 7). It is likely due to a combination of these two trends. The difference between inbound and outbound densities during T55 and T58 is not as large, which also agrees with the NTD findings: The NTD region only covers part of the T55 outbound leg, which also occurs at higher altitude (see Figure 91). Nonetheless, a small difference can be observed. On the other hand, a large part of the T58 flyby trajectory is within the NTD region. This means that again differences are only expected to be small and at higher altitude, which is the case.

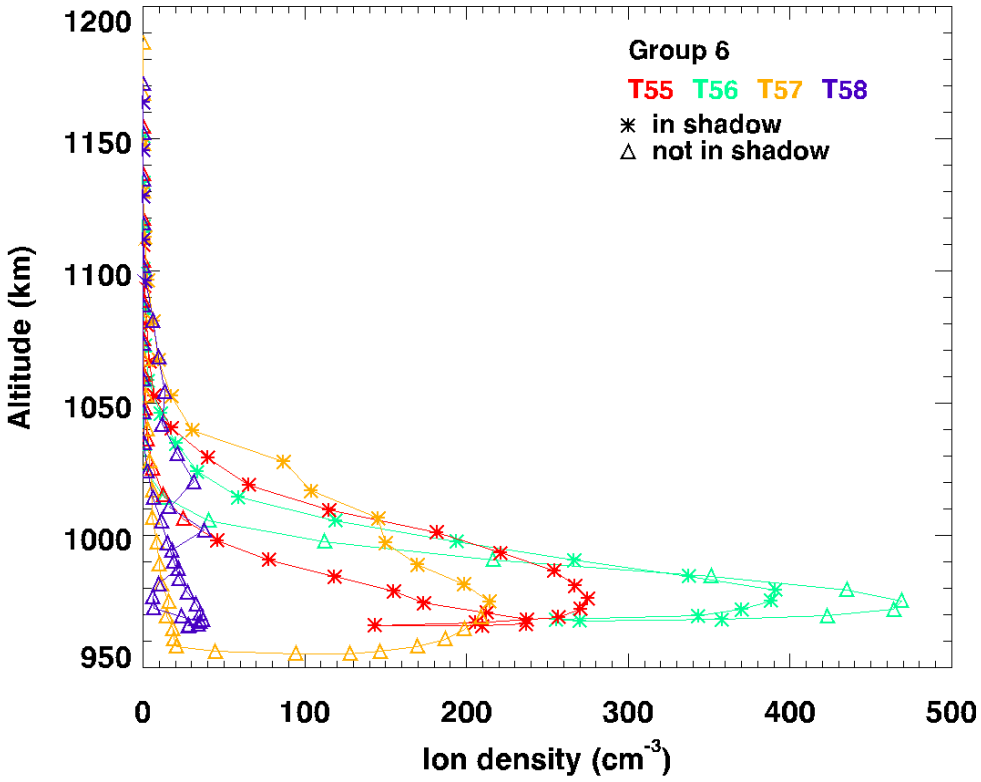

Figure 97: Group 6 density profiles of data from the four actuator fixed flybys T55 – T58. The different colours correspond to the respective flybys. The symbols (asterisks or triangles) indicate whether the sample was observed when the spacecraft was in shadow. The reference density is so low in this case that the vertical dashed line marking it is too close to the altitude axis to be visible.

Group 6 density profiles are still somewhat similar to the previous three groups but there are some differences. Again the densities start to increase at lower altitudes than previous groups. T55 inbound and outbound densities only 'overlap' close to CA; the inbound densities are higher than outbound for almost the entire flyby. The T56 profile is similar structurally but more stretched out in the higher densities. T57 inbound densities are significantly higher than the outbound densities and drop rapidly after crossing the terminator near CA. T58 inbound and outbound densities are similar and also low compared to the other flybys.

Group 6 data generally also agree with findings of the SZA density trend in the previous section. The densities reach intermediate to high densities compared to all

flybys. The very noticeable difference between inbound and outbound densities during T57 occur again just after the terminator crossing, therefore the NTD boundary is at a slightly higher SZA than the results in section 5.6.4. The T56 NTD upper boundary is not properly observed, although there are signs of it when the outbound densities start to decrease faster with increasing altitude than the inbound densities around 1000 km. This is at 127° SZA which is in the expected NTD boundary range, and it is also where it was observed in the lower mass groups where the altitude range was not as restricted.

The group 6 T55 densities at higher SZAs are higher than the ones at the same altitude at lower SZAs. However, the NTD SZA range is only covered at higher altitudes at which densities are too low in this mass range. Therefore, the difference in the densities may be due to other changes in ambient conditions, or the NTD boundary is at a SZA slightly higher than expected. Nevertheless, the fact that T55 densities reach the intermediate range relative to all flybys (see Figure 83) shows that the data agree with the results that at these higher SZAs densities can reach higher values. On the other hand, T58 densities are mostly well within the NTD region and are low, which also agrees with the general SZA density trends found in 5.6.4.

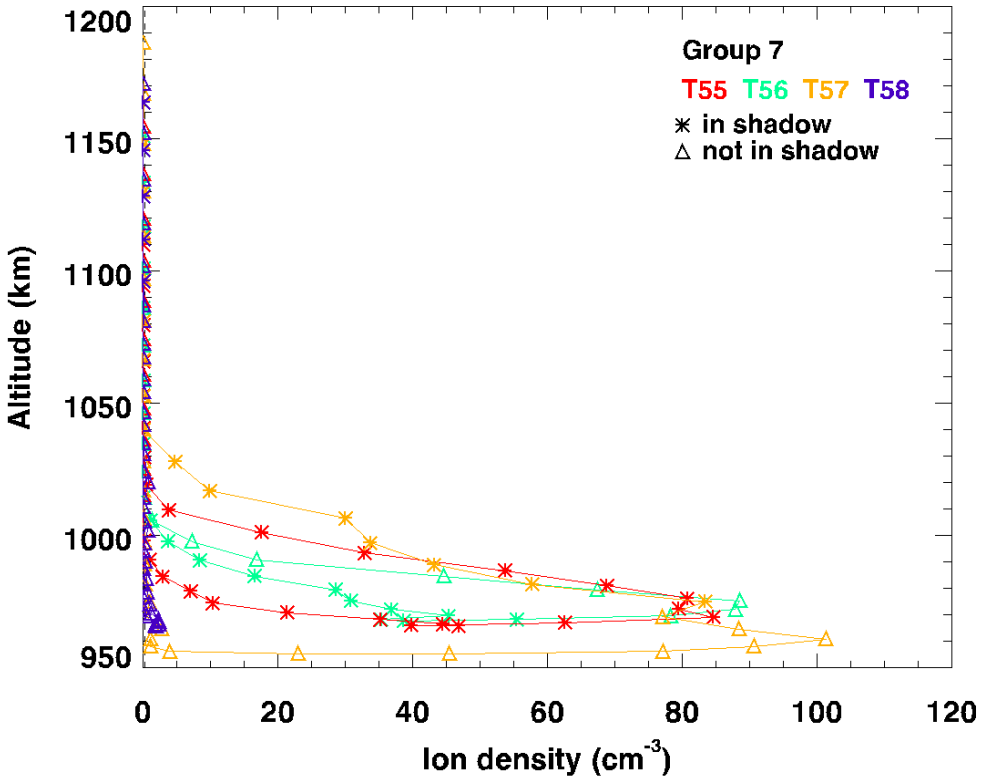

Figure 98: Group 7 density profiles of data from the four actuator fixed flybys T55 – T58. The different colours correspond to the respective flybys. The symbols (asterisks or triangles) indicate whether the sample was observed when the spacecraft was in shadow. The reference density is so low in this case that the vertical dashed line marking it is too close to the altitude axis to be visible..

Group 7 densities are only significant at the lowest altitude, below 1050 km. From T55, only densities obtained when in shadow are high enough to be visible on the plot, and a peak is reached around 980 km. The T56 peak is reached at the same altitude as T55 after which densities drop quite suddenly. T56 in shadow densities are lower than when not in shadow at very low altitude but they are otherwise similar. The T57 peak is reached at slightly lower altitude, around 960 km. This is also where the terminator has just been crossed, after which densities drop very rapidly. The remaining outbound data points above 960 km are so low they are not visible on the plot therefore the difference between inbound and outbound is very large. T58 densities both inbound and outbound are very low and barely visible on the plot even at very low altitudes. This is the only group where T57, and not T56,

reaches the highest densities of the four flybys, but only by a relatively small amount.

The analysis of the group 7 data is very similar to the group 6 analysis above. One main difference is that in the group 7 T56 data no signs of the NTD boundary are observed. The altitude range is even more restricted here and the range in which it was observed during lower mass groups is not available. If we compare the results to the scatter plot in Figure 84, intermediate to high densities are reached. However, the upper NTD boundary observed in Figure 84 was at a lower SZA than that of the other groups: 100° compared to 120° – 130°. The data in this section suggests that the boundary is more likely to be similar to that of mass group 6, if the interpretation of it is correct. On the other hand, only T57 data shows a particularly strong reaction to the solar input after the crossing of the terminator. Conversely, T57 also offers a larger number of data points in the available altitude window because CA is approximately 20 km lower than that of the other three flybys.

5.7.4.3. Summary

We have further investigated the SZA trends near the terminator found in section 5.6.4 using altitude profiles of continuous negative ion signatures from four actuator fixed flybys. Results for mass groups 3 to 5 mostly agree well with the result that low densities are found in the NTD region and these are generally lower than the densities at higher SZAs. Results from mass groups 6 and 7 are more difficult to draw conclusions from because of a smaller altitude window, but generally also appear to agree with lower densities below a certain SZA around 130°. However, the group 7 upper NTD boundary was found to be around 100° from the scatter plots; we will discuss this further in the next section. Results from these scatter plots also suggested that the upper SZA boundary of the NTD for mass

groups 1 – 6 is usually between 120° and 130°. The results in this section show that in some cases the boundary can be closer to the terminator. A consistent example of this in all mass groups is T57.

The group 1 and 2 results in this section were inconclusive due to a number of problems described above.

The small T58 density fluctuations may be related to the vertical striation structures mentioned in section 5.7.2. Even though the structures in the spectrogram are related to suddenly observing a larger mass range, there may also be related changes in densities. In future, these could be analysed further by using an even larger number of data points. Due to the continuous data available, this number is only limited by the timing of the instrument energy sweeps, which is two seconds. The work of Jones (pers. comm., 2009) will also be useful in the further analysis of these interesting structures.

A few mass groups have only very small changes in the densities over the entire inbound altitude range. This is also evident in the higher mass groups – as soon as their density is established at a certain altitude (above which they are virtually zero), they stay relatively constant until CA.

These density profiles will also be useful in future studies as part of investigating density altitude trends. The profiles can be compared to other flyby data. There are two more actuator fixed flybys (T59 and T61) that have not been analysed yet. Other flybys where the actuator was not fixed can also be used to produce altitude profiles, although the smaller number of available negative ion samples would make it more difficult to observe changes occurring within short time periods.

5.8. Discussion and conclusions

5.8.1. Science summary discussion

5.8.1.1. Altitude trends

The general altitude trends observed are:
(1) Higher densities and masses at lower altitudes
(2) The higher the mass group, the lower the maximum altitude at which these ions are observed (the reference altitude).

We saw in section 5.6.3 that the altitude at which the maximum density for each mass group is observed decreases with increasing mass. Below these altitudes, the maximum observed mass at a certain altitude decreases again. We also observed the altitude trend in an individual flyby in section 5.7.3; the main peak in the T57 counts (which is related to density) spectra increases as the altitude decreases.

We can see from the results presented in section 5.6.3 that at a given altitude, or altitude range, a sometimes large variety of densities is observed. Therefore the altitude of the overall maximum density for a group does not necessarily mean that this is where the peak will be under every set of conditions and is not the same for each flyby. The maximum density is often reached at similar altitudes. However, the value of the maximum density of a group for a specific flyby can vary considerably, even if found at a similar altitude. On the other hand, the altitude profiles of the actuator fixed flybys in section 5.7.4 showed that in some cases, there is no noticeable altitude peak and the densities stay constant over large altitude ranges.

We can compare the peak altitude of groups 1 - 3 with the CN^-, C_3N^- and C_5N^- densities calculated by Vuitton et al. (2009) as discussed in section 5.4. 1050 km for group 1 is very close to approximately 1060 km for CN^-. 1030 km for group 2 is still

reasonably close to 1000 km for C_3N^-. The group 3 peak is at 1018 km which is higher than 960 km for C_5N^-. The trend for the peak altitude to be lower for higher mass is followed by both observations and calculations. In future, it will be interesting to compare these data with electron and positive ion peaks.

The Coates et al. (2009) study and the continuation of it in section 5.5 showed that the highest masses are observed at low altitudes. One difference between the density and mass trends is that the density peaks seem to be reached above the lowest altitudes sampled (950 km), whereas the highest masses are observed at the very lowest altitudes. The peak densities of most of the individual mass groups occur at altitudes above 950 km, as summarised in Table 7 in section 5.6.3.

Coates et al. (2009) pointed out that the maximum mass result agrees with the result in Vuitton et al. (2009) that electron attachment is the main negative ion formation process at these higher altitudes. Even though Vuitton et al. (2009) only considered the lighter ion species relevant to groups 1-3, this may apply to the heavier mass species too. Titan's cold electron population, including the main thermal population at 1 – 10 eV and also suprathermal photoelectrons at approximately 24 eV are available for both dissociative and also radiative electron attachment reactions to take place. The trend that higher densities are present at lower altitudes seems to strengthen this theory.

5.8.1.2. SZA trends and the NTD region

The general SZA density trends were described and summarised in section 5.6.4. The effects of the presence and absence of solar radiation (i.e. low and high SZAs, respectively) on the different mass groups were explored. The lower mass group densities tend to be highest on the dayside, whereas for some higher mass groups the highest densities are found on the night side, or even at both high and low SZA

angles. The most striking result of this part of the density study is the lack of high or intermediate densities in the region between the surface terminator at 90° and the actual terminator at approximately 135°. In section 5.6.4 we learnt that for most mass groups, this effect appears to be most pronounced in the region 100° - 120°. We refer to the effect as the *near terminator depression* (NTD). At these SZAs, solar flux is still present but low (see section 5.5.5).

Further density trend results from the actuator fixed flybys T55 – T58 were discussed in detail in section 5.7.4. Altitude profiles for groups 1 and 2 were inconclusive due to a number of reasons including high random uncertainties. However, altitude profiles of groups 3 – 6 generally agree well with the findings of the overall SZA density trends, although some data showed that the upper NTD region boundary can be closer to the terminator than was found in section 5.6.4; an example of this is T57 during which densities for all mass groups plummet as soon as solar radiation is present.

In section 5.6.4 the group 7 data indicated a NTD region at SZAs between 75° and 100° which is at a lower SZA range than the other mass groups. However, the group 7 altitude profile in section 5.7.4 suggested that the upper boundary may be the same as those of the other mass groups, although the data were restricted due to a very small altitude and hence SZA window (see section 5.7.4.1). It is possible that the group 7 NTD may generally be present in a large SZA range, between 75° and 135°. In the group 7 scatter plot containing all flyby data in Figure 84, there are five data points around 110° SZA that are at intermediate densities. Considering the restricted group 7 altitude range and hence a lower number of samples, five data points is not an insignificant number. This led to the preliminary conclusion in section 5.6.4 that the group 7 NTD region is at a lower SZA range; no intermediate or high densities are present between 75° and 100°. On further analysis, four of the five data points that show intermediate group 7 densities around 110° are T16 data. As discussed in section 5.5.6, T16 data show the highest masses of all negative

ions observed with CAPS-ELS. It was also found that the reason for this may be a combination of a seasonal and latitude effects: T16 is the closest polar flyby in time to the 2002 northern winter solstice. Such conditions may also result in high densities, which may have been dampened due to the effects of the NTD.

The lower number of data points and the restricted altitude range make the analysis of group 7 data more challenging than for the other mass groups. Future flybys will increase the number of group 7 negative ions signatures which will help in finding the location of the NTD region, if it exists for group 7.

As discussed for the altitude trend study, at a particular solar zenith angle we observe a range of densities. Hence even when very high density data points are present, we usually observe a range of intermediate to low densities, too. Therefore, if high densities are observed at a certain SZA, this does not mean that we will always find high densities at these angles.

5.8.1.3. Data point distributions and sampling

We can take a closer look at the distribution of data points on the SZA density plots. We use group 1 as an example (Figure 78). When higher densities are observed, on the dayside, the data points have a reasonably wide distribution. In the NTD region, on the other hand, there are no high densities and the data points are clustered at low densities. On the night side, the data points are again more spread out from low to intermediate densities. This, combined with the sampling distribution in Figure 60, suggests that the trends summarised above are real.

5.8.1.4. Concepts to explain the SZA trends and the NTD

In the NTD region only a low flux of solar radiation reaches this part of the ionosphere due to the long path length through the atmosphere (also see section 5.5.5). We now discuss some ideas that may explain the presence of predominantly low densities in the NTD region, and the general SZA trends.

There may be a balancing effect that does not allow the densities to rise above a certain level. Photochemical reactions may be limited due to the low solar flux available. The two photochemical reactions affecting negative ions that have photons as a reactant are ion-pair formation and photo-detachment. Ion-pair formation creates negative ions, whereas photo-detachment destroys them (see section 5.4). At low SZAs, both photo-detachment and ion-pair formation are at work. Maybe ion-pair formation is only effective in stronger sunlight, whereas photo-detachment reaction rates are kept at a moderate level right until the solar flux is turned off completely (i.e. the terminator at 135°), or just before it. In this case ion-pair formation would not be present in the NTD region to 'balance' or 'counter' the destruction rate due to photo-detachment. In a similar way, other photo-dissociation reactions may keep up low reaction rates when some solar flux is still present.

The NTD is more prominent in the higher mass groups. This could indicate that the ion-pair formation reaction rates producing lower mass negative ions are less affected by less solar radiation until the flux becomes very small, whereas ion-pair formation rates creating higher mass negative ions decrease more quickly as a function of decreasing solar flux. On the other hand, it may also mean that it is easier for photo-detachment to occur on higher mass negative ions when the solar flux gets lower than on lighter ions.

If we assume for a moment that the differences between day and night side densities, and also the NTD, are direct results of certain photochemical reaction rates being high at low SZAs and zero or very low at high SZAs, then we can draw certain conclusions from the results about the types of reactions that may contribute significantly to the densities. The lower mass groups have significantly more intermediate and high density data points at low SZAs, therefore if we consider photochemical reactions only, ion-pair reaction rates are very high on the day side, while photo-detachment reactions are not as effective. This result would be in some disagreement with the Vuitton et al. (2009) results. Their results indicate that photo-detachment is not as important as any of the other destruction reactions considered (ion-neutral associative detachment, proton transfer and ion-ion recombination), but it does contribute to the destruction rates at the higher altitudes of the Cassini flybys. Their results also indicate that photo-detachment reactions are more efficient at destroying negative ions than ion-pair formation at creating them.

However, it is more likely that the solar flux has a more indirect way of causing the differences on the day and night side, and the NTD region, or at least in addition to influencing the photochemical reactions. Day-night transport, the rotation of the moon and winds may be some ways through which the densities are affected more indirectly. In addition, a factor that will no doubt have a significant effect is the difference between general ionisation rates on the day and night sides. On the night side, the magnetospheric plasma is the only ionisation source. This affects the dynamics and structure of the ionosphere in many ways (e.g. Cravens et al., 2009, Ågren et al., 2009). Electron and positive ion densities are different from the dayside densities. Therefore other reactants are available for the formation and destruction reactions of negative ions. For instance, thermal electrons are required for radiative electron attachment, and suprathermal electrons for dissociative electron attachment. Both reactions are believed to be some of the most important

negative ion formation reaction. Therefore these different conditions will affect the negative ion densities significantly.

Furthermore, we can try to use this 'availability' of different reactants to refine our explanation of the NTD above. On the dayside, photo-detachment and other photo dissociation reactions might destroy some of the products of ionisation caused by the magnetospheric plasma. The reactions producing negative ions are mainly using products of solar ionisation. On the night side however, there are no photochemical reactions destroying magnetospheric products and therefore different reactions take over producing negative ions. These reactions are more efficient at producing higher mass ions than lower mass ions. Near the terminator when some solar flux is still present, photochemical reactions are still destroying some of the magnetospheric products. However, there are fewer solar ionisation products in the same region, hence the reactions that were efficient at lower SZAs producing negative ions now only yield lower densities. Similarly, reactions that thrive on the night side cannot result in higher densities because there are insufficient reactants.

The above description is just one example of what could be happening as a result of different conditions. The point is that we seem to have three different regions – the day and night sides and a somewhat extended transition between them due to Titan's extensive atmosphere. Different conditions in these different regions result in different dominant reactions. In the NTD region, these reactions are in competition so there is a different balance where the destruction processes seem to 'win' and the formation reaction rates suffer.

Another question that this explanations poses is: Are the negative ion products also different in the different regions? We suspect that this is very possible. Despite the fact that certain masses seem to fall into certain mass ranges, or groups, they could be completely different species that happen to have the same or similar masses and are the result of the same or different chemical formation processes.

The higher mass groups are also not as well defined as the three lowest because the peaks do not always stay at the same energy as a function of decreasing altitude. In addition, according to Waite et al. (2009), the aerosols most likely form by the clumping of smaller molecules. Therefore, what kind of species the very high masses become may depend directly on the lower mass populations.

The highest maximum masses observed were found to be in the NTD region and around the terminator at 135°. At first it might seem peculiar to find the highest maximum masses in a region with the lowest densities. However, the highest maximum mass data points are from the T16 flyby. We established in section 5.5.6 that the T16 masses are probably so unusually high because of a seasonal effect and the high latitude of that encounter. It is possible that in this case, the SZA was not the parameter controlling the mass and the masses would have been high at any SZA. If we remove the T16 data points from the maximum mass SZA plot, we actually observe the highest masses on the dayside around 50° and also on the night side around the 135° terminator. We can generally see the highest number of intermediate to high maximum masses on the dayside and in the 135° terminator region. There is still a small number of masses that do not fall in the low mass range in the NTD region. It is possible that this is due to other controlling parameters such as seasons or latitude, too. In the future, we need to combine the latitude, season and SZA parameters to determine if there is also a near terminator depression in the masses. We discuss this further in section 5.8.3.

5.8.2. Uncertainties discussion

5.8.2.1. Uncertainty on negative ion mass

Here we discuss the uncertainties in the data analysed. We start with the uncertainty on the calculated mass of the negative ions. The energy resolution of CAPS-ELS is $\Delta E/E = 16.7$ %. This is the size of an energy bin. There is another uncertainty which affects the energy, and therefore the negative ion mass: the spacecraft electrical potential is negative in Titan's dense ionosphere (see section 2.2.1.5). Hence, negatively-charged particles are decelerated before detection and the observed energy therefore needs to be shifted according to this potential (see section 5.2). Spacecraft potential data is available from the RPWS Langmuir Probe (LP) instrument (Ågren 2012, pers. comm.). As discussed, Crary et al. (2009) have used a comparison of INMS data and CAPS-IMS data to determine spacecraft potentials. The Crary et al. (2009) data are likely to be more accurate due to the location of the instruments; the RPWS LP is located on a boom at a distance from CAPS-ELS. However, the Crary et al. (2009) data are only available for selected flybys therefore we use RPWS data to be consistent.

We now describe briefly how we selected the uncertainty on the spacecraft potential shift. Crary et al. (2009) performed a study that used CAPS-IBS data and INMS data to match the peaks of positive ions. This allowed them to determine the spacecraft potential for selected flybys. These data are only available for a number of flybys, therefore as described in section 5.2.3, we use RPWS spacecraft potential data in this study. However, it is useful to consider the results by Crary et al. (2009) for the purpose of analysing the uncertainties and also future work (section 5.8.3).

Data from the Crary et al. (2009) study were kindly provided (Magee, pers. comm. 2012). The data times generally match the times of the negative ion signatures more closely than do those from RPWS. This is because the positive ion signatures in CAPS-IBS usually occur roughly at the same time as the negative ion signatures in CAPS-ELS whereas the RPWS times are not related to CAPS ion signatures because they are completely independent of the instrument's actuator angle. The Crary et al. (2009) data are also more likely to be accurate in the CAPS area of the spacecraft because CAPS-IBS and INMS are much closer to CAPS-ELS physically than RPWS – the spacecraft potential may vary at different positions of the spacecraft. Crary et al. (2009) compared their data to RPWS data and report that there is generally an offset of 0.25 V which is believed to be due to the difference in location on the spacecraft. We use this offset as a minimum uncertainty because the difference between the spacecraft potential at CAPS-ELS and RPWS is likely to be similar.

The uncertainty on the RPWS spacecraft potential data is 10% (Ågren 2012, pers. comm.). The RPWS spacecraft potential data set is available at varying time intervals. These time stamps do not necessarily coincide with the negative ion signature time stamps. In addition, the negative ion signature time stamps are at the centre of the signature. However, as described in section 5.2, a small number of readings are taken slightly before or after the centre of the signature. These timing issues add to the uncertainty of the spacecraft potential used. For a small number of flybys, eg. the actuator fixed flybys, one constant value of spacecraft potential was used for the duration of the flyby, because the signatures were very close together. In these cases the constant was either an average of that flyby or a default value of -0.6 V which is believed to be a general average value (Crary et al., 2009, Coates et al., 2007b).

Taking all the above sources of uncertainty into account, we estimate a total uncertainty of 0.6 V with a 90% confidence level on the spacecraft potential used. This results in an energy shift of +0.6 eV. This uncertainty is a universal value used

in this study for all spacecraft potentials for all flybys. In reality sometimes the spacecraft potential uncertainties are smaller, e.g. when we have a measurement that coincides in time with an RPWS measurement. However, for the purpose of this study, we use this one "universal" uncertainty. In future, more specific uncertainties could be assigned; this could be done on a flyby by flyby basis or possibly even for each negative ion signature. For some flybys the data from Crary et al. (2009) could be used; these would probably be more accurate for the negative ions observed with CAPS ELS because (1) they were determined using the CAPS-IMS and INMS instruments which are much closer in location to CAPS-ELS and (2) the time stamps of the data are generally closer to the ELS negative ion centre time stamps. This is because the study is based on comparing the ion peaks observed with CAPS-IMS and INMS. The CAPS-IMS positive ion signatures will generally have the same or very similar time stamps to those from ELS ion observations because these positive ions are also observed when the CAPS actuator points in the ram direction.

In order to determine a total uncertainty on the negative ion mass, we need to combine the uncertainty due to the energy resolution and due to the spacecraft potential shift. The energy used for the negative ion mass conversion is given by

$$E = E_o + E_{pot}$$

Equation 30

where E_o is the observed energy and E_{pot} is the energy that needs to be added due to the negative spacecraft potential. The total energy uncertainty is therefore

$$\sigma_E = (\sigma_o^2 + \sigma_{pot}^2)^{1/2}$$

Equation 31

where σ_o is the uncertainty due to the observed energy and σ_{pot} is the uncertainty due to the added spacecraft potential energy.

As described in section 5.1.2, the energy can be converted to mass:

$$m_{amu} = cE_{eV}$$

Equation 32

where c is a conversion factor that depends on the spacecraft velocity (see Equation 26). The total uncertainty on the negative ion mass is therefore

$$\sigma_m = c\sigma_E = c(\sigma_o^2 + \sigma_{pot}^2)^{1/2}$$

Equation 33

If we insert the values discussed above, $\sigma_E = 0.16E_o$ and $\sigma_{pot} = 0.6$ in eV, we get:

$$\sigma_m = c(0.028\ E_o^2 + 0.36)^{1/2}$$

Equation 34

As an example, the uncertainty for a negative ion with a mass of 15.0 amu is 4.0 amu.

For measurements above approximately 25 eV (~134 amu), the energy resolution becomes the dominant uncertainty, and the mass uncertainty is 16.7 %.

5.8.2.2. Uncertainty on negative ion densities

We will now discuss some uncertainties on the negative ion densities. We first discuss two uncertainties that affect the normalised counts, and then the dominant uncertainty that appears when converting the normalised counts into densities.

The uncertainty on the raw counts (see section 5.2) assumes Poisson counting statistics and is therefore sqrt(counts). The negative ion density is given by Equation 29 as described in section 5.6.1. In order to show the effect that this uncertainty

has on the densities, we assume for a moment that the counting statistics is the only source of uncertainty. In this case the uncertainty on the densities is

$$\sigma_n = \frac{\sqrt{C}}{A_{eff}\varepsilon v}$$

Equation 35

where n is the negative ion density, C is the count rate, A_{eff} is the effective area of the instrument, ε is the estimated MCP efficiency for ions at this bias voltage and v is the spacecraft velocity. Depending on mass group, typical values of this uncertainty are between 0.02 cm^{-3} and 0.07 cm^{-3}, or between 0.13% and 1.3%.

Some other sources of uncertainty were considered in the calculation of the reference density in section 5.6.2. The reference density for a mass group can be regarded as the uncertainty on the negative ion densities due to anode scaling and electron background subtraction, assuming that no other uncertainties are present. This is of course not the case but it gives an indication of the effect on the densities due to these uncertainties.

The reference density is highest for the low mass groups (see Table 6). This is because the electron background subtraction is less accurate due to the dense, cold electron population at these energies. If we compare the reference density values with the uncertainties due to the counting statistics above, the reference density is consistently higher, generally by approximately one order of magnitude or more.

In section 5.2.5 we described the actuator walk effect. This phenomenon is not fully understood yet, however we do take the consequences into account when calculating the normalised counts that are used for the density determination by selecting the maximum count rate in each energy bin from the centre of the ion signature +/- 8 seconds (see section 5.2). By doing this we avoid missing part of the

ion beam. However, the low masses are affected strongly and it is possible that the main part (i.e. highest count rate) of groups 1 and 2 does not enter the instrument. We therefore consider the density data of mass groups 1 and 2 as a lower limit only.

The two central anodes, 4 and 5, are usually closest to the ram direction. However, quite often the angle to the ram direction of both anodes is the same, because the nominal ram direction is often at the boundary between anodes 4 and 5. Therefore neither of them point exactly in the ram direction. This may also result in missing a small part of the ion beam. As a consequence, strictly speaking the calculated densities should be regarded as a lower limit. Considering the difference in negative ion counts between anodes that have small but slightly different angles to the ram direction, the resulting uncertainty is probably of the same order of magnitude or smaller than the uncertainties considered above, and certainly smaller than the dominant uncertainty considered below. However, the effect should be investigated further in future studies.

We now consider the uncertainty on the MCP efficiency, which is the dominant uncertainty in calculating the negative ion density. As described in section 5.6.1, the MCP efficiency is difficult to estimate because negative ions were not expected to be detected by CAPS-ELS which is an instrument designed and calibrated to measure electrons. Using the work of Fraser (2001) (Figure 68), we estimate that the MCP efficiency could be in the range between 0.005 and 0.095. We therefore assign an uncertainty of 0.05 ±0.045. Using uncertainty propagation and assuming that no other uncertainties are present, the resulting uncertainty on the negative ion densities is also ±90% of the calculated values. This is clearly the dominant uncertainty.

Due to the large value of this uncertainty we suggest that the calculated negative ion densities are mainly useful in relative terms within the mass groups. The

uncertainty is mostly systematic in nature, hence comparing density ranges within the group should be acceptable. Figure 68 suggests that there is also an energy dependence on the MCP efficiency. We therefore suggest that the absolute values of the densities should not be compared directly, especially between mass groups with high mass differences. This should be avoided in any case though, because the mass ranges of the mass groups vary to a large extent. Due to the energy dependence we also advise caution in using total density values shown in this work.

5.8.3. Future work

More work can be done with the density and maximum mass data sets available from this study. The effects of the different controlling parameters need to be studied in more detail. In order to do this, certain controlling parameters need to be kept approximately constant to see the other effects more clearly. This is becoming less challenging as more flyby data become available. For example, to investigate latitudinal effects, we need to find a set of data with signatures during one year (to keep seasonal effects constant) at a small enough altitude range (e.g. 950 – 1050 km) and in a small SZA angle range, e.g. 0° - 50°.

Clearer trends may also be revealed by displaying the data in more convolved ways. For example, now that we have identified three different SZA regions (dayside, near terminator, and night side), we can include these parameters in other plots by using e.g. colour. As the T16 considerations show, seasonal effects should also be included in SZA, latitude and altitude plots by using different colours for different seasons or time periods. Furthermore, mercator style plots similar to the ones presented by Coates et al. (2009) will be useful and also make it easier to identify well sampled regions.

As discussed in section 5.5.6, it would be of great interest for this study to see a south polar flyby in or near the southern winter solstice in 2017. This would be to see if similarly high masses are observed as the unusually high masses observed during T16 which was at the north pole near the northern winter solstice. The T116 flyby in 2016 is planned to take place at a latitude of -84°N, however the currently planned CA altitude is too high to detect negative ions (1400 km).

The NTD region could be investigated in more detail by studying the extinction of solar flux as a function of different wavelengths and loci through the atmosphere determined by occultation experiments.

A trend dependence on other possible controlling parameters such as Saturn Local Time, winds on Titan, day/night transport (e.g. Cui et al., 2010) and the moon's rotation also needs to be investigated. In addition, instead of using SZA as a controlling parameter, it will also be interesting to investigate the dependence on optical depth directly.

In order to find out more about which negative ion species might be at work here, and also to possibly show some more or clearer trends, the mass groups could be narrowed down further to a larger number with smaller mass ranges. This way the number of different species included in one mass group would probably be smaller. Different species might be affected by the controlling parameters in different ways. This would be reflected more clearly in the density trends of these new mass groups. If a number of 'neighbouring' mass groups show the same trends, they can be put back together into larger groups. The limiting factor here is however the ranges of the energy bins. Some mass groups already contain only three energy bins. The mass ranges are also much larger at the higher masses because of the logarithmic scale of the energy bins.

An important next step is also to compare the negative ion densities with electron densities. While investigating negative ion density trends helps to determine what factors control and drive them, comparing the ion densities to electron densities is necessary in order to study the details of how the chemistry works and how the different negative ions form. It is, however, also important to carry out more modelling and also laboratory work to more fully understand the detailed chemistry.

An as yet unexplained phenomenon is the vertical striation structures found in some of the actuator fixed flyby observations (see section 5.7.2). In addition, more density profiles can be used to further study the altitude trends. We have yet to understand why during some flybys the densities reach a peak at a certain altitude, whereas during other flybys some mass group densities stay almost constant at different altitudes. T59 and T61 are two actuator fixed flybys that have not yet been analysed in detail. Other flybys can be used to produced altitude profiles too, as discussed in section 5.7.2.

Some of the causes of the actuator walk are still not fully understood. As described in section 5.2.5, possible ion winds need to be investigated, in addition to testing the actuator walk effects as a function of actuator angle and a more detailed analysis of the spacecraft potential effects. Furthermore, the effect of the instrument not pointing directly into the ram direction needs to be investigated in more detail, as discussed in the previous section.

In future studies it may be possible to use modified RPWS data with the offset added or combined with the Crary et al. (2009) results. This may require coverage of more flybys such that we can check that this offset is consistent.

As discussed in section 5.8.2.1, the spacecraft potential values used may be improved by implementing results from the Crary et al. (2009) study. This would slightly improve the accuracy of the calculated negative ion masses.

It is important to reduce, where possible, the density uncertainties. As discussed in the previous section, the instrument was not calibrated to measure negative ions, and it is therefore especially difficult to estimate the MCP efficiency and its dependence on energy. Although a thorough review of relevant literature was conducted, further insights may be obtained from future collaborations with workers in related fields.

It may be possible to further research the literature and communicate with specialists to improve the current understanding of how MCPs react to negative ions. However, ideally the instrument needs to be tested. The CAPS-ELS engineering model is located at SwRI (Southwest Research Institute) in San Antonio, Texas. Testing this instrument would give great insight into what MCP efficiency should be used, even if it is not the exact same instrument as that now at Saturn which also has a different MCP history.

5.9. Summary

We used data from 34 Cassini Titan flybys from the first, TA on 26 October 2004, to T71 on 7 July 2010. Negative ions are detected when the flyby altitude is low enough (<1400 km) and CAPS points in the ram direction. Seven groups of masses have been identified because recurrent peaks are observed in the mass-per-charge spectra of different encounters (section 5.3).

The main science results of the negative ion work presented in this chapter are:

- There is a preference for higher masses and densities at lower altitudes (sections 5.5.3, 5.6.3, 5.7.3, 5.7.4.2 and 5.8.1.1)
- The maximum altitude at which different mass groups are observed decreases with increasing mass (Table 7) (sections 5.6.3 and 5.8.1.1)
- Unusually high masses and high densities observed during T16 may be a result of polar winter conditions (sections 5.5.6 and 5.8.1.2)
- The highest densities of negative ions with mass < 130 amu/q (groups 1 – 4) are observed on Titan's sunlit dayside (section 5.6.4 and 5.8.1.2)
- Predominantly low densities are present at SZAs between the surface terminator (90° SZA) and the terminator at 1000 km altitude (135° SZA); this near terminator depression (NTD) effect is especially prominent at higher masses (sections 5.6.4, 5.7.4, 5.8.1.2 and 5.8.1.4)

We have identified three different regions defined by the solar zenith angle which show different mass and density behaviour: The dayside, the near terminator depression (NTD) region and the nightside. The boundaries between these regions vary slightly for different mass groups but are near the surface terminator (90° SZA) and the 1000 km altitude terminator (135° SZA). Mass groups also show individual trends. Each region is exposed to different conditions which in turn are governed by a combination of different reactions. As a result, the range of negative ion densities and masses vary depending on which region they are in.

6. Conclusions

Titan is a particularly complex solar system body to study. Its interaction with the surrounding plasma is similar to that of the solar wind with Venus or Mars, and comets. However, Titan can be exposed to Saturn's magnetospheric plasma or the solar wind. The plasma and magnetic configuration inside the magnetosphere are highly variable. This constantly changes the magnetic structure of the interaction, allowing different ionisation processes and reactions to take place and change location. In addition, Titan hosts one of the most complex chemical systems known.

In the first two science chapters (3 and 4) we used CAPS-ELS electron data to study Titan's magnetic environment and upper ionospheric structure. We learnt that photoelectrons produced in the dayside ionosphere can travel to larger distances from Titan in the exosphere and ionospheric tail via magnetic field lines. This was the first step in establishing a more structured view of Titan's magnetic environment. Knowing that we can use photoelectrons as tracers of magnetic field lines, the next step will be to conduct a statistical survey of locally produced photoelectrons, and photoelectrons in the exosphere and tail.

The discovery of the electron acceleration regions, described in chapter 4, and their relation to the corotation electric field and possible pick up ions is a key factor in understanding the structure of the topside ionosphere. Further analysis is necessary to fully understand the process causing these events. This should include the study of the actual electric field direction rather than the nominal direction which can vary considerably due to the changing environment, and a closer analysis of the pick up ions. A more complete understanding of these regions will also

contribute to the magnetic environment study; if the observed changes in electron energy in these regions are due to an acceleration of ionospheric electrons then ionospheric photoelectrons would also be affected.

The second science part of the thesis (chapter 5) is concerned with CAPS-ELS measurements of negative ions in Titan's ionosphere. The Cassini-Huygens mission has revealed the presence of complex organic chemistry even at altitudes as high as 1100 km in Titan's atmosphere. The discovery of heavy negative (Coates et al., 2007b) and positive ions (e.g. Waite et al., 2005, 2007) in the upper ionosphere have necessitated the rethinking of Titan's chemical system as a whole. For example, the particles making up Titan's haze layers below 500 km were believed to originate in similar atmospheric regions in the pre-Cassini era but may actually be a direct product of the negative ion chemistry in the upper ionosphere studied here, which fall to the lower atmosphere. Painting this new, detailed picture of Titan's chemical system is an ongoing process consisting of spacecraft data analysis, modelling and laboratory experiments and simulations. CAPS-ELS only provides very limited compositional negative ion information through the identification of mass peaks in the spectra and was designed to measure electrons. Our contribution with the work presented in this thesis is therefore aimed at constraining the different negative ion formation and destruction processes by demonstrating what conditions result in higher and lower densities and masses and how different groups of masses react to changing external factors. The information will hopefully prove valuable to use in models and laboratory experiments.

Clear trends found include an altitude dependence and three different regions consisting of the dayside, nightside and near terminator region. A possible seasonal effect may also have been discovered which explains that the very high masses observed during the T16 encounter could be due to polar winter conditions. This theory will hopefully be put to the test during the winter solstice in the southern hemisphere in 2017. In addition, now that some controlling factors have been

identified, the data can be analysed in different ways by keeping known controlling factors constant to avoid certain biases. This will become more achievable with the ever-increasing number of flybys. Other important future studies include a direct comparison of electron and negative ion densities, and reducing the uncertainties related to MCP efficiencies.

Acronyms

ASI: Italian Space Agency

CA: Closest Approach

CAPS: Cassini Plasma Spectrometer

ELS: Electron Spectrometer

ENA: Energetic neutral atom

ESA: Electrostatic analyser

FGM: Fluxgate Magnetometer

FOV: Field of view

FPP: Fields and particles palette

GCR: Galactic cosmic rays

HASI: Huygens Atmospheric Structure Instrument

HGA: High gain antenna

ESA: Electrostatic analyser

IBS: Ion Beam Spectrometer

IMS: Ion Mass Spectrometer

INMS: Ion and Neutral Mass Spectrometer

IP: Interplanetary dust

LEF: Linear electric field

LEMMS: Low Energy Magnetospheric Measurement System

LP: Langmuir Probe

MAG: Magnetometer

MCP: Microchannel plate

MIMI: Magnetospheric Imaging Instrument

NTD: Near terminator depression

RPWS: Radio and Plasma Wave Science

RSS: Radio Science Subsystem

RTG: Radio Thermo Isotope Generator

SOI: Saturn orbit insertion

SRA: Solar incidence-ram-angle

S/VHM: Scalar/Vector Helium Magnetometer

SwRI: Southwest Research Institute

SZA: Solar zenith angle

TOF: Time of flight

UTC: Coordinated Universal Time

7. References

Ågren, K., Wahlund, J.-E., Garnier, P., Modolo, R., Cui, J., Galand, M. and Muller-Wodarg, I. (2009), On the ionospheric structure of Titan, Planet. Space Sci., 57, 1821–1827.

Ågren, K., et al. (2011), Detection of currents and associated electric fields in Titan's ionosphere from Cassini data, J. Geophys. Res., 116, A04313, doi:10.1029/2010JA016100.

Ågren, K., N. J. T. Edberg, and J.-E. Wahlund (2012), Detection of negative ions in the deep ionosphere of Titan during the Cassini T70 flyby, Geophys. Res. Lett., 39, L10201, doi:10.1029/2012GL051714.

Andersson, P. (2009), Laser Photodetachment of Negative Ions, Ph.D. dissertation, Department of Physics, University of Gothenburg, Gothenburg, Sweden.

Arridge, C. S., N. Achilleos and P. Guio (2011), Electric field variability and classifications of Titan's magnetoplasma environment, Ann. Geophys., 29, 1253-1258, doi:10.5194/angeo-29-1253-2011.

Arridge, C. S. et al. (2011), Upstream of Saturn and Titan, Space Sci. Rev., vol. 162, pages:25-83, 10.1007/s11214-011-9849-x.

Arridge, C.S., et al. (2012), Mapping Magnetospheric Equatorial Regions at Saturn from Cassini Prime Mission Observations, Space Sci. Rev., 164(1-4), pp. 1-83, doi:10.1007/s11214-011-9850-4.

Bagenal, F. (2001), Planetary Magnetospheres, Encyclopedia of Astronomy and Astrophysics, ed. Murdin, P., IOP Publishing.

Bame, S.J., J.R. Asbridge, H.E. Felthauser, J.P. Glore, H.L. Hawk, and J. Chavez, ISEE-C solar wind plasma experiment, IEEE Trans. Geosci. Electron., GE-16, 160-162, 1978.

Baumjohann, W. and R. A. Treumann (1997), Basic Space Plasma Physics, Imperial College Press, London.

Bertucci, C., N. Achilleos, M. K. Dougherty, R. Modolo, A. J. Coates, K. Szego, A. Masters, Y. Ma, F. M. Neubauer, P. Garnier, J.-E. Wahlund, D. T. Young (2008), The Magnetic Memory of Titan's Ionized Atmosphere, Science, Vol. 321, doi: 10.1126/science.1159780.

Blanc, M. et al. (2001), Magnetospheric and Plasma Science with Cassini-Huygens, Space Science Reviews 104: 253–346, Kluwer Academic Publishers.

Bohme, D.K. (1992), PAH and Fullerene ions and ion/molecule reactions in interstellar and circumstellar chemistry. Chem. Rev. 92, 1487–1508.

Borucki, W. J., et al. (2006), Predictions of the electrical conductivity and charging of the aerosols in Titan's atmosphere, Icarus, 181, 527–544.

Borucki, W. J. and R. C. Whitten (2008), Influence of high abundances of aerosols on the electrical conductivity of the titan atmosphere, Planet. Space Sci, 56(1), pp. 19-26.

Broadfoot, A. L., et al. (1981), Extreme ultraviolet observations from Voyager 1 encounter with Saturn, Science, 212, 206.

Brown, R. H., J.-P. Lebreton, and J. H. Waite (2009), Overview, in Titan from Cassini-Huygens, Springer, edited by R. H. Brown, J.-P. Lebreton and J. H. Waite, p. 1-7.

Burton, M. E., Buratti, B., Matson, D. L., and Lebreton, J. P. (2001). The Cassini/Huygens Venus and Earth flybys: An overview of operations and results. J. Geophys. Res., 106(A12):30099–30107.

Chaizy, P., H. Reme, J. A. Sauvaud, C. d'Uston, R. P. Lin, D. E. Larson, D. L. Mitchell, K. A. Anderson, C. W. Carlson, A. Korth & D. A. Mendis (1991), Negative ions in the coma of comet Halley, Nature, 349, 393– 396.

Coates, A.J., A.D. Johnstone, J.J. Sojka,G.L. Wrenn (1985), Ionospheric photoelectrons observed in the magnetosphere at distances up to 7 Earth radii, Planet. and Space Science, vol. 33, p. 1267-1275, doi: 10.1016/0032-0633(85)90005-4.

Coates, A. J. (2001), Our solar system and beyond in the new millennium, in Visions of the Future: Astronomy and Earth Science, ed. J.M.T. Thompson, p. 85-113, Cambridge University Press.

Coates, A. J., F. J. Crary, D. T. Young, K. Szego, C. S. Arridge, Z. Bebesi, E. C. Sittler Jr., R. E. Hartle, and T. W. Hill (2007a), Ionospheric electrons in Titan's tail: Plasma structure during the Cassini T9 encounter, Geophys. Res. Lett., 34, L24S05, doi:10.1029/2007GL030919.

Coates, A. J., F. J. Crary, G. R. Lewis, D. T. Young, J. H. Waite Jr., and E. C. Sittler Jr. (2007b), Discovery of heavy negative ions in Titan's ionosphere, Geophys. Res. Lett., 34, L22103, doi:10.1029/2007GL030978.

Coates, A. J., et al. (2008), Ionospheric photoelectrons at Venus: Initial observations by ASPERA-4 ELS, Planet. Space Sci., 56, 802–806, doi:10.1016/j.pss.2007.12.008.

Coates, A. J., A. Wellbrock, G. R. Lewis, G. H. Jones, D. T. Young, F. J. Crary and J. H. Waite (2009), Heavy negative ions in Titan's atmosphere: Altitude and latitude dependence, Planet. Space Sci., 57, issues 14-15, 1899-1871, doi: 10.1016/j.pss.2009.05.00.

Coates, A. J. (1991), Observations of the velocity distribution of pickup ions, in 'Cometary Plasma Processes', Geophysical Monograph 61, pp. 301 – 310, AGU.

Coates, A.J. (2009), Interaction of Titan's ionosphere with Saturn's magnetosphere, Phil. Trans. R. Soc. A, 367, 773–788, doi:10.1098/rsta.2008.0248.

Coates, A.J., and G. H. Jones (2009), Plasma environment of Jupiter family comets, Planetary and Space Science, 57, 1175–1191, doi:10.1016/j.pss.2009.04.009.

Coates, A. J., G. H. Jones, G. R. Lewis, A. Wellbrock, D. T. Young, F. J. Crary, R. E. Johnson, T. A. Cassidy, T. W. Hill (2010), Negative ions in the Enceladus plume, Icarus, 206, 618-622, doi: 10.1016/j.icarus.2009.07.013.

Coates, A. J., S. M. E. Tsang, A. Wellbrock, R. A. Frahm, J. D. Winningham, S. Barabash, R. Lundin, D. T. Young, F. J. Crary (2011), Ionospheric photoelectrons: Comparing Venus, Earth, Mars and Titan, Planet. Space Sci., 59, 1019-1027, doi: 10.1016/j.pss.2010.07.016.

Coustenis, A. & F. W. Taylor (2008), Titan: Exploring an Earthlike World, World Scientific.

Cowley, S., E. Bunce and J. O'Rourke (2004). A simple quantitative model of plasma flows and currents in Saturn's polar ionosphere. J. Geophys. Res, 109(10.1029).

Crary, F. J., B. A. Magee, K. Mandt, J. H. Waite Jr., J. Westlake, D. T. Young (2009), Heavy ions, temperatures and winds in Titan's ionosphere: Combined Cassini CAPS and INMS observations, Planet. Space Sci., 57, 1847-1856, doi:10.1016/j.pss.2009.09.006.

Cravens, T.E. (2001), Saturn: Magnetosphere Interaction with Titan. Encyclopedia of Astronomy and Astrophysics, Nature Publishing Group 2001, Institute of Physics Publishing 2006.

Cravens, T. E. (2004), Physics of Solar System Plasmas, ISBN 0521611946, Cambridge, UK, Cambridge University Press.

Cravens, T. E., I. P. Robertson, J. H. Waite, R. V. Yelle, W. T. Kasprzak, C. N. Keller, S. A. Ledvina, H. B. Niemann, J. G. Luhmann, R. L. McNutt, W.-H. Ip, V. De La Haye, I.Mueller-Wodarg, J.-E.Wahlund,V. G. Anicich, and V. Vuitton (2006), Composition of Titan's ionosphere, Geophys. Res. Lett., 33:7105.

Cravens, T. E., I.P. Robertson, J.H. Waite Jr., R.V. Yelle, V. Vuitton, A.J. Coates, J.-E. Wahlund, K. Ågren, M.S. Richard, V. De La Haye, A. Wellbrock, F.M. Neubauer (2009), Model-data comparisons for Titan's nightside ionosphere, Icarus, 199, p. 174-188, doi:10.1016/j.icarus.2008.09.005.

Cravens, T. E., R. V. Yelle, J.-E. Wahlund , D. E. Shemansky, and A. F. Nagy (2009), Composition and Structure of the Ionosphere and Thermosphere, in Titan from

Cassini-Huygens, Springer, edited by R. H. Brown, J.-P. Lebreton and J. H. Waite, p. 259-295.

Cui, J., M. Galand, R. V. Yelle, J.-E. Wahlund, K. Ågren, J. H. Waite Jr., and M. K. Dougherty (2010), Ion transport in Titan's upper atmosphere, J. Geophys. Res., 115, A06314, doi:10.1029/2009JA014563.

De Pater, I. and J. J. Lissauer (2001), Planetary Sciences, Cambridge University Press.

Desch, S. J., et al. (2002), Progress in planetary lightning, Rep. Prog. Phys., 65, 955–997.

Dougherty M. K. et al. (2004), The Cassini magnetic field investigation, Space Science Reviews, 114, 331-383.

Dungey J. W. (1961). Interplanetary magnetic field and the auroral zones. Physical Review Letters, 6(2), 47-48.

Edberg, N. J. T., J.-E. Wahlund, K. Ågren, M. W. Morooka, R. Modolo, C. Bertucci, and M. K. Dougherty (2010), Electron density and temperature measurements in the cold plasma environment of Titan: Implications for atmospheric escape, Geophys. Res. Lett., 37:L20105.

English, M. A., L. M. Lara, R. D. Lorenz, P. R. Ratcliff, R. Rodrigo (1996), Ablation and chemistry of meteoric materials in the atmosphere of Titan, Advances in Space Research, Volume 17, Issue 12, pages 157 – 160, http://dx.doi.org/10.1016/0273-1177(95)00774-9.

Frahm, R. A., et al. (2006), Carbon dioxide photoelectron peaks at Mars, Icarus, 182(2), p. 371– 382, doi:10.1016/j.icarus.2006.01.014.

Frahm, R. A., et al. (2006b), Locations of atmospheric photoelectron energy peaks within the mars environment, Space Sci. Reviews (2006), 126: 389–402, doi: 10.1007/s11214-006-9119-5.

Frahm, R. A., et al. (2007), Locations of atmospheric photoelectron energy peaks within the Mars environment, Space Sci. Rev., 126, 389– 402, doi:10.1007/s11214-006-9119-5.

Fraser, G. W. (2002), The ion detection efficiency of microchannel plates (MCPs), International Journal of Mass Spectrometry, 215, 13-30.

Fulchignoni et al. (2005), In Situ measurements of the physical characteristics of Titan's environment, Nature 438, 785-791, doi:10.1038/nature04314.

Galand, M., R. V. Yelle, A. J. Coates, H. Backes, and J.-E. Wahlund (2006), Electron temperature of Titan's sunlit ionosphere, Geophys. Res. Lett., 33, L21101, doi:10.1029/2006GL027488.

Galand, M., R. V. Yelle, J. Cui, J.-E. Wahlund, V. Vuitton, A. Wellbrock, and A. Coates (2010), Ionization sources in Titan's deep ionosphere, J. Geophys. Res., 115, A07312, doi:10.1029/2009JA015100.

Gan, L., C. N. Keller, and T. E. Cravens (1992), Electrons in the Ionosphere of Titan, J. Geophys. Res., 97(A8), 12,137–12,151.

Ganguli, S. B. (1996), The polar wind, Rev. Geophys., 34, 311-348, 1996.

Garnier, P., I. Dandouras, D. Toublanc, P. C. Brandt, E. C. Roelof, D. G. Mitchell, S. M. Krimigis, N. Krupp, D. C. Hamilton, H. Waite (2007), The exosphere of Titan and its

interaction with the kronian magnetosphere: MIMI observations and modeling, Planet. Space Sci., 55, 165-173, doi:10.1016/j.pss.2006.07.006.

Gombosi, T. I. et al (2009), Saturn's Magnetospheric Configuration, in Saturn from Cassini-Huygens, Springer, edited by M. K. Dougherty, L. W. Esposito and S. M. Krimigis, p. 203-256, doi: 10.1007/978-1-4020-9217-6_9.

Gurnett D. A., et al. (2004), The Cassini Radio and Plasma Wave Investigation, Space Science Reviews, 114, 1, 395 . 463.

Hanel, R.A., B.J. Conrath, F.M. Flasar, V. Kunde, W. Maguire, J. Pearl, J. Pirraglia, R. Samuelson, L. Herath, M. Allison, D. Cruikshank, D. Gautier, P. Gierasch, L. Horn, R. Koppany, and C. Ponnamperuma (1981), Infrared Observations of the Saturnian System from Voyager 1, Science, Vol. 212, p. 192.

Hargreaves, J. K. (1992), The Solar-Terrestrial Environment, Cambridge Atmos. Space Sci. Ser., vol. 5, Cambridge Univ. Press, Cambridge, UK.

Hartle, R. E., et al. (1982), Titan's exosphere observed from Voyager 1, J. Geophys. Res., 87, 1383-1394.

Hartle, R. E. and J. M. Grebowsky (1995), Planetary loss from light ion escape on Venus, Advances in Space Research, Vol. 15, issue 4, 117-122, doi: 10.1016/0273-1177(94)00073-A.

Hartle, R. E., et al. (2006), Initial interpretation of Titan plasma interaction as observed by the Cassini Plasma Spectrometer: Comparisons with Voyager 1, Planet. Space Sci., 54, 1211 –1224.

Horanyi, M., T. W. Hartquist, O. Havnes, D. A. Mendis, and G. E. Morfill (2004), Dusty plasma effects in Saturn's magnetosphere, Rev. Geophys., 42, RG4002, doi:10.1029/2004RG000151.

Hunten, D. M., et al. (1984), Titan, in Saturn, edited by T. Gehrels and M. S. Matthews, Univ. of Arizona Press, Tucson.

Jackman, C. M., N. Achilleos, E. J. Bunce, B. Cecconi, J. T. Clarke, S. W. H. Cowley, W. S. Kurth, andP. Zarka (2005), Interplanetary conditions and magnetospheric dynamics during the Cassini orbit insertion fly-through of Saturn's magnetosphere, J. Geophys. Res., 110, A10212, doi:10.1029/2005JA011054.

Johnstone A.D., et al. (1997), PEACE: A plasma electron and current experiment, Space Science Reviews, 79, 1 - 2, 351 . 398.

Jones, G. H., A. J. Coates, A. Wellbrock and the CAPS team (2011), Negative Ion Flow at Titan, presented at the American Geophysical Union fall meeting 2011.

Kallio, E., J.-Y. Chaufray, R. Modolo, D. Snowden, R. Winglee (2011), Modeling of Venus, Mars and Titan, Space Sci Rev (2011) 162:267–307, DOI 10.1007/s11214-011-9814-8.

Kanani, S. J., et al. (2010), A new form of Saturn's magnetopause using a dynamic pressure balance model, based on in situ, multi-instrument Cassini measurements, J. Geophys. Res., 115, A06207, doi:10.1029/2009JA014262.

Keller, C.N. and T. E. Cravens (1994), One-dimensional multispecies hydrodynamic 335 models of the wakeside ionosphere of Titan, J. Geophys. Res., 99, 6527-6536.

Kivelson, M. G., & Russell, C. T. (1995). Introduction to space physics: Cambridge Univ Pr.

Kivelson, M. G., K. K. Khurana, C. T. Russel, R. J. Walker, J. Warnecke, F. V. Coroniti, C. Polanskey, D. J. Southwood & G. Schubert (1996), Discovery of Ganymede's magnetic field by the Galileo spacecraft, Nature 384, 537 – 541, doi:10.1038/384537a0.

Kivelson, M. G. (2006), Does Enceladus Govern Gagnetospheric Dynamics at Saturn? Science 311, 1391-1392, 10.1126/science.1124494.

Kliore, A. J., et al. (2008), First results from the Cassini radio occultations of the Titan ionosphere, J. Geophys. Res., 113, A09317, doi:10.1029/2007JA012965.

Lewis, G. R. et al. (2010), The calibration of the Cassini-Huygens CAPS Electron Spectrometer, Planet. Space Sci., 58, 427-436, doi:10.1016/j.pss.2009.11.008.

Lewis, G., André, N., Arridge, C., Coates, A., Gilbert, L., Linder, D., & Rymer, A. (2008). Derivation of density and temperature from the Cassini-Huygens CAPS electron spectrometer. Planetary and space science, 56(7), 901-912.

Liang, M.-C., Y. L. Yung, D. E. Shemansky (2007), Photolytically generated aerosols in the mesosphere and thermosphere of Titan, The Astrophysical Journal, 661, L199-L202, doi: 10.1086/518785.

Linder, D. R., et al. (1998), The Cassini CAPS electron spectrometer, in Measurement Techniques in Space Plasmas: Particles, Geophys. Monogr. Ser., Vol. 102, edited by R. E. Pfaff, J. E. Borovsky, and D. T. Young, pp. 257– 262, AGU, Washington, D. C.

Ma, Y. J., et al. (2009), Time-dependent global MHD simulations of Cassini T32 flyby: From magnetosphere to magnetosheath, J. Geophys. Res., 114, A03204, doi:10.1029/2008JA013676.

Mantas and Hanson (1979), Photoelectron Fluxes in the Martian Ionosphere, J. Geophys. Res., Vol. 84, No. A2, pp. 369-385, doi:10.1029/JA084iA02p00369.

McAndrews, H. J., C. J. Owen, M. Thomsen, B. Lavraud, A. Coates, M. Dougherty, and D. T. Young (2008), Evidence for reconnection at Saturn's magnetopause, J. Geophys. Res., 113, A04210, doi:10.1029/2007JA012581.

Michael, M., S. N. Tripathi, P. Arya, A. J. Coates, A. Wellbrock, D. T. Young (2011), High-altitude charged aerosols in the atmosphere of Titan, Planet. Space Sci., 59, 880-885, doi: 10.1016/j.pss.2011.03.010

G.J. Molina-Cuberos et al. (1999), Ionization by cosmic rays of the atmosphere of Titan Planetary and Space Sci., 47, 1347-1354.

Mueller-Wodarg, I.C.F., Yelle, R.V., Mendillo, M., Young, L.A. and Aylward, A.D. (2000), The thermosphere of Titan simulated by a global three-dimensional time-dependent model, Journal of Geophysical Research, Vol. 105, No. A9, pp. 20,833-20.

Neubauer, F. M., D. A. Gurnett, J. D. Scudder, and R. E. Hartle (1984), Titan’s magnetospheric interaction, in Saturn, Univ. of Ariz. Press, Tucson, edited by T. Gehrels and M. S. Matthews, pp. 760–787.

Owen, T. (2005), Planetary science: Huygens rediscovers Titan, Nature 438, 756-757, doi:10.1038/438756a.

Robertson, IP and Cravens, TE and Waite, JH and Yelle, RV and Vuitton, V and Coates, AJ and Wahlund, JE andAgren, K and Mandt, K and Magee, B and Richard, MS and Fattig, E (2009) Structure of Titan's ionosphere: Model comparisons with Cassini data. Plat. Space Sci , 57 (14-15) 1834 - 1846. 10.1016/j.pss.2009.07.011.

Roboz A., Nagy A. F. (1994), The energetics of Titan's ionosphere. J. Geophys. Res. 99(A2):2087.

Russell, C. T. (1991), Planetary Magnetospheres, Science Progress, 75, 93-105.

Rymer, A.M., A. J. Coates, K. Svenes, G. A. Abel, D. R. Linder, B. Narheim, M. Thomsen, and D. T. Young (2001), Cassini Plasma Spectrometer Electron Spectrometer measurements during the Earth swing-by on August 18, 1999, Journal of Geophysical Research, Vol. 106, No. A12, pages 30,177 – 30,198.

Rymer, A. M., H. T. Smith, A. Wellbrock, A. J. Coates, and D. T. Young (2009), Discrete classification and electron energy spectra of Titan's varied magnetospheric environment, Geophys. Res. Lett., 36, L15109, doi:10.1029/2009GL039427.

Schunk, R. W. & A. F. Nagy (2009), Ionospheres: Physics, Plasma Physics, and Chemistry, second edition, Cambridge University Press.

Sillanpää, I. (2008), Hybrid Modeling of Titan's Interaction with the Magnetosphere of Saturn, Ph.D. dissertation, Department of Physical Sciences, Faculty of Science, University of Helsinki, Yliopistopaino, Helsinki, Finland.

Sillanpää, I., D. T. Young, F. Crary, M. Thomsen, D. Reisenfeld, J.-E. Wahlund, C. Bertucci, E. Kallio, R. Jarvinen, and P. Janhunen (2011), Cassini Plasma Spectrometer and hybrid model study on Titan's interaction: Effect of oxygen ions, J. Geophys.

Res., 116, A07223, doi:10.1029/2011JA016443.

Sittler, E. C. Jr., R. E. Hartle, A. F. Viñas, R. E. Johnson, H. T. Smith and I. Mueller-Wodarg (2004), Titan Interaction with Saturn's Magnetosphere: Mass Loading and Ionopause Location, in “Proceedings of the International Conference ‘Titan – from discovery to encounter’, 13-17 April 2004, ESTECT, Noordwijk, Netherlands. Ed.: Karen Fletcher. ESA SP-1278, Noordwijk, Netherlands: ESA Publications Division, ISBN 92-9092-997-9, 2004, p. 377 - 394".

Sittler, E. C. Jr., A.Ali, J.F.Cooper, R.E.Hartle, R. E.Johnson, A. J. Coates, D. T. Young (2009a), Heavy ion formation in Titan’s ionosphere: Magnetospheric introduction of free oxygen and a source of Titan’s aerosols?, Planet. Space Sci., 57, 1547-1557, doi:10.1016/j.pss.2009.07.017.

Sittler E. C., R. E. Hartle, C. Bertucci, A. J. Coates, T. E. Cravens, I. Dandouras and D. Shemansky (2010), Energy Deposition Processes in Titan's Upper Atmosphere and Its Induced Magnetosphere, in Titan from Cassini-Huygens, Springer, edited by R. H. Brown, J.-P. Lebreton and J. H. Waite, p. 393-453, doi: 10.1007/978-1-4020-9215-2_16.

Strobel, D. F., M. E. Summers, and X. Zhu (1992), Titan's upper atmosphere: Structure and ultraviolet emissions, Icarus, 100, 512-526.

Strobel, D. F. S. K. Atreya , B. Bézard, F. Ferri, F. M. Flasar, M. Fulchignoni, E. Lellouch, and I. C. F. Müller-Wodarg (2009), Atmospheric Structure and Composition, in Titan from Cassini-Huygens, Springer, edited by R. H. Brown, J.-P. Lebreton and J. H. Waite, p. 235-257, doi: doi10.1007/978-1-4020-9215-2.

Szego, K., Z. Bebesi, C. Bertucci, A. J. Coates, F. Crary, G. Erdos, R. Hartle, E. C. Sittler Jr., and D. T. Young (2007), Charged particle environment of Titan during the T9 flyby, Geophys. Res. Lett., 34, L24S03, doi:10.1029/2007GL030677.

Tokano, T., F. M. Neubauer, M. Laube, P. McKay (1999), Seasonal variation of Titan's atmospheric structure simulated by a general circulation model, Planetary and Space Science 47, 493-520.

Tomasko, M., et al., 2005. Rain, winds and haze during Huygens probe's descent to Titan's surface. Nature 438 (8), 765–778, doi:10.1038/nature04126.

Vasyliunas, V. (1983). Plasma distribution and flow. Physics of the Jovian magnetosphere, 1, 395-453.

Vuitton, V., R. V. Yelle, M. J McEwan (2007), Ion chemistry and N-containing molecules in Titan's upper atmosphere, Icarus, 191, 722-742, doi: 10.1016/j.icarus.2007.06.023.

Vuitton, V., R. V. Yelle, and J. Cui (2008), Formation and distribution of benzene on Titan, J. Geophys. Res., 113, E05007, doi:10.1029/2007JE002997.

Vuitton, V., Lavvas, P., Yelle, R.V., Galand, M., Wellbrock, A., Lewis, G.R., Coates, A.J., Wahlund, J.-E. (2009), Negative ion chemistry in Titan's upper atmosphere, Planet. Space Sci., 57, 1558–1572, doi:10.1016/j.pss.2009.04.004.

Wahlund, J.-E. et al. (2005), Cassini Measurements of Cold Plasma in the Ionosphere of Titan, Science, Vol. 308 no. 5724 pp. 986-989, DOI: 10.1126/science.1109807.

Wahlund, J.-E., M.Galand, I.Muller-Wodarg, J.Cui, R.V.Yelle, F.J.Crary, K.Mandt, B.Magee, J.H.Waite, D.T.Young, A.J.Coates, P.Garnier, K. Ågren, M.Andre, A. I.

Eriksson, T. E. Cravens, V. Vuitton, D.A.Gurnett, W.S.Kurth (2009), On the amount of heavy molecular ions in Titan's ionosphere, Planet. Space Sci., 57, 1857-1865, doi:10.1016/j.pss.2009.07.014.

Waite, J. H., Jr., et al. (2005), Ion neutral mass spectrometer results from the first flyby of Titan, Science, 308, 982 – 986, doi:10.1126/science.1110652.

Waite, J.H., D. T. Young, T. E. Cravens, A. J. Coates, F. J. Crary, B. Magee, and J. Westlake (2007), The Process of Tholin Formation in Titan's Upper Atmosphere, Science, Vol. 316 no. 5826 pp. 870-875, doi: 10.1126/science.1139727.

Waite, J. H., D. T. Young, J. H. Westlake, J. I. Lunine, C. P. McKay, and W. S. Lewis (2010), High-Altitude Production of Titan's Aerosols, in Titan from Cassini-Huygens, Springer, edited by R. H. Brown, J.-P. Lebreton and J. H. Waite, doi: 10.1007/978-1-4020-9215-2_8.

Wei, H. Y., C. T. Russell, J.-E. Wahlund, M. K. Dougherty, C. Bertucci, R. Modolo, Y. J. Ma, and F. M. Neubauer (2007), Cold ionospheric plasma in Titan's magnetotail, Geophys. Res. Lett., 34, L24S06, doi:10.1029/2007GL030701.

Wei, H. Y., C. T. Russell, M. K. Dougherty, F. M. Neubauer, and Y. J. Ma (2010), Upper limits on Titan's magnetic moment and implications for its interior, J. Geophys. Res., 115, E10007, doi:10.1029/2009JE003538.

Wellbrock, A., A. J. Coates, I. Sillanpää, G. H. Jones, C. S. Arridge, G. R. Lewis, D. T. Young, F. J. Crary, and A. D. Aylward (2012), Cassini observations of ionospheric photoelectrons at large distances from Titan: Implications for Titan's exospheric environment and magnetic tail, J. Geophys. Res., 117, A03216, doi:10.1029/2011JA017113.

Westlake, J. H., J. M. Bell, J. H. Waite Jr., R. E. Johnson, J. G. Luhmann, K. E. Mandt, B. A. Magee, and A. M. Rymer (2011), Titan's thermospheric response to various plasma environments, J. Geophys. Res., 116, A03318, doi:10.1029/2010JA016251.

Wurz, P., Balogh, A., Coffey, V., Dichter, B., Kasprzak, W., Lazarus, A., Lennartsson, W., McFadden, J. (2007), Calibration techniques, in: Wuest, M., Evans, D. S., von Steiger, R. (Eds.), Calibration of Particle Instruments in Space Physics. The International Space Science Institue, ESA Communications, pp. 117–276.

Yelle, R. V., N. Borggren, V. de la Haye, W.T. Kasprzak, H.B. Niemann, I. Muller-Wodarg, J.H. Waite Jr. (2006), The vertical structure of Titan’s upper atmosphere from Cassini Ion Neutral Mass Spectrometer measurements, Icarus, 182, 567-576, doi:10.1016/j.icarus.2005.10.029.

Young, D. T., et al. (2004), Cassini Plasma Spectrometer investigation, Space Sci. Rev., 114, 1–112, doi: 10.1007/s11214-004-1406-4.

Acknowledgements

I would like to thank my supervisor Andrew C. for his great support, guidance and understanding. Thank you for giving me the opportunity to work on unique and exciting topics such as negative ions at Titan. I am also very grateful to you for all the travel opportunities I have had during my time as a PhD student. Attending conferences, workshops and meetings around the world has been an invaluable experience both in terms of networking and improving my scientific knowledge.

A big thank you also goes to Geraint J. who has been an invaluable extra source of help and support. Thank you to Alan A., my secondary supervisor, for your guidance and teachings especially during the early part of my PhD, and to Nick A. for your help and guidance in choosing the right topics during the very early stages of the PhD.

Thank you to my thesis examiners Emma Bunce and Lidia van Driel-Gesztelyi for taking the time to read this work so carefully.

Thank you to Gethyn, Lin and Neville for IDL and operations support. Thank you to the MSSL planetary and plasma groups for providing guidance and feedback during group and practice talks. Thanks to Frank Crary, Dave Young and the CAPS team for their general advice.

Thank you to my collaborators for working with me and for your help: Chris Arridge, Ilkka Sillanpää, Karin Ågren, Niklas Edberg, Hanying Wei, Brian Magee, Abi Rymer, Todd Smith, Yasir Soobiah, Cesar Bertucci, Tom Cravens, Marina Galand, Zoltan Nemeth, Marykutty Michael, Yingjuan Ma, Veronique Vuitton, Panayotis Lavvas and Erik Vigren.

Thank you to everyone I shared office 108 with, you all made it a great office to work in. Thanks to my friends from the student flats, the lab in general and our lunch group. Thank you to my Australian ‘family’ and friends at home and around the world. Thank you Craig for your wonderful support. Vielen lieben Dank an meine Eltern und Grosseltern für die Möglichkeiten, dir ihr mir eröffnet habt.